Department of Precision and Microsystems Engineering

Design and Fabrication of a Soft Photonic Crystal Brain Implant

Damla Yengül

Report no   : MNE-2021.059
Coach   : Dr.D. Fan
Professor   : Prof. dr. U. Staufer
Specialisation   : Micro and Nano Engineering
Type of report   : Master Thesis
Date   : 17 September 2021

TU**Delft** Delft
University of
Technology

Design and Fabrication of a Soft Photonic Crystal Brain Implant

by

Damla Yengül

to obtain the degree of Master of Science

at the Delft University of Technology,

to be defended publicly on Tuesday September 17, 2021 at 09:00 AM.

Student number: 4911156
Project duration: October 1, 2019 – September 17, 2021
Thesis committee: Prof. dr. U. Staufer   TU Delft, supervisor
                   Dr. N. Bhattacharya   TU Delft
                   Dr. R. Norte   TU Delft
                   Dr. D. Fan   TU Delft

An electronic version of this thesis is available at `http://repository.tudelft.nl/`.

TUDelft

Abstract

This thesis is a feasibility study for the delivery of light in a flexible brain implant using 2D photonic crystal waveguides. A research gap exists in a targeted drug-delivery from the outer surface of the brain with an implant that is actuated with light. If an implant with spatial control that can release drugs in a targeted location is possible, it will provide efficient treatment for a variety of brain diseases such as strokes. This thesis investigates light as the activation stimulus and specifically aims to create a waveguide that uses photonic crystal phenomena to guide light into the brain implant. The objective is to study whether a photonic crystal waveguide can maintain its functionality under the mechanical bending imposed on the implant by the geometry and movement of the brain.

A flexible 2D photonic crystal was simulated, fabricated and tested, and its suitability for such an implant application was evaluated. Simulations were performed for a 2D photonic crystal waveguide operating with infrared light. Good light waveguiding behavior was found for metallo-photonic crystals introduced into the system as "ring-shaped" metal thin films. A transmission of 78% in a linear waveguide of 15 unit cell lengths was calculated for a flexible UV-PDMS matrix containing photoresist columns coated with 21 nm gold. The transmission bandgap range is from 1300 nm to 1650 nm with a transmission percentage shift of 78±5%. The unit cell of this design is a square lattice with 560 nm diameter pillars with 800 nm pitch. The mechanical bending of the implant is simulated as a 2D strain, and for 10% nominal bending, the peak transmission shift is ±3%. The design includes a tapered rib waveguide at the input and output of the photonic crystal for light coupling.

The device was 3D printed using two-photon polymerization. A minimum diameter of 0.30±0.02μm at a 500 nm pitch and 3.75 aspect ratio was achieved for IP-Dip nanopillar waveguide arrays. The use of photosensitive PDMS was found to be advantageous for the transfer of the printed nanopillars into a flexible matrix. The rest of the device, the coupling of the nanopillar waveguides, was printed on the same chip with 2PP for alignment accuracy. UV-PDMS was drop-casted onto the printed structures to result in: PDMS patterned to create rib waveguide couplers and the photonic crystal waveguide embedded in the PDMS matrix.

For characterization, an end-fire test setup was built and conceptually proven for transmission measurements on the fabricated devices. The experimental phase provided "real life" feedback that was used to optimize device design and fabrication.

Preface

Presented before you is my Master's thesis, the "Design and Fabrication of a Soft Photonic Crystal Brain Implant". The motivation of the project stems from the ambitious concept of placing an implant onto the brain to deliver drugs, and leads into the world of photonic crystals, electromagnetic waves, nano-fabrication and optical testing. More personally, finishing a thesis during a global pandemic has been a unique journey of travel restrictions and extended timelines. I would like to thank those who have helped me conclude on a high note.

D. Yengül
Delft, September 2021

Contents

1

Introduction

1.1. Motivation

Neuroscientists have identified a technology gap for an implant that can be used to deliver drugs to the brain. The current method uses a needle to inject into the brain, which is an invasive procedure that breaks the blood-brain barrier. A method that accesses the brain from the surface and can be controlled externally is not available. The development of such a device can advance the treatment of a number of brain diseases, such as stroke or epilepsy. The requirements for such an application have been identified as an implant that sits on the surface of the cerebral cortex and can deliver the drug to the target location in the brain at the desired time and is controlled by an external mechanism. The implant is envisioned to be a microfluidic device that has "stimuli-responsive" soft membrane pores that can be activated, i.e. opened or closed, to release the drug.[43]

The state-of-the-art in implants that are placed to the surface of the brain are electrocorticography (ECoG) devices, which are flexible implants with electrode arrays currently used to record neural activity [55]. These electrodes can be used to send electrical signals to the brain for epilepsy treatment [77] or can be incorporated with microfluidic pumps for drug delivery [58].

The use of electricity as a stimulus is not ideal due to the unpredictable spatial control [37] which will compromise the precision with which the drug can be delivered to the target location. Light is proposed as an alternative stimulus which has good spatial precision and offers flexibility in the optical path [22]. It also enables rapid actuation [70]. Light is commonly integrated into brain implants with LEDs that are placed onto ECoG devices [67]. These are spike shaped polymer waveguides that are pushed into the brain and used as probes for simulating selected regions in the brain, often for research in the field of optogenetics [37]. The integration of photonics into brain implants is a developing field with ongoing innovative research [63] and is promising for the novel approach of using it for this drug delivery application.

Photonic crystals are a promising phenomenon to realize the optical network needed for such brain implants because they can control light flow. At their simplest, photonic crystals are periodic structures that reflect certain wavelengths of light. This property is used to create waveguides: interruptions in periodicity form paths inside photonic crystals surrounded by light-reflecting edges that confine light to flow in that path. Compared to other conventional light-guiding methods, such as dielectric waveguides, photonic crystals offer the advantage of efficient light transmission even for sharp bends in the light path [46]. This feature gives design flexibility in the placement of target sites, which is valuable for a brain implant design. Literature shows that while photonic crystals have been used as implants for sensing purposes [82], there has not been a focus on using their waveguiding capabilities for light delivery in brain implants.

1.2. Optical theory of photonic crystals

The behavior of light in a photonic crystal can first be studied using optical theories. Because of the periodicity of the structure, the medium through which light propagates also changes periodically. As the light moves from one dielectric medium to the other, it experiences partial reflection and refraction at the interface [80]. The light reflected at each interface or layer of the photonic crystal interferes with each other. When the reflected waves are in phase, they interfere constructively, resulting in strong reflection [74]. A strong reflection causes the incident light to be canceled, resulting in a standing wave. In this case, the light is obstructed from propagating into the photonic crystal [44]. A visualisation of this in a one dimensional structure is shown in Figure 1.1. This is the creation of the photonic bandgap: constructive interference of the incident light and the light reflected from the alternating mediums stop light from propagating into the photonic crystal. If the reflected waves are not constructive, then the incident light propagates within the photonic crystal. This is dependent on the direction and wavelength of the incident light and is governed by Bragg-Snell's law, given in Equation (1.1) [45].

$$m * \lambda = 2 * d \sqrt{n_{eff}^2 - \sin^2 \theta}\tag{1.1}$$

In the equation d represents the periodicity of the alternating mediums, θ the angle of the light and λ, the wavelength of the incident light. The effective refractive index n_{eff}, relays the overall refractive index of a structure which is dependent on the optical values of the materials and the geometry of the photonic crystal. Bragg-Snell's law establishes the condition for constructive reflection, which states that the wavelength, or its multiple by an integer m, must satisfy correlation given in Equation (1.1). Satisfying the condition means that there exists a photonic band gap. The equation shows that the photonic band gap of a structure depends on the refractive index of the two media, the periodicity of repetition of these media and the direction of the light wave [80].
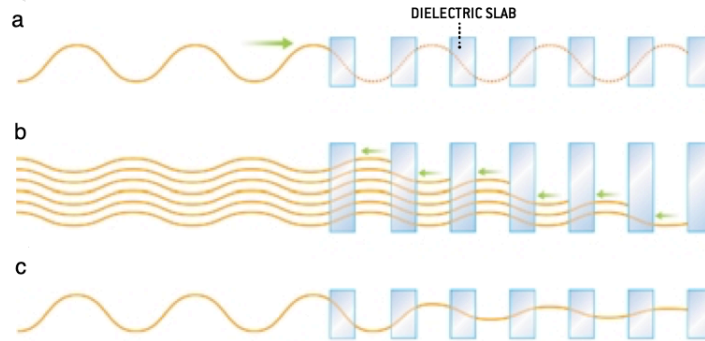
Figure 1.1: Visualisation of coherent reflection resulting in a bandgap for a 1D photonic crystal. a) 1D propagation of the incident wave within the periodic structure. b) Reflection of light in at every interface of the alternating mediums. The reflections are in phase. c) The incident wave diminishes within the photonic crystal layers, due to its interference with the coherent reflecting waves. The image is adapted from [80].

1.3. Device requirements and design parameters

The design of the implant is dependent on a range of functionalities and design parameters of the photonic crystal structure, a diagram showing how each aspect of the device is interconnected is given in Figure 1.2.

The functionalities needed for the light delivery of the drug-release-implant are:

– Photonic crystal bandgap wavelength at which the device will function

– Flexibility, for suitability for placement on the brain

– Waveguiding efficiency, delivery of light to the drug-delivery-pores

– Biocompatibility

These functionalities are controlled through the following design parameters:

– Geometry, which relays the periodic pattern,

– Periodicity, which defines the dimensions of the periodic pattern, and thus the bandgap, and

– Material choice, which determines the refractive index ratio, flexibility, and the fabrication.

These concepts serve as the guidelines that inform the formulation of this project and are evaluated in the rest of the thesis.
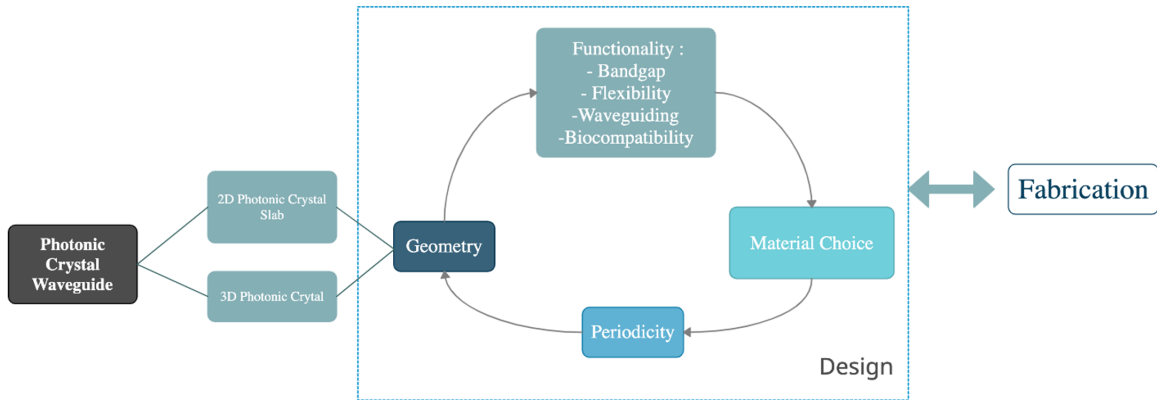
Figure 1.2: The interrelation of the fundamental parameters that make up the flexible photonic crystal waveguide.

1.3.1. Geometry and bandgap

Photonic crystals are grouped by the axis of their periodicity, that is, by the direction from which light is reflected. In 3D structures, light is confined in all three dimensions, and 3D waveguides are possible. However, they are computationally challenging. A 2D waveguide geometry is planarly periodic, and light propagates in this plane. Johnson et al. show that a 2D slab waveguide can control the propagation of light in three dimensions, which they suggest is a less complicated alternative to a 3D geometry structure that has the same guiding function [29]. However, here the light must be confined in the out-of-plane direction with internal reflection and this requires the additional consideration of the interface between the photonic crystal and the medium, such as the cladding, that it is surrounded by [8]. The 2D geometry allows the use of simpler 2D computation and lithography fabrication methods. Therefor the feasibility of using a 2D geometry is investigated for this application.

1.3.2. Periodicity and bandgap wavelength

2D photonic crystals are slabs with dielectric structures (typically cylinders) arranged periodically along a plane. The critical dimensions of the photonic crystal are the periodicity, a, the pillar radius, r, and slab height, h, which are illustrated in Figure 1.3. Bragg-Snell's law (Equation (1.1)) states that the periodicity and bandgap wavelength are directly correlated. In the infrared range, photonic crystals with a periodicity of 510 nm have been shown to have a bandgap at 1550 nm [49], whereas for a bandgap in the ultraviolet range a periodicity of about 160 nm is required. The implant that is the motivation of this thesis is designed to enable local activation of drug delivery mechanisms, with UV light opening pores and visible light closing pores [70]. However, the minimum feature size required for a UV band gap cannot be achieved using the fabrication methods available for this work (Listed in Table 1.1). Considering these feature sizes, this thesis aims for a photonic crystal bandgap in the infrared region to design a device that can be both fabricated and tested. The design is re-imagined as a mechanical drug delivery system that is activated globally with UV light and then closed locally with infrared light. However, photonic crystals are scalable, so the operating wavelength can also be scaled down if fabrication allows.
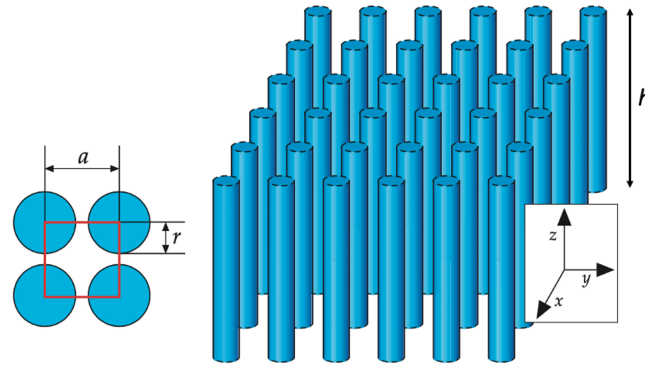
Figure 1.3: Visual representation of a single unit cell and the bulk of a two dimensional photonic crystal, with periodic cylindrical blocks. The periodicity, a, the pillar radius, r and slab height, h are labeled. Figure reproduced from [26].

1.3.3. Flexibility

The brain, like other organisms, is soft and curved [79]. The brain implant application requires the device to accommodate this curvature as well as the movement of the brain. An implant placed on the surface of the brain must have similar mechanical properties to the brain, which has a modulus of elasticity of ~1 kPa, to avoid stress and damage to the tissue [70]. The maximum bending should also tolerate the external curvature of the brain. The curvature of the cerebral cortex is estimated to have a bending radius of ~15 mm [71]. Photonic crystal application as a brain implant requires that the bandgap of the structure during bending still allows the transmission of the desired wavelength in the waveguide. Therefore, in this thesis, flexibility is a design constraint rather than a feature that provides additional functionality. The additional design considerations to ensure functionality during mechanical bending are:

- Maximizing the width of the photonic crystal bandgap.
  The fundamental property of the photonic crystal, its bandgap, is greatly dependent on the geometry of the lattice structure. Any bending alters the lattice structure and thus the bandgap wavelength range. In accordance with Bragg's law, a decrease in the lattice constant leads to a decrease in the wavelength of the bandgap [81, 56]. The mid-wavelength of the bandgap will shift as the implant experiences mechanical bending. Therefore, maximizing the bandgap range is critical to maximize the mechanical bending that the device can endure to ensure that the goal wavelength remains inside the shifted bandgap range. The size of the bandgap range is determined by the lattice constant, pillar radius and height of the slab. The radius to lattice constant ratio *r/a* needs to be optimized for the chosen materials. The size of the bandgap is optimized when the slab height to lattice constant ratio *h/a* is at ~2.25 which also determines ideal pitch ratio of the pillars [26].

- Stiffness of the chosen materials.
  In literature, the flexibility of a photonic crystal is achieved by adding a flexible layer ([83], [21], [15], [81]) or by using a flexible matrix with air cylinders [85]. However, refractive index contrast between PDMS (n=1.4,[84]) and air (n=1) is relatively low and does not result in a strong band gap region. Using the flexible matrix as the low refractive index material with high refractive index pillars embedded is not a popular design in literature. However, it appears to be an advantageous design due to its allowance of flexibility and a high refractive index contrast. In this configuration, the material choice for the pillars is not limited by their stiffness. Because the pillars are free-standing they are expected to move with the matrix itself without hindering the bending.

1.3.4. Material choice and fabrication

The final key in the design of a photonic crystal is the choice of material. The band gap, functionality, and fabrication are fundamentally affected by the properties of the chosen materials. The range and wavelength of the bandgap to be developed depend on the ratio of the dielectric constants of the two materials, with a higher contrast leading to wider bandgaps (Section 1.2). The stiffness of the chosen materials and the geometry of the structure influence the bending of the flexible photonic crystals. In addition, the materials must be biocompatible to be used in an implant. A literature review is conducted to identify potential materials for the flexible matrix and the nanopillars, focusing on materials commonly used in photonics. The material selection for the nanopillars is given in Table 1.1. The materials are evaluated based on high refractive index and biocompatibility. The availability of the methods, the ease with which they can be employed and the number of steps are the parameters used to evaluate the fabrication processes listed. Gold (Au), nickel (Ni) and gallium nitride (GaN) appear as promising materials to be further investigated for the design based on the evaluation results.

Polydimethylsiloxane (PDMS) was chosen as the flexible matrix. In a previous master's thesis, PDMS was identified as the best material to use for the prototype of the brain implants because it is biocompatible, readily available and easy to fabricate [70]. Its elastic modulus is comparable to that of the brain, so it is commonly used for brain implants such as ECoG devices [23]. Table 1.2 gives values for two PDMS formulations for which the polymerization process is initiated with different stimuli.

Table 1.1: Possible materials that can be used for the photonic crystal nanopillars. Refractive indices without citation are taken from [2].

Pillar Material	Refractive Index at 1550 nm	Biocompatibility	Fabrication	Fabrication Availability/Ease/Steps
Gold (Au)	n = 0.35755, k = 10.669[61]	+[64]	Sputter deposition with 2PP pillars	+/+/+
Nickel (Ni)	n = 2.0024 k = 4.3027[28]	+[4]	Nickel plating[62]	+/-/-
Platinum (Pt)	n = 1.7719, k = 16.193[76]	+[9]	Sputter deposition	-/+/+
Gallium arsenide (GaAs)	3.374	- [6]	Elective-area growth[60]	-/-/-
Silicon nitride (SiN)	2.2 [10]	+[50]	Masked etching[52]	-/+-/+-
Gallium nitride (GaN)	2.449	+ [24]	Elective-area growth[20]	+-/-/-
Diamond (C)	2.383	+ [35]	Diamond growth, nanoparticle doping of photoresist [19]	-/-/-
Silicon (Si)	3.476	- [5]	Deep etching[36]	+-/-/+
IP-Dip Photoresist	1.526 [38]	+ [39]	2PP	+/+-/+

Table 1.2: Material selection for the flexible PDMS matrix.

Matrix material	Refractive Index at 1550 nm	Biocompatibility	Fabrication	Fabrication Availability/Ease/Steps
Sylgard PDMS	1.3804 [84]	+	Heat curing	++/+/+
UV PDMS	1.3996 [18]	+	UV curing	+/+/+

1.4. Approach to the project

Based on the evaluation of the device requirements and design parameters, it is determined that this thesis will investigate a 2D photonic crystal waveguide with a flexible PDMS matrix for waveguiding in the IR region, which maintains light transmission under mechanical bending to function as a drug delivery implant on the exterior surface of the brain.

The first step of the thesis is to use electromagnetic wave theory to simulate the dispersion diagram of the unit cell and the transmission of light through the photonic crystal waveguide. The modeling will be performed for TM polarized light. 2D square latticed photonic crystals have a bandgap in transverse magnetic (TM) polarization when the pillars have a higher refractive index than the matrix.[26] The goal is to achieve a mid-bandgap wavelength of 1550 nm and to maximize the bandgap width.

PDMS is chosen as the material for the flexible matrix. Au, Ni and GaN are chosen as the materials with high refractive index that will be used to simulate the models.

The final design and its materials will determine the chosen fabrication method. Two-photon polymerization has been shown to be a suitable fabrication method for producing the feature sizes required for the nanopillars of the photonic crystal in the IR wavelength range. Fabrication will focus on incorporating these printed pillars with a PDMS molding process to fabricate the flexible matrix.

The final step of the thesis will focus on characterizing the photonic behavior and light guiding efficiency of the designed and fabricated implant. An end-fire coupling will be employed for testing.

$$2$$

Modelling

Section 1.3 is brought into an analytical study using COMSOL Multiphysics software simulations. The unit cell of a 2D square lattice photonic crystal is modeled to plot bandgap diagrams. The propagation of light in the waveguide made up of these unit cells is modeled to calculate transmission efficiency. Parameter sweeps are executed for the design parameters in order to determine the combinations that result in the largest bandgap and the highest transmission values. These key models are then investigated with a mechanical bending simulation to determine the transmission in the implant in its bent state and whether or not the light guiding functionality is maintained. The bending of the implant inside the brain is simulated using a stress /strain approach.

2.1. Bandgap analysis of photonic crystal unit cell

The first step in the design of a photonic crystal is to determine the dispersion diagram of its repeating unit cell. An eigenfrequency study is conducted using COMSOL Multiphysics software based on electromagnetic wave theory. The goal is to determine the design with the widest possible bandgap with which a midpoint wavelength of 1550 nm can be achieved. The widest bandgap is predicted to compensate the lattice distortion during bending, which will be discussed in Section 2.3.

2.1.1. Electromagnetic wave theory and dispersion diagrams

In order to model the behaviour of a photonic crystal unit cell, the light inside such a structure first needs to be solved as an electromagnetic wave, which are governed by Maxwell's equations. Joannopoulos et al. reformulate Maxwell's equations to reflect the periodic change in dielectric material depending on the location inside the photonic crystal [26], as given in the following equations:

$$\nabla \cdot H(\mathbf{r}, t) = 0, \qquad \nabla \times E(\mathbf{r}, t) + \mu_0 \frac{\partial H(\mathbf{r},t)}{\partial t} = 0$$
$$\nabla \cdot [\varepsilon(\mathbf{r}) E(\mathbf{r}, t)] = 0, \quad \nabla \times H(\mathbf{r}, t) - \varepsilon_0 \varepsilon(\mathbf{r}) \frac{\partial H(\mathbf{r},t)}{\partial t} = 0 \tag{2.1}$$

Here the electric, E, and magnetic field, H, of the electromagnetic wave are a function of the position, $\mathbf{r}$ and time, t. The relative permittivity, $\varepsilon(\mathbf{r})$, is a function of the position vector to express the periodically changing regions within the material. ε_0 and μ_0 are vacuum permittivity and vacuum permeability, respectively. Writing these equations as harmonic modes, $H(\mathbf{r}, t) = H(\mathbf{r}) e^{-i\omega t}$ and $E(\mathbf{r}, t) = E(\mathbf{r}) e^{-i\omega t}$ allow the behavior of light to be expressed as mode profiles, $H(\mathbf{r})$ and $E(\mathbf{r})$, independent of time [26]. Applying the harmonic modes to Equation (2.1) and following several mathematical maneuvers result in the two main equations for the electric and magnetic field of a photonic crystal given in Equations (2.2) and (2.3).

$$\nabla \times \left(\frac{1}{\varepsilon(\mathbf{r})} \nabla \times H(\mathbf{r}) \right) = \left(\frac{\omega}{c} \right)^2 H(\mathbf{r}) \tag{2.2}$$

$$E(\mathbf{r}) = \frac{i}{\omega \varepsilon_0 \varepsilon(\mathbf{r})} \nabla \times H(\mathbf{r}) \tag{2.3}$$

Now, Maxwell equations for the photonic crystal are an eigenvalue problem which also expresses the periodically changing mediums inside with $\varepsilon(\mathbf{r})$. $H(\mathbf{r})$ gives the eigenvectors and $(\frac{\omega}{c})^2$ the eigenvalues of the magnetic field.

The geometry of the photonic crystal also needs to be expressed in the reciprocal domain. The periodic photonic crystal is made up of "discretely symmetric" repetitive unit cells [26]. Vectorially, the location of each unit cell can be expressed in relation to each other with the position vector with $\mathbf{a}_1 = (a, 0)$ and $\mathbf{a}_2 = (0, a)$ for a 2D square lattice. a is the lattice constant. In the frequency domain the reciprocal wavevector, $\mathbf{k}$, is a combination of vectors $\mathbf{b}_1 = (\frac{2\pi}{a}, 0)$ and $\mathbf{b}_2 = (0, \frac{2\pi}{a})$ [3]. A square unit cell is shown in Figure 2.1a with these vectors labeled.

This reciprocal space is defined by a finite area, called the Brillouin zone, much like how a unit cell expresses the real space [32]. Within this area there exists an irreducible Brillouin zone which, as the name suggests, is the smallest component which can be used to convey the rest of the zone using symmetry. The corners of the irreducible Brillouin zone are symmetry points, labeled as Γ, M and X for a triangular area. These symmetry points are shown on the unit cell in Figure 2.1a. The maxima and minima of the eigenmodes for the photonic crystal are seen along the borders of the irreducible zone. Solving the eigenvalue problem along the wavevectors that connect these symmetry points are enough to solve the behavior of the entire structure. The solution is the dispersion diagram, an example is shown in Figure 2.1b. The horizontal axis represents the wave vector, spanning the edges of the irreducible Brillouin zone. The vertical axis is the frequency. The lines drawn along the diagram are the eigenmodes of the photonic crystal which show which frequency of light can propagate inside the structure at any given reciprocal direction. The modes that correspond to different polarizations of light waves, transverse-electric (TE) and transverse-magnetic (TM) modes, are solved separately [26]. The wavelength range at which no modes occur is the photonic bandgap. If no modes exist within a region, then light of that wavelength and direction cannot exist within the photonic crystal [73].

(a)   (b)
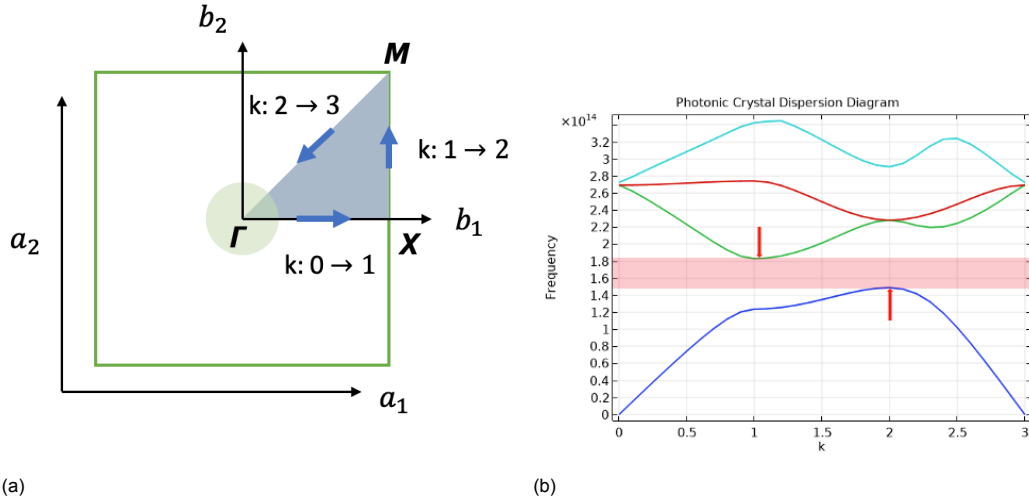
Figure 2.1: a) The real and reciprocal domain square unit cell overlapped. Γ, M and X label the corners of the Brillouin zone. The direction of the k vector, as well as the arbitrary (0-3) value assigned is shown. b) An example dispersion diagram. The y-axis sweeps the k vector from 0 to 3. The lines represent the eigenmodes of the unit cell. The red arrow is used to indicate the high and low frequency modes that border the bandgap, shown by the red region.

2.1.2. COMSOL unit cell formulation

The COMSOL Wave Optics Module solves Maxwell's equation by setting boundary conditions and meshing the geometry into small units to which the wave equations are applied to. The "Electromagnetic Waves, Frequency Domain" physics interface is used to express the unit cell of the photonic crystal and solve for its eigenmodes. The COMSOL model built is based on the modelling approaches presented in the examples from the software's application library [40][12]. The periodic pattern of the photonic crystal is applied to the model by setting "Floquet periodicity" conditions on the boundaries of the unit cell. COMSOL requires that this periodicity be expressed as a wave vector, $\mathbf{k}$, that spans the irreducible Brillouin zone for the unit cell of the photonic crystal. Using the reciprocal lattice vector expressions, the reciprocal plane locations of the symmetry points Γ, X and M are $(0,0)$, $(0, \frac{2\pi}{a})$ and $(\frac{2\pi}{a}, \frac{2\pi}{a})$, respectively. Then the x and y components of the wave vector are formulated as "if" functions to express vectors connecting these symmetry points as follows:

$$\mathbf{k}_x, k = \begin{cases} k\frac{\pi}{a}, & \text{if } 0 \leq k \leq 1 \\ \frac{\pi}{a}, & \text{if } 1 \leq k \leq 2 \\ (3-k)\frac{\pi}{a}, & \text{if } 2 \leq k \leq 3 \end{cases}, \mathbf{k}_y, k = \begin{cases} 0, & \text{if } 0 \leq k \leq 1 \\ (k-1)\frac{\pi}{a}, & \text{if } 1 \leq k \leq 2 \\ (3-k)\frac{\pi}{a}, & \text{if } 2 \leq k \leq 3 \end{cases} \tag{2.4}$$

Here, the numerical value assigned to the constant k is arbitrary and is chosen as 0 to 3. Solving the boundary condition varying the value of the wavevector constant sweeps the entire irreducible Brillouin zone and yields the dispersion diagram of the unit cell. The "Eigenfrequency" solver of the software is used to plot the dispersion diagram, which finds an eigenvalue, or light frequency value, for each k value. The model is set to search for frequencies around the goal bandgap midpoint, which is 193.41 THz (1550 nm wavelength). The electric field component is input as a perpendicular vector to the plane of the photonic crystal slab to solve for the TM polarization mode.

2.1.3. Design parameters and bandgap behavior

Three main designs of the square lattice unit cells were chosen to be studied: a classical photonic crystal with dielectric pillars, metal pillars, and photoresist pillars with a metal ring coat; all in a photosensitive PDMS matrix. The choice of materials was presented previously in Section 1.3.4. The dielectric pillar is modeled with GaN and the metal pillar with Ni, their unit cell is shown in Figure 2.2a. Au and Ni are the materials considered for the ringed model, shown in Figure 2.2b. The use of photoresist IP-Dip pillars as the coated pillars stems from the fabrication results to be discussed in Section 3.3.2. The refractive index values are taken from Table 1.1, calculated for 1550 nm wavelength. The thickness-dependent refractive index data of thin-film Au is given in Appendix A.1. A parameter sweep for the design variables are solved ranging:

- Lattice constant, a: 500 nm to 1400 nm

- Radius ratio, r/a: 0.2 to 0.4

The range of the lattice constant is determined based on the values given in Section 1.3.2, which inform the dimensions required to achieve a bandgap at the target wavelength of 1550 nm. The midpoint and width of the bandgap are examined to decide which parameter sweep combination is most advantageous for the waveguide device.
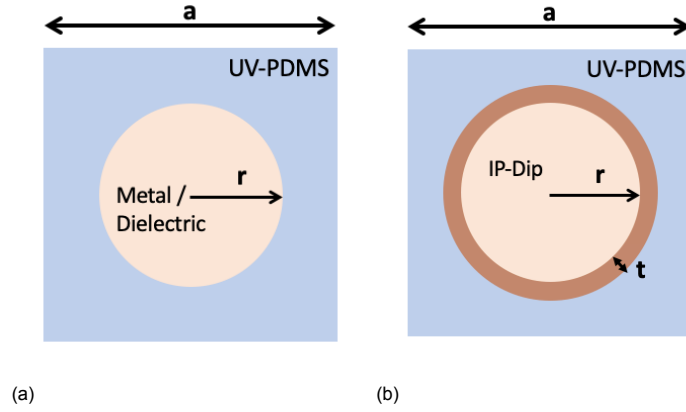
Figure 2.2: a)Unit cell with a metal or dielectric pillar, the materials modeled are GaN and Ni. b)Unit cell with a photoresist pillar with metal, Ni or Au, ring. Both unit cell matrices are UV-PDMS. a is the lattice constant, r pillar radius, t ring thickness.

Dielectric unit cell

The first unit cell design is modeled using GaN, a common semiconductor material, as the material for the pillar. Performing the parameter sweep on this model shows that the refractive index difference between the matrix (n=1.3996) and the pillars (n=2.449) is not large enough to produce a wide bandgap. The dispersion diagram for a unit cell with 500 nm lattice constant is shown in Figure 2.3a. In the figure, the red arrows indicate the upper and lower modes that determine the bandgap, showing that the wavelength range is 1550 nm±150 nm. This model shows that a simple dielectric design is insufficient for this photonic crystal application, and so the investigation was continued using metallic materials.

This design was also used as a preliminary model to confirm the validity of the unit cell analysis. In Figure 2.3b, the mid-wavelength of the bandgap increases when the lattice constant is increased to 700 nm, as expected based on the theory presented in Section 1.2.
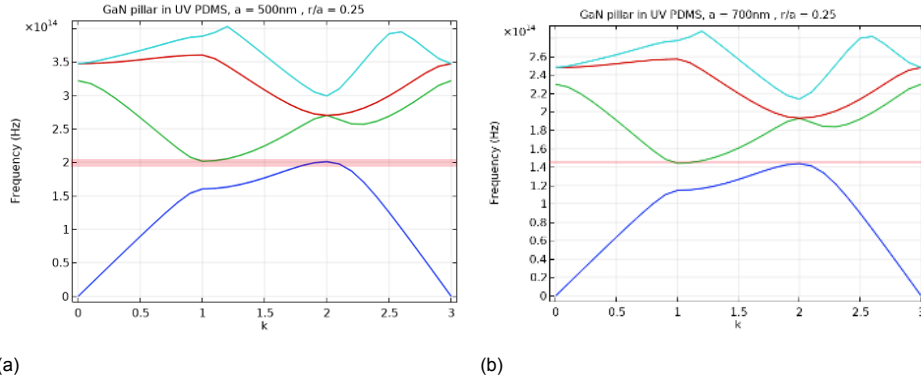
Figure 2.3: Dispersion diagram for GaN pillars in UV-PMDS. Radio to lattice constant ratio is 0.25. Lattice constants are a) 500 nm and b) 700 nm. The red zone is the bandgap. Red arrows indicate the top and bottom modes of the bandgap.

Metallo-photonic crystal unit cell bandgap behavior

Incorporating metal into the photonic crystal is advantageous because of the large negative refractive indices and the variety of fabrication possibilities [30]. They are reportedly good reflectors in the infrared region [42]. However, they are dispersive materials and especially in the infrared region their extinction coefficient must be taken into account [75]. Due to their dispersive behavior and submicron fabrication difficulties, metallo-photonic crystals are not extensively studied in the IR region [42]. Figure 2.4 is given as an example of the bandgap formation in the nickel-based unit cell models, calculated for TM polarization. The metallo-photonic crystal is seen to have a cutoff frequency below which light cannot propagate, resulting in a large bandgap range [26]. This is also called a plasmon bandgap because it occurs below the plasma frequency of the metal [42]. A second bandgap, formed by dielectric contrast, is also observed in a higher frequency range.

Literature on the use of a thin film of metal in a photonic crystal structure is not common. There is a study of 2D photonic crystal metal "tubes" consisting of cylinders connected at the bottom, but they are designed to function as absorbers [7]. The simulation results show that a bulk metal pillar, Figure 2.4a, and metal ring unit cells, Figure 2.4b, lead to similar bandgap behavior, but the bandgap wavelengths are shifted. It can be deduced that thin film coated structures exhibit similar photonic behavior to bulk metal intrusions and therefore represent a promising design alternative that can create new fabrication opportunities.

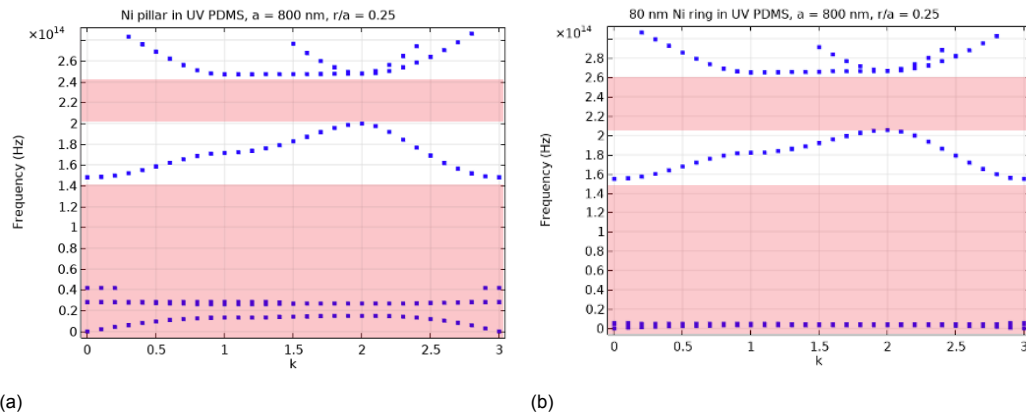(a)   (b)

Figure 2.4: Dispersion diagrams for Ni unit cells in PDMS with lattice constant 800 nm and r/a = 0.25. a) Nickel pillar. b)80 nm Nickel ring around photoresist pillar. Red regions indicate the bandgap ranges, where the low frequency bandgap is the plasmon bandgap.

2.2. Light propagation through a photonic crystal waveguide

A waveguide within a photonic crystal is created by introducing defects that disrupt the periodicity in the structure. Within a photonic crystal, a defect leads to the localization of light. The disrupted symmetry means that the light wave is confined within the defect and cannot propagate into the periodic structure [26]. Modelling the transmission efficiency of light through the waveguide is key to predicting the losses of the device. Plotting the transmission spectrum also provides information about the width and range of the bandgap where light is transmitted in the waveguide.

2.2.1. COMSOL model for light propagation

In COMSOL, the propagation of light in the photonic crystal waveguide is evaluated using a 2D model. The entire device cannot be simulated due to the computational power required to do so. Instead, light transmission in a 15 unit cell long waveguide with a missing pillar line defect is modeled. The electromagnetic wave module is used to define a plane wave incident along the input boundary of the waveguide. The incident wave is set to have an electric field amplitude perpendicular to the periodic plane of the photonic crystal to solve for TM polarized light. COMSOL's "scattering boundary" condition is used to ensure that no reflection is modeled at the boundaries of the model. The transmission of light through the waveguide is calculated by taking the integral of the power outflow across the input and output boundaries. The model is solved for a wavelength range from 1100 nm to 2000 nm in the near-infrared range, to plot the transmission spectrum.

2.3. Transmission through the waveguide in mechanical bending

The main goal of this thesis is to investigate the feasibility of using photonic crystal waveguides for a brain implant that must withstand the mechanical bending it will experience when placed on the brain due to the curvature and movement of the brain. Figure 2.5 is a visualization of the curved state of the waveguide at its implanted location on the brain surface. This section focuses on explaining how the waveguiding function of the implant is affected by this mechanical bending. A 2D model is built to relate the bending experienced by the waveguide to strain that alters the periodicity of the unit cells.
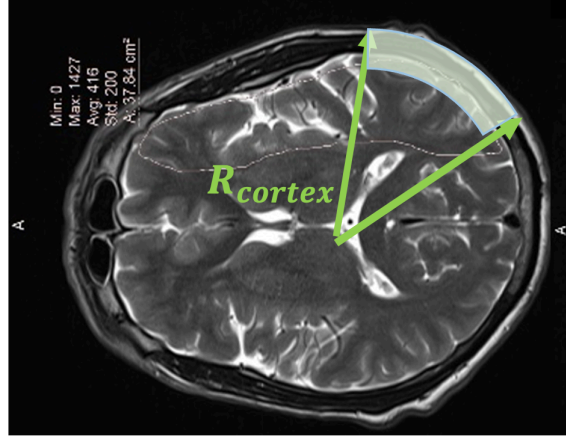
Figure 2.5: Image showing an axial brain MRI, with the visualization of the brain implant placed on the surface. The deformation experienced by the implant due to the bending radius of the cortex, **R**$_{cortex}$ is seen. The implant size is not to scale.

2.3.1. 2D approach to slab curvature and COMSOL formulation

The effect of mechanical bending on the bandgap of the photonic crystal has already been discussed in Section 1.3.3. In this section, the distortion of the unit cell of a photonic crystal slab is theorised using the 2D beam bending model. This approach is used to explain the bending in a flexible 2D photonic crystal slab as a "stretch" of the lattice structure [21]. Placed on the brain, the implant experiences tension at the top and compression at the bottom. This deformation is shown in Figure 2.6a. The midpoint of the slab thickness is a "neutral axis" where the lattice structure is assumed to remain unchanged. The 3D visualisation of the flexible device in its bent state is also shown in Figure 2.6b. In this state, the bending radius, R, can be estimated as a function of the length, l, the thickness, h, and the strain, $\frac{\Delta l}{l}$, that it experiences as given Equation (2.5), which is derived by expressing the bend as a sinusoidal function for simplicity [53].

$$R_{nom} = \frac{l}{2\pi\sqrt{\frac{\Delta l}{l} - \frac{\pi^2 h_S^2}{12l^2}}}$$ (2.5)

When a material experiences elastic deformation, its optical behavior also changes [79]. However, this photoelastic effect is assumed to be negligible in these calculations to simplify the simulations and the refractive index of PDMS is assumed to be isotropic. Furthermore, any change in shape that might alter the circular nature of the pillars are disregarded because the pillars are expected to be tilted and not bent when the flexible matrix is bent.

(a)   (b)

Figure 2.6: a) Beam bending model illustration, showing the stress and compression at the top and bottom of the implant. a_0 is the neutral axis. h labels the height of the susbtrate and R the bending radius. b) Bent flexible device with the change in length $l - \Delta l$, bending radius R and the applied force is labeled. The image is adapted from [53].

2.3.2. Simulation of transmission through the waveguide in mechanical bending

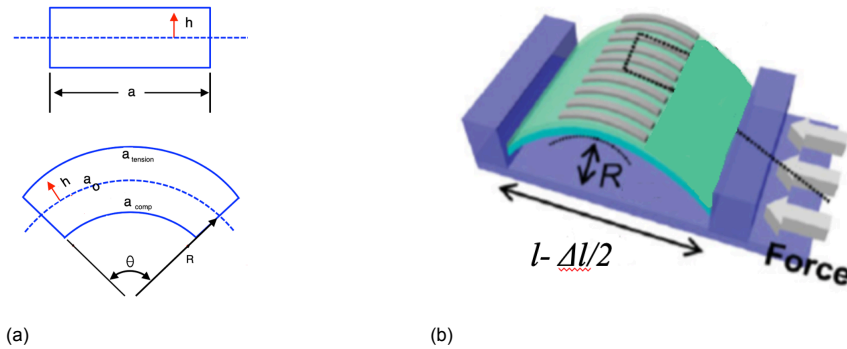COMSOL simulations of transmission are performed with strained lattice structures to model the propagation of light inside the mechanically bent waveguide. In the strained state, the photonic crystal waveguide consists of rectangular unit cells. To reflect this deformation, the geometry is changed so that the lattice constants of one side of the unit cell is $a \pm \Delta a$ along the propagation direction. The change in light propagation when the lattice is deformed by bending is shown in Figure 2.7. The inlet of the figures show the deformed unit cells that make up the waveguides. The transmission of light in the non-bent state, or in the neutral axis, of the implant is shown in Figure 2.7b. It is expected that the maximum deformation and thus change in transmission occurs at the top, Figure 2.7a, and bottom, Figure 2.7c, of the implant.

(a)   (b)   (c)
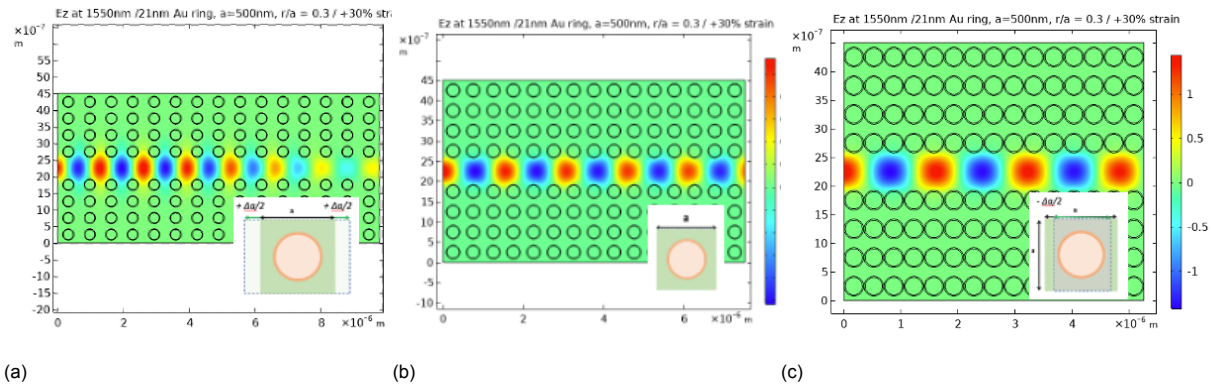
Figure 2.7: Comparison of propagation of out-of-plane electric field inside the waveguide in its initial and mechanically bent states. The simulated model is the 21 nm Au coated IP-Dip pillars in UV-PDMS design, with a=500nm, r/a=0.3. The inlets show the deformed unit cells. Deformation occurs only in the direction of the strain and one side is extended by $\pm \Delta a$. a) Simulation of the top of the implant where the waveguide is strained by +30% along the defect line, transmission is 27%. b)Simulation of the neutral state of the waveguide transmission is 62% c)Simulation of the bottom of the implant where the waveguide is strained by -30% along the defect line, transmission is 67%.

2.4. Simulation findings

The results from the COMSOL unit cell and transmission simulations are correlated and analyzed to finalize the design that will be used to fabricate a prototype device. The data from the simulations are reported in detail in Appendix A. A large number of possible designs emerge from the simulations. "Key" designs for each material combination are selected to report the findings in a condensed form, summarized in Table 2.1. These key designs are: the model with the widest bandgap region calculated in the unit cell analysis, the model with the highest transmission peak at 1500 nm, and the model with the widest transmission peak at the mid-bandgap wavelength of 1550 nm, respectively denoted as 1,2,3 in Table 2.1, for each material combination. The table also comments on "fabricability", a term that reflects the availability of resources, the expertise required, fabrication methods previously given in Table 1.1, and the overall performance of the bandgap behavior.

Key Models	Lattice Constant (a)	r/a	Pillar diameter (d)	Bandgap Width x10^{14}Hz	Transmission At 1550nm	Evaluation Fabrication/Waveguide
A- GaN pillars						-/-
	500 nm	0.25	250 nm	1.9-2.1	21.31%	
B- Ni pillar						+- /-
B.1	500 nm	0.3	300 nm	0-2.9	17.50%	
B.2	800 nm	0.35	560 nm	0-2.2	43.04%	
B.3	1000 nm	0.2	400 nm	0-1 1.6-1.8	54.38%	
C - IP-Dip pillar with 80 nm Ni Ring						–/+-
C.1	600nm	0.25	300 nm	0-2.2	19.09%	
C.2	800 nm	0.25	400 nm	0-1.6 2-2.6	42.56%	
C.3	1000 nm	0.35	700 nm	0-1.8	46.01%	
D- IP-Dip pillar, 21 nm Au ring						+/++
D.1	600 nm	0.30	360 nm	0-2.8	64.39%	
D.2	800 nm	0.35	560 nm	0-2.3	78.46%	
D.3	1200 nm	0.3	720 nm	0-1.1 1.4-1.8	63.59%	
E. IP-Dip pillar, 11.7nm Au Ring,						+/+
E.1	500 nm	0.35	350 nm	0-3.1	33.01%	
E.2	800 nm	0.35	560 nm	0-1.9	62.46%	
E.3	1300 nm	0.35	910 nm	1.6-2.0	76.58%	

Table 2.1: Key models summary of simulation results. The table gives the data for lattice constant (a), radius ratio(r/a), pillar diameter(d), bandgap width $\Delta\omega$, transmission percentage and evaluation of fabrication and bandgap properties.

2.4.1. Metallo-photonic crystals

Metallo-photonic crystals exhibit interesting bandgap properties. The data obtained from the unit cell and transmission simulations are evaluated to draw conclusions about the effect of metal addition, photonic behavior for the ring design, and the effect of varying ring thickness.

Effect of metal on photonic crystal behavior

Figure 2.8 compares the dielectric GaN pillar design (key model A in Table 2.1) with the 80 nm Ni-ringed photoresist pillar design (key model C), both with the same pitch distance and pillar diameter. Direct conclusions between the structures cannot be drawn as the pillar materials used are not the same, but some comparison is possible. The addition of a metal structure changes the bandgap significantly and results in a much larger bandgap being formed for the same dimensions as a dielectric photonic crystal. This is also evident in the comparison of the transmission spectra given in Figure 2.8b, where the transmission is much higher and extends over a broader wavelength range instead of a narrow transmission peak as in the dielectric case. The dimensions and bandgap wavelength are consistent with the literature, where a 2D metallo-photonic crystal is calculated to have similar bandgap wavelengths at 500 nm pitch distance [69].

(a)   (b)   (c)
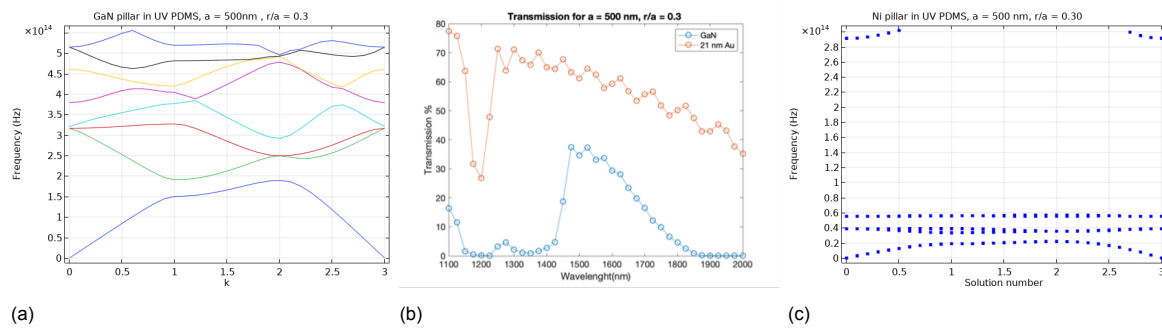
Figure 2.8: Bandgap diagram and transmission of a = 500 nm, r/a = 0.3 unit cells models. a)The calculation for dielectric GaN pillars. b) Transmission spectrum for both structures. c)The bandgap for photoresist pillar with a 80 nm nickel coat.

Effect of metal ring thickness

The thickness of the metal thin film in the ring designs (key models C, D and E from Table 2.1) is studied as a design parameter. In Figure 2.9, the transmission of the waveguides with 11.7 nm and 21 nm gold coatings is compared, while the other design parameters are kept constant. The graphs show that the transmission behavior does not experience any significant changes as the ring thickness is varied. The peak transmission remains at 1550 nm. The significant difference is in the transmission efficiency, which appears to decrease by 20% at the goal wavelength with an 11.7 nm thick ring, compared to that of 21 nm. This is a comparison between only two models for gold rings, so no conclusions can be made about the general effect of metal ring thickness on transmission without simulations for more ring thicknesses. However, for this application it is more advantageous to use a coating of 21 nm.

(a)   (b)
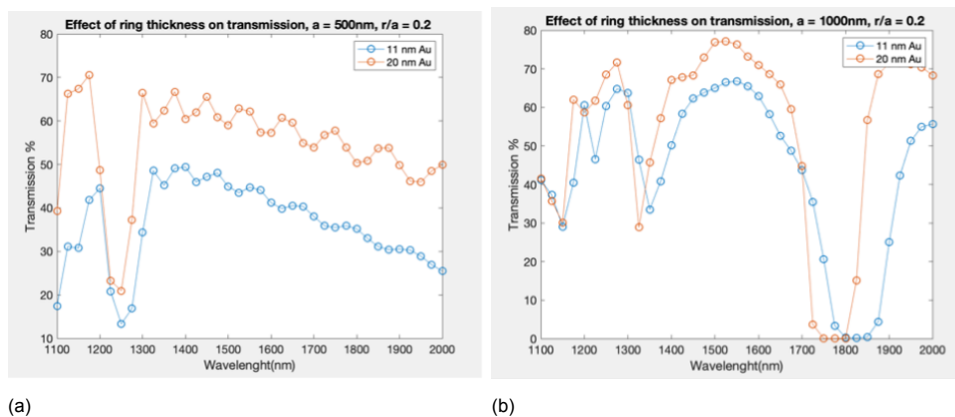
Figure 2.9: Effect of Au thin film thickness (11.7 and 21 nm) on the transmission spectrum of the Au coated IP-Dip pillars in UV-PDMS designs. a)Lattice constant,a, 500 nm and radius to lattice constant ratio, r/a, 0.2 b) a=1000 nm, r/a = 0.2

2.4.2. Comparing transmission in mechanical bending

The key models for the 21 nm Au-coated pillar design are used to compare the bandgap and transmission values reported in Table 2.1, along with the results of transmission simulations of the strained state of the waveguides. For simplicity, the key models are labeled as D1, D2, and D3 for the dimensions of 600 nm to 0.3, 800 to 0.35, and 1200 nm to 0.3 for lattice constant and radius, respectively. The key model D1 is chosen because it shows the largest bandgap in the unit cell analysis, D2 because of the large transmitted wavelength width in the waveguide model, and D3 because it has the highest transmission.

The dispersion diagram simulation of model D1 exhibits the widest bandgap range, shown in Figure 2.10b. At its unbent state, the measurements show 64% transmission at 1550 nm. The bandgap in transmission is very wide ranging from 1450 nm to 2000 nm with a transmission percentage ranging from 70% to 55%. The effect of a 10% strain is clearly visible when Figure 2.10a is analysed. The graph shows that compression shifts the valley in transmission to a lower wavelength. For tension, this valley is shifted up to 1550 nm, resulting in a significant decrease in transmission in this state.

Model D2 was chosen because of its high transmission rate and large bandgap in the transmission simulations. The transmission in the unbent state is 78%. At a strain of 10%, Figure 2.11a, the transmission shifts by only ±3%. The graph shows that the strained state of the device still maintains an overall bandgap range between 1400 nm to 1700 nm. However, at a strain of 20%, Figure 2.11c, transmission of the waveguide in compression drops to 22%, while in tension it remains unaffected.

Model D3 exhibits the highest transmission rates in both the initial and bent states. At 10% strain, as shown in Figure 2.12a, the transmission remains unchanged in tension and compression for a high transmission of about 80% at 1550 nm. However, the shifts experienced by the transmission peaks are very large across the transmission spectra. This means that the transmission can be kept very high with careful design, but is much more sensitive to changes in strain. The narrow transmission peak can shift below or above the desired wavelength due to strain. This is consistent with the dispersion diagram, Figure 2.12b, where the bandgap region is also narrow.

Overall, the transmission and bandgap models validate each other. A large bandgap range in the unit cell analysis also results in a large transmission range in the waveguide simulations. This is very apparent by comparing Figures 2.12a and 2.12b to Figures 2.11a and 2.11b. As expected, a wide transmission range in the initial unbent configuration provides good compensation for the mid-bandgap wavelength shift that occurs with applied strain.

In general, the transmission percentage increases in compression and decreases in tension. This is expected to be directly correlated to the change in the length of the waveguide: The shorter the light path, the less loss it will experience as it propagates. However, the shifts in the transmission peaks are still valuable results. Looking at Figures 2.10a and 2.11c, it can be commented that the transmission is more significantly altered in the stretched state. This will mean that more loss at the top of the implant is expected.

Figure 2.10: Transmission and dispersion diagram calculations for Key model D1, a =600, r/a = 0.3. b) Dispersion diagram. a) Transmission in neutral axis, bending and compression for 10% strain. c) Transmission in neutral axis, bending and compression for 20% strain.

Figure 2.11: Transmission and dispersion diagram calculations for Key model D2, a =800, r/a = 0.35 b) Dispersion diagram. c) Transmission in neutral axis, bending and compression for 10% strain. c) Transmission in neutral axis, bending and compression for 20% strain.
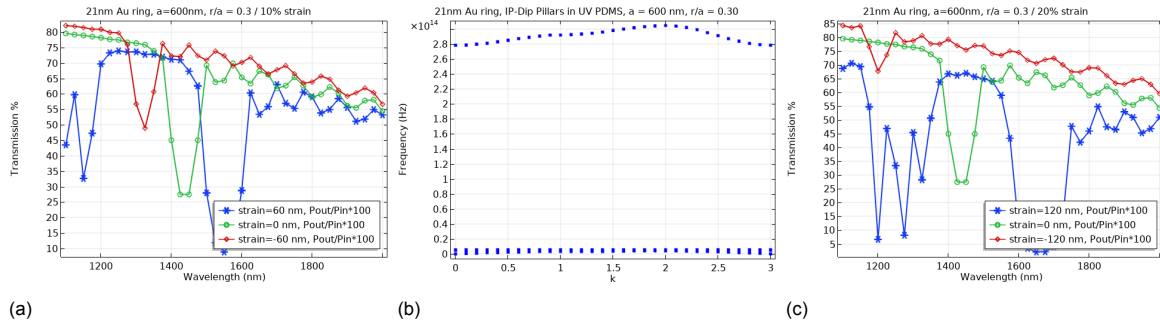

Figure 2.12: Transmission and dispersion diagram calculations for Key model D3, a =1200, r/a = 0.3 b) Dispersion diagram. c) Transmission in neutral axis, bending and compression for 10% strain. c) Transmission in neutral axis, bending and compression for 20% strain.
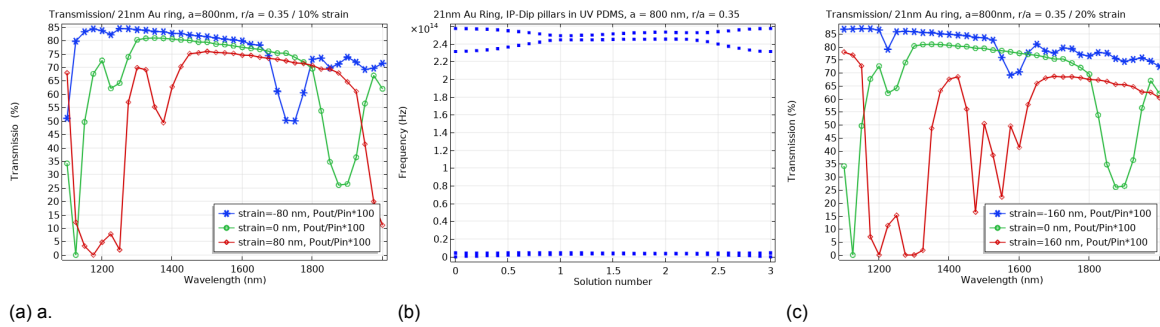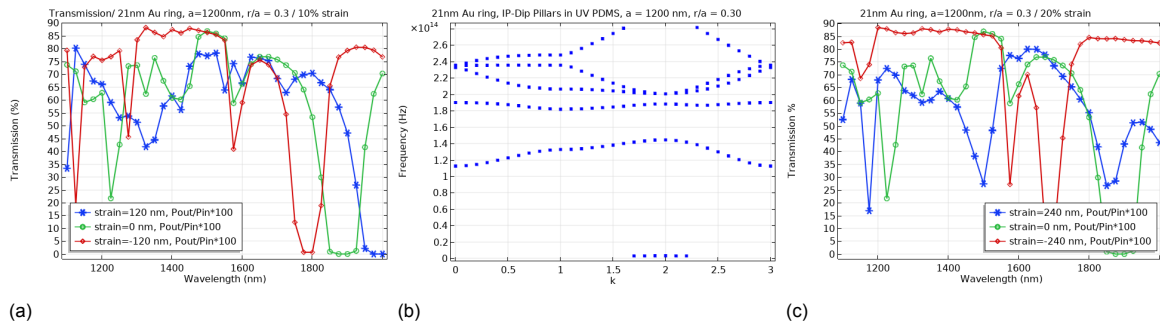
2.5. Simulation conclusions

The simulations have led to many different photonic crystal designs that exhibit waveguiding function for the flexible brain implant. The most promising model appears to be the UV-PDMS matrix with 21 nm gold-coated photoresist pillars.

The use of a metal ring gives the photonic crystal a good bandgap abilities and leads to varied fabrication possibilities, as thin film metals can be fabricated in many ways. Gold appears to have excellent transmission while Nickel is unfavorable, which is in agreement with literature which states that the bandgap in Nickel is weakened by absorption [75].

Analysis of the simulation data shows that there are a large number of combinations of the design parameters that result in models that exhibit the desired waveguide functionality. Key models were identified for simplification. The model with lattice constant of 600 nm and a radius-to-pitch constant of 0.3 exhibits the largest bandgap simulated using dispersion. Transmission simulations show that the waveguide maintains a transmission of 78% to 65% at 20% strain. This corresponds to a nominal bending radius of 2.671 μm for the simulated waveguide of 15 unit cells. The height of the waveguide is taken from Section 3.1.1. The model with a lattice constant of 800 nm and a radius ratio of 0.35 has a transmission of 78.46±3% at 10% mechanical bending. The nominal bending radius of the device is 6.044 μm. Compared to the curvature of the brain (∼15 mm), the bending radii for which the transmission calculations are performed are much smaller. According to these calculations, the transmission loss of the implant due to placement on the surface of the brain will be almost negligible.

The models should also be considered in terms of the fabrication tolerances that will come into play outside the world of simulations. It is difficult to detect or control the deposited thickness of a gold coating. However, the results show that this thickness only changes the transmission efficiency, not the bandgap or transmission behavior. This allows for a margin of error in the fabrication of the gold film.

Similarly, a margin of error should be considered in the fabrication of the nanopillars. The simulations proved the sensitivity of the bandgap to changes in the dimensions of the unit cell. This can adversely affect transmission if the dimensions of the pillars are not fabricated exactly. The transmission spectra plotted to show the effect of varying the pillar diameter (r/a), are given in Appendix A.5.

Overall, the 3 key models with the gold-coated photoresist nanopillars embedded in UV-PDMS showed interesting behavior that is promising to be further investigated through fabrication and testing.

3

Fabrication

This chapter describes in detail the fabrication methods and procedures used to produce the prototype photonic crystal waveguide device. The fabrication of the device includes the printing and development processes for two-photon polymerization (2PP) of nanopillars and waveguide structures, metal coating and PDMS molding. A flowchart for the fabrication steps is given in Figure 3.1. The fabrication protocol is listed in Appendix B.1.
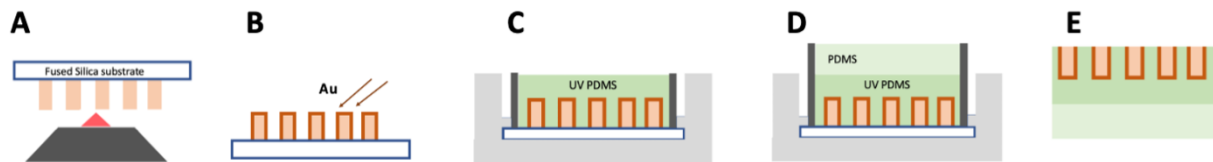
Figure 3.1: Steps of the fabrication process of the photonic crytal waveguide prototypes.1) 2PP printing of the photoresist nanopillars arrays and waveguide structures. 2) Gold thin film layer deposition with sputtering. 3)Placement of the substrate into the sample holder, drop-casting of UV-PDMS and UV exposure. 4) PDMS pour as the cladding layer and heat curing. 5) Release of the device from the fused silica substrate and sample holder.

3.1. Two-photon polymerization

Two-photon polymerization (2PP) is a 3D fabrication method that uses the theory of two-photon absorption to polymerize photosensitive resists in submicron feature sizes. In this thesis, a Photonic Professional GT 3-D Laser Lithography System from Nanoscribe (Germany) was used for printing. Equipped with a femtosecond pulsed 780 nm wavelength laser with a laser repetition rate of 80 MHz and a pulse length of 100-200 fs, the device prints "voxels" by polymerizing the smallest possible volume at the focal point of the laser beam. The voxel size depends on the dose, which is adjusted by the laser power and the scan speed [47]. To print the smallest possible feature sizes, Nanoscribe utilises a 63x objective (NA = 1.4, Carl Zeiss, Oberkochen, Germany), which is used to focus the light in Dip-in Liquid Lithography (DiLL) mode, where the objective is immersed in the resist. Theoretically, the planar resolution of the objective is 340 nm [14]. The writing field has a diameter of 200 μm. IP-Dip (Nanoscribe, Germany) is a negative tone resist that has a refractive index of 1.552 nm in its polymerized state. It has high resolution printing capability when used with fused silica as the substrate on which the structures are printed [38]. In this project, it is used to print the base of the photonic crystal waveguide devices, the nanopillars of the photonic crystal and the coupling structures.

3.1.1. Nanopillar fabrication using 2PP

Based on the dimensions of the photonic crystals analyzed in Section 2.4, pitch distances are printed for different diameters for a range between 0.5 μm and 1.4 μm. The aspect ratio of the nanopillars is set to 3.75. This is a value from literature showing that maximizing the bandgap width of the photonic crystal slab is related to the ratio of height and pitch [26]. An "under-size" approach is taken and the pillars are taken to be 85% smaller in diameter in the CAD models to mitigate the slightly larger voxel size.

CAD model for the waveguides

Figure 3.2 shows the computer-aided design (CAD) of photonic crystal waveguide designs made up of nanopillars, with an s-shaped line of missing pillars forming the path of the waveguide. The design choices of the waveguide are further discussed in Section 4.3.2. The entire waveguide is printed in a single exposure field instead of printing each pillar individually, which significantly decreases the printing time. This means that the maximum size of the waveguide is limited by the print field that can be exposed by the 63x objective to avoid stitching. The printed array sizes are 40 μm x 40 μm, 40 μm x 60 μm, and 30 μm x 120 μm.
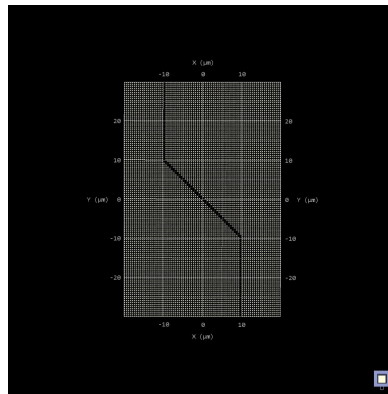

Figure 3.2: CAD design of the nanopillar arrays with a missing s-shaped line of pillars that make up the waveguide in the Describe software, the dimensions are 60 μm x 40 μm.

Recipe for Nanoscribe

Nanoscribe's software Describe is used to process the 3D CAD model for printing [48]. The CAD model is divided into horizontal (slicing) and vertical (hatching) lines, which the printer recognizes as the geometry to be exposed. Describe generates a .gwl file (the printer's General Writing Language format) that defines the writing parameters and recipe for the trajectory of the laser while printing.

Extensive dose testing (shown in Appendix B.3,Appendix B.4) was performed to determine the printing parameters that would achieve the target dimensions of the pillars. A successful dose was found with 0.02 μm hatching distance, 0.1 μm slicing distance, and a laser scanning speed of 1500 μm/sec and 20±1% laser power. Laser power is a more sensitive parameter, which also depends on the power scaling condition of the laser at the time of printing. Therefore it needs to be adjusted accordingly.

Sample development

The sample development process is as important as the printing parameters to achieve defect-free pillar arrays. Experiments have shown that nanopillars tend to collapse onto each other after the standard IP-Dip development process, leading to defects in the periodic arrays. In a previous work, it was found that the main factor of pillar collapse is the capillary meniscus force that occurs between two pillars when they are immersed in the developing fluid [57]. The pillars collapse on each other when they are removed from the developer to dry, due to the high surface tension difference between the liquid and air. The surface tension, and thus the force to which the pillars experience, can be reduced by immersing the structure in an additional liquid with low surface tension before drying. The use of Novec 7100 Engineered Fluid (Sigma-Aldrich, Germany) as a low surface tension solvent solved the collapse problem and enabled the printing of reproducible and defect-free pillar arrays. Some of the other sample development methods that were explored are detailed in Appendix B.5.

The final development procedure for defect-free pillars is as follows: Before printing, the fused silica substrate is first cleaned with acetone, then isopropanol, followed by 10 minutes in the plasma cleaner for surface activation. These steps are taken to obtain defect free prints and for better adhesion of the pillars to the substrate surface. After printing, the unpolymerized resin was removed by first being placed in 1-methoxy-2-propanol acetate (PGMEA) (Sigma-Aldrich, Germany) for 40 minutes followed by isopropanol (IPA) (Sigma-Aldrich, Germany) for 10 minutes. Finally, it is placed in Novec for 30 seconds and dried using an air gun. Due to the susceptibility of the nanopillars to collapse, they are developed horizontally in each solution. Care must be taken to ensure that the sample is placed from one solution to the other as quickly as possible to avoid contact with air. During drying, the pressure of the air gun must be kept low and the air must be pointed perpendicularly towards the center of the print area.

3.1.2. Coupling structures

The photonic crystal waveguide is connected at its input and output to a PDMS tapered waveguide, which serves as a light coupling structure. The two-photon polymerization technology enables the fabrication of the tapered waveguide on the same substrate as the nanopillar arrays. This is an advantageous strategy because the high-resolution printing allows for easy and accurate alignment, minimal fabrication steps, and customizability in the designs. All 2PP features of the device are printed during the same print job. The fabrication strategy is to polymerize the most critical feature, the pillars, first and then to print the coupling structures. Nanoscribe is equipped with a positioning system controlled by the Describe software which is used to code the position of these structures to ensure that the inlet and outlet ports are aligned. Figure 3.3 shows the CAD model of one of the taper designs, as well as the model of the print job showing the tapers aligned at both ends of the photonic crystal waveguide. The print parameters are 0.2 μm hatching distance and 0.3 μm slicing distance at a scanning speed of 40000 μm/sec for 65% of laser power. Larger hatching and slicing values were chosen in comparison to the pillar printing parameters because these structures are comparatively larger and do not require the same degree of precision. The dimensions of the various printed tapers are further discussed in Section 4.2.2. The purpose of the printed 2PP structures for the light coupling is to serve as a mold with which to pattern the PDMS; therefore, the negative of the rib waveguide is printed.

(a)   (b)
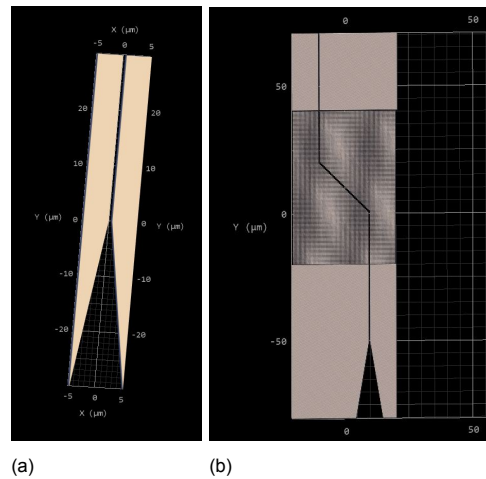
Figure 3.3: 3D CAD designs of the example coupling structures printed using 2PP. a) Image of a free standing mold design of tapered rib waveguide attached with a straight waveguide. b) Image of the entire nanopillar array and coupler that is printed. One port of the photonic crystal waveguide is attached to a tapered rib waveguide while the other is attached to a straight rib waveguide. The alignment of the inlet and outlet of each structure is done using the Describe software.

3.2. PDMS molding

Patterning of PDMS with nanofeatures is a subject of extensive study in nanofabrication. In the initial formulation of the device design, the printed nanopillars were meant to serve as a mold that would pattern the PDMS slab with cylindrical holes. Experimental results showed that a more novel fabrication method could be used: The nanopillar structures tend to detach from the substrate and remain embedded in the PDMS when photosensitive PDMS was used. This can be explained by the small surface area the substrate and pillars are in contact with each other. This result was adopted and the goal of PDMS fabrication became to have the gold-coated photoresist pillar arrays in a PDMS matrix. It was observed that the waveguiding structures, which have a much larger surface area, did not detach from the substrate and functioned as molds. The experiments also showed that the gold layer acted as an "anti-stick" layer between the fused silica and the PDMS, allowing the PDMS to be easily peeled off the substrate without tearing.

3.2.1. PDMS molding methodology

After two-photon polymerization, the next step in fabrication is to deposit gold in a thin film to create the ring around the pillars. The samples are placed in the sputter coating chamber at a 45°angle to coat the sidewalls of the pillars. After each cycle of deposition, the sample is rotated 90°so that the metal is sputtered more uniformly around the sidewalls. The sputtering parameters are 20 mA for 5s for each cycle, resulting in a gold thin film of 20 nm. These parameters are chosen based on the data sheet of the sputter coater (Sputter Coater JEOL JFC-1300) and its deposition rate. However, it is expected that the thin film thickness estimation is not very accurate using this fabrication method. The gold-coated sample is then placed in the sample holder. The design of the sample holder is discussed in Section 4.3.1.

The UV-PDMS (KER -4690, micro resist technology GmbH, Germany) is prepared under yellow light to avoid starting the curing process. Equal weights of base and curing agent (KER -4690 A and B) are mixed in a tinted glass bottle with a magnetic stirrer for 1 hour. The mixture is then placed in a desiccator for 1 hour to remove air bubbles form during stirring. The desiccated mixture is drop-casted onto the 2PP structures placed inside the sample holder. The height of the holder determines the height of the PDMS cast. The samples are then placed in the desiccator again for 1 hour, this time to ensure that the liquid flows and settles in the small air gaps of the printed structures. For curing, the samples are placed in the UV chamber (Photopol Light, Dentalfarm, Italy) for 40 minutes. The PDMS is left in the sample holder for at least 2 hours after curing before it is removed and peeled off the fused silica substrate.

3.3. Results and discussions

The 2PP structures and PDMS molds were analyzed using an optical microscope (Keyence Digital Microscope VHX-6000, Japan) and a scanning electron microscope (Jeol JSM-6020LA SEM, Japan). Important aspects studied were the dimensions of the 2PP structures, the uniformity of the nanopillar arrays, the alignment of the coupling structures, the quality of the molded PDMS device, and the definition achieved with the molds.

3.3.1. Characterization of the pillar dimensions

The dimensions of the nanopillar arrays are carefully chosen to ensure that the photonic crystal waveguide exhibits the designed bandgap functionality, as detailed in Chapter 2. Therefore, fabrication of nanopillars with the target diameter and arrays with uniformity is an important aspect of the creating functional waveguides. In SEM imaging, the dimensions of the pillars are analyzed at a magnification of x20000 by measuring the diameter of 5 pillars and taking the average of the distance across a line of 10 pillars. The height of the pillars is measured at a 45°angle and the actual height is calculated.

For a fixed lattice constant, ranging from 500 nm to 1400 nm, and a radius to lattice constant, r/a =0.3, the effect of dose on the pillar dimensions is studied. Figure 3.4 shows the SEM measurements made on the model with a 500 nm lattice constant with pillars of 250 nm diameter, printed with %1 change in laser power while the scan speed was held constant. The pillars printed with the lower laser power have a diameter of 0.30±0.02 μm with a height of 1.17 μm, Figure 3.4a. The r/a ratio is 0.3. At higher laser power, Figure 3.4b, the pillar diameter increases to 0.33±0.04 μm with a height of 1.43 μm.

The r/a ratio increases to 0.33. This indicates that laser power is a sensitive printing parameter that allows pillar dimensions to be adjusted with a high degree of accuracy and leads to the ability to print a wide range of different r/a ratios. This ability to adjust pillar size by varying the dose was performed for a wide range of pitch distances, and only the smallest feature size achieved has been detailed here as it was the most difficult design to achieve. Further examples of the printed pillars can be found in Appendix B.2.

(a) (b)
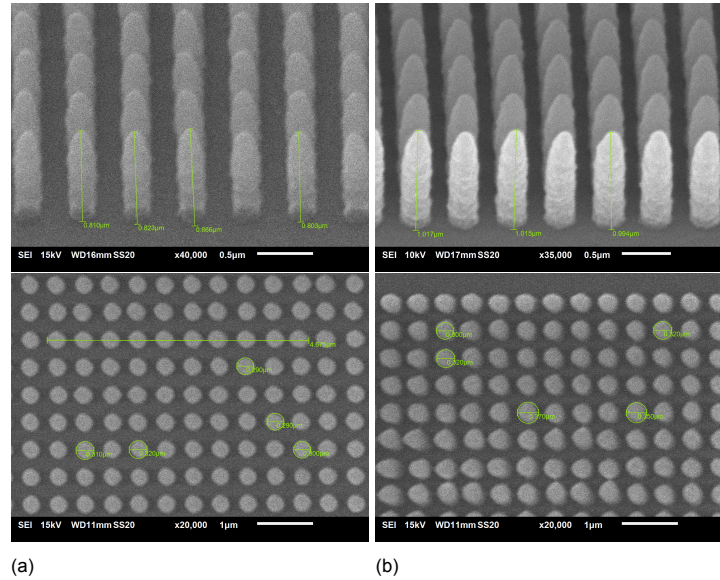
Figure 3.4: SEM images showing two doses of a nanopillar array with 500nm pitch, printed with a CAD design of 250nm diameter pillars with 3.75 aspect ratio. The tilted images are taken from a 45° angle. The scanning speed is constant at 1500 μm/sec. a) The print with 20% laser power. The measured pillars have a diameter of 0.30±0.02 μm and 3.9 aspect ratio. b)The print with 21% laser power. The measured diameter is 0.33±0.04 μm. The measured aspect ratio is 4.33.

Another goal of the project was to print the longest possible waveguide while keeping inside the 140 μm limitation of the printing field. Using the stitching feature of the Nanoscribe tool to divide the print into smaller arrays resulted in shifts in the periodicity. Therefore, it was important to maximize the length of a single print. It was observed that longer arrays were much more sensitive to changes in laser power and defects. This is consistent with the research of Nouri-Goushki et al. who have visually demonstrated that a smaller array size results in more uniform pillar fabrication [51]. It was also found that the larger array areas need to be polymerized at a 1% higher dose to achieve the same pillar size as the smaller arrays. Figure 3.5 shows the uniform range of nanopillar array lengths that were printed by making use of these findings, with the maximum length achieved being 130 μm. The maximum length achievable was observed to be critically related to the condition of the alignment and tilt of the Nanoscribe, and some of the problems faced due to this are detailed in Appendix B.6.

(a) (b) (c)

Figure 3.5: SEM images of the printed nanopillar arrays with 300 nm diameter with a lattice constant of 500 nm. a) Waveguide length 40 μm b) 60μm c)130 μm.

3.3.2. Viscosity of PDMS

The decision to use UV-PDMS in the final device was based on experiments conducted with different PDMS materials. Due to the very small air gaps between the 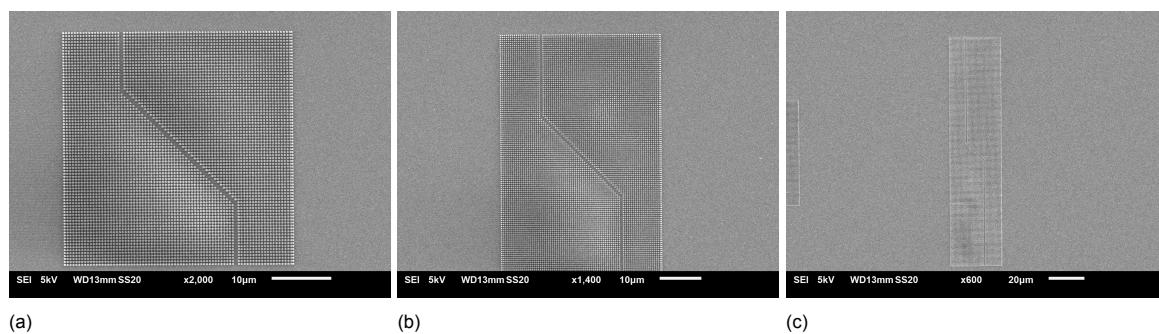pillars, the smallest distance being 200 nm, it was important to investigate how PDMS with different viscosities would flow around the nanopillar arrays and mold the 2PP structures. Sylgard 184 PDMS, prepared conventionally and as a solution with toluene as thinner, and UV-PDMS were evaluated. The viscosity of Sylgard 184 PDMS is 3.5 Pa·s at a 10:1 ratio of its base solution and curing agent [68]. The addition of toluene to the Sylgard 184 mixture as a diluent is presented by Koo et al. and their methodology is used [34]. The viscosity of UV-PDMS is 2.7 Pa·s and is reported to have a molding resolution of 100 nm [72].

Figure 3.6a shows the surface of the Sylgard 184 PDMS slab after being peeled off from the substrate. It can be seen that the viscosity of Sylgard 184 is too high to penetrate the gaps between the pillars, so only very shallow patterns were achieved. In Figure 3.6c PDMS diluted with 20(wt)% toluene shows that although parts of the pillars have detached from the substrate and are embedded in the PDMS, other areas of the PDMS are defected with the pillars still attached to the substrate. Increasing the weight percentage of solvent to 60% was also unsuccessful. It appeared that the increased amount of solvent interacted negatively with the photoresist material or the gold layer, resulting in the formation of wave shaped defects on the surface, as shown in Figure 3.6d. It should also be noted that the use of a solvent requires additional fabrication steps and safety measures in the preparation of PDMS. While toluene is expected to evaporate from the solution during degassing, it is unknown whether or not the resulting PDMS material is biocompatible. Ultimately, the use of UV-PDMS showed the most promising molding results as evidenced by the uniform surface shown in Figure 3.6b, indicating that the pillars are inside the matrix.
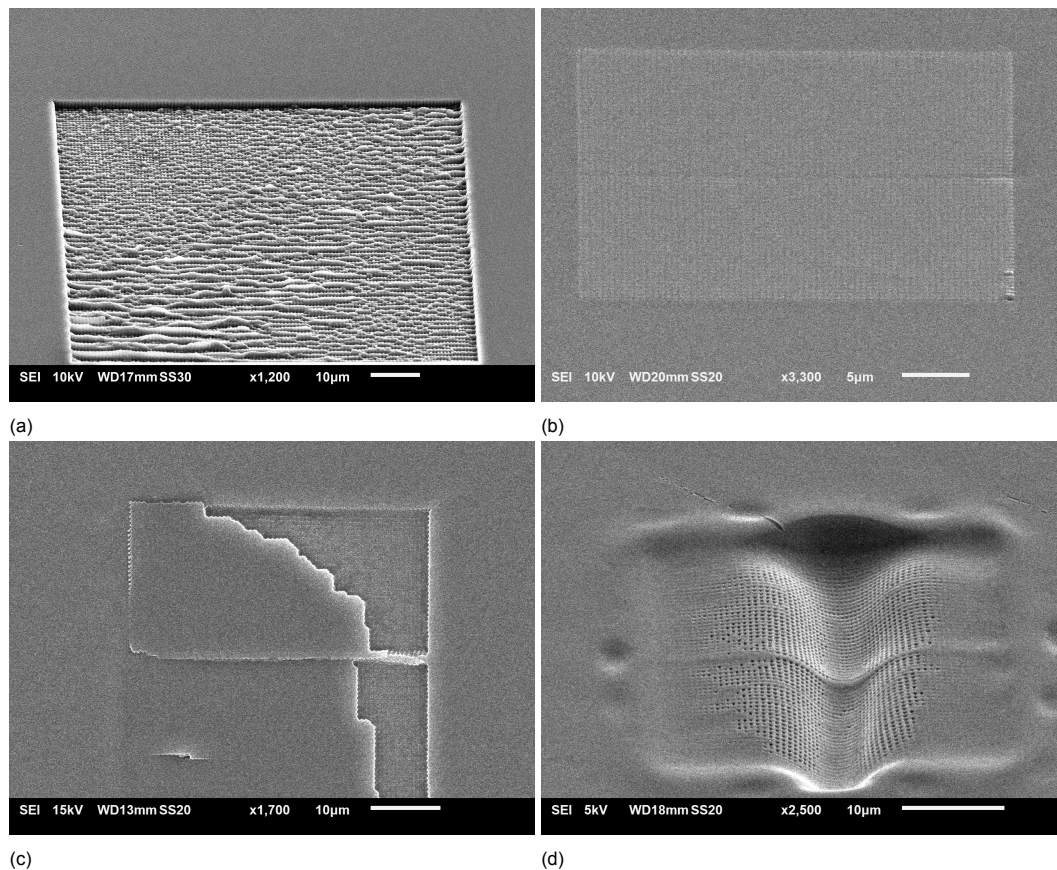

Figure 3.6: SEM images showing PDMS surface after molding. a) PDMS used is Sylgard 184 PDMS. b) UV-PDMS c)Sylgard 184 PDMS diluted with 20% Toluene. d)Sylgard 184 PDMS diluted with 60% Toluene.

Confirmation of the transfer of pillars and the accuracy of the patterning of the PDMS cast was done by optical imaging. The absence of pillars on the substrate after peeling off the UV-PDMS was a clear indicator of that the pillars are detached. In addition, the peeled UV-PDMS exhibited photonic behavior, to be explained in Section 4.1, indicating that the pillars were embedded inside. This can be seen by comparing the surface of the peeled UV-PDMS, Figure 3.7b, and the substrate after peeling, Figure 3.7a. The defective print in the lower left corner clearly shows the visual difference between transferred and remaining pillars underneath the optical microscope because the pillars on the substrate and in the PDMS both interact with light.

(a)   (b)
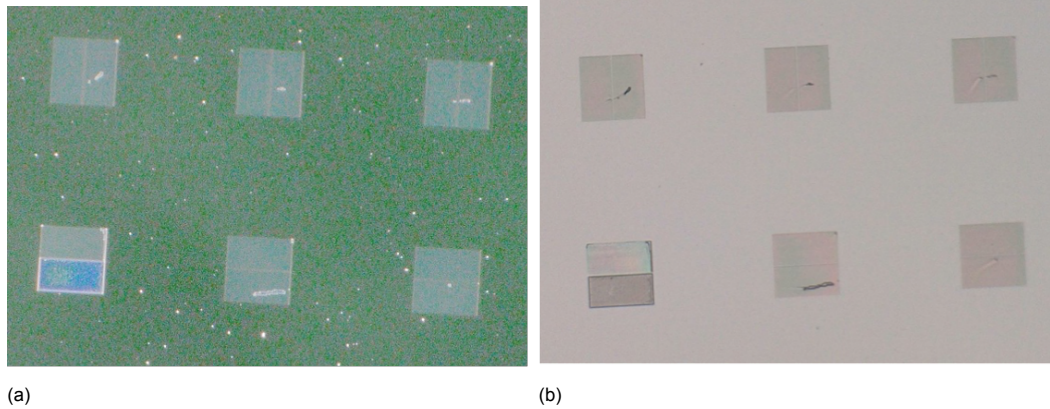
Figure 3.7: a) Image of fused silica substrate after UV-PDMS molding, showing the absence of pillars except in the bottom left corner. b) UV-PDMS cast after being peeled off the substrate, showing pillars embedded in the matrix. Regions that appear colorful are due to the pillar arrays interracting with light.

3.3.3. Alignment and mold definition of the waveguide structures
The accuracy of the alignment of the coupler waveguide to the photonic crystal waveguide is critical to the transmission efficiency of the device. Misalignment during the printing of the structures will lead to losses in the coupling of light. Similarly, defects in the definition of the PDMS mold will result in further losses in the device. The two 2PP prints of the entire device with the nanopillars and the tapered waveguide molds at each end are shown in Figure 3.8. The SEM image is of the alignment of a 700 nm wide waveguide inlet. It shows the level of accuracy with which structures can be printed using the Nanoscribe software and its high-resolution alignment capabilities.

(a)   (b)
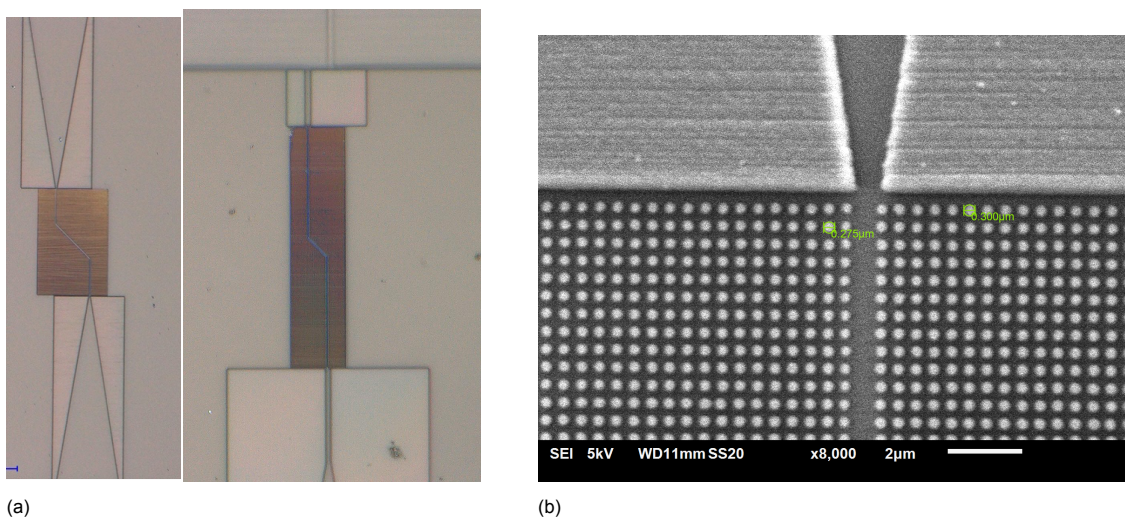
Figure 3.8: a) Optical images of the coupling structure designs printed with alignment to the inlet and outlet of the photonic crystal waveguide. b) SEM image focused on the coupling region between the photonic crystal and the waveguide mold structure showing the accuracy in alignment. The width of the photonic crystal waveguide and inlet of the tape is 700 nm.

The molding of the coupling structures is shown in Figure 3.9. Figure 3.9a is the SEM image showing that the PDMS has been patterned to produce the tapered waveguide along with the embedded pillar arrays. The 2PP molds of the coupling structures remain attached to the substrate while the pillars are peeled off, as pictures by the image of the substrate after the PDMS is peeled in Figure 3.9b.

(a)   (b)
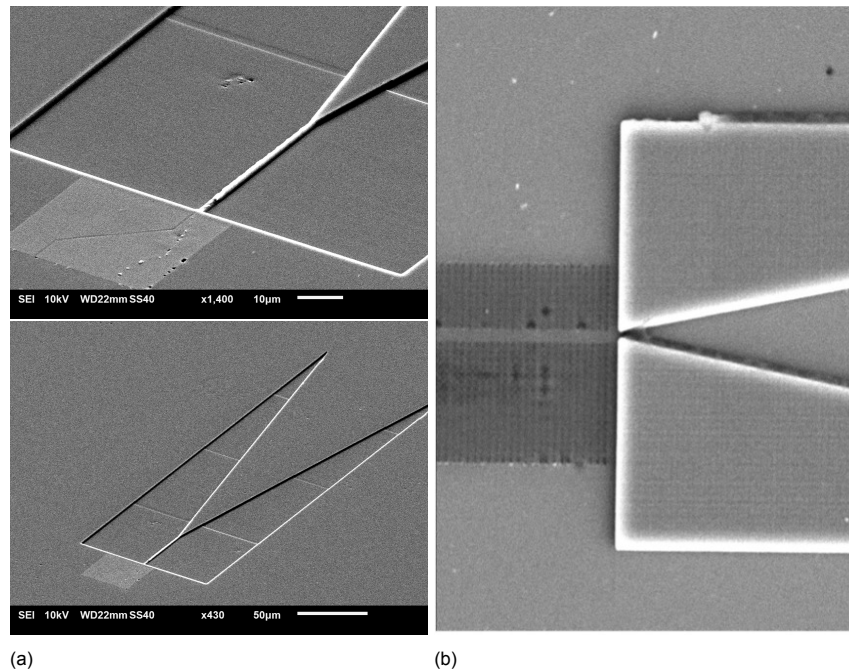
Figure 3.9: a) The optical microscope and SEM image of the surface molded PDMS showing embedded pillars and PDMS rib waveguide with a rib waveguide with 700 nm width. b) Fused silica substrate after PDMS is peeled off, showing the remaining coupling structure molds and missing pillars.

4

Characterization of the implant

This section details the investigation into characterizing the photonic bandgap and transmission of the flexible waveguide device that is fabricated. The photonic behavior of the pillars is characterized optically. A light coupling system consisting of a tapered rib waveguide is designed and simulated. An end-fire test setup is built for experimental characterization and the validity of the coupling system is investigated. The observations obtained through the experiments are used as critical feedback in determining the final device design and fabrication process, as well as identifying the weak points of the project. These are detailed in this chapter as results of the characterization.

4.1. Optical characterization of photonic behavior

When analyzed through an optical microscope, the nanopillar arrays exhibit photonic behavior: That is, they appear brightly colored even though the polymerized resist is transparent and regular 2PP structures appear grey under the microscope. This behavior is not surprising, since the nanopillar arrays as printed are simply dielectric pillars in an air matrix and thus are photonic crystal structures. Figure 4.1 shows the optical microscopy images of pillars that vary in pitch distance and dose while the pillar diameter is kept constant. It can be clearly seen that each print reflects a different color when viewed under white light. The color the pillars appear corresponds to the fundamental relationship between the pillar size, periodicity, and bandgap wavelength of photonic crystals as well. As the periodicity of the pillars decrease, the colors of the arrays change from violet (short wavelength) to bluish green to orange (long wavelength). This is as expected: decreasing the r/a constant should increase the wavelength at which the photonic band gap occurs. Similarly, increasing the dose leads to larger pillars and thus an expected increase in the wavelength of the bandgap. This is most clearly seen in the middle row of the figure, which shows the color shift of the pillars from violet to blue to green. The photonic behavior of the printed waveguides and their agreement with the theory explained in Section 1.3.2 is confirmed. This feature was a valuable tool in evaluating individual printed samples. By linking the SEM measurements to the color that the nanopillars appeared to have, this property was used to visually confirm the dimensions of each printed sample. It was also used to evaluate the uniformity of the pillar sizes across the waveguide print. It is also noteworthy that photonic behavior was observed on the surface of the PDMS coated pillars, as previously shown in Figure 3.7.
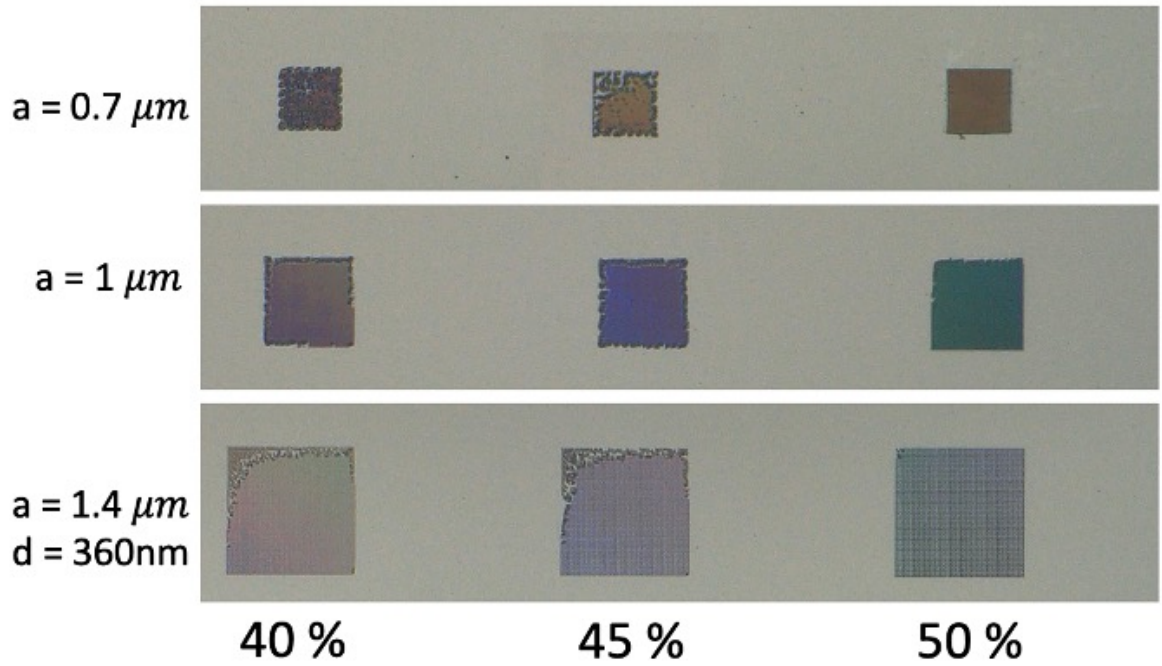
Figure 4.1: Optical microscope images of a dose test for 360 nm pillars, printed with 13600 μm/sec scan speed. The y axis ranges the pitch distance, a, and the x axis ranges the laser power.

4.2. Light coupling for experimental characterization

An optical test setup is designed and built to characterize transmission through the simulated and then fabricated photonic crystal waveguides. A free-space optics approach with end-fire coupling is chosen as this is the most straight-forward experimental method to implement [11]. This method is suitable to be used in combination with a tapered waveguide structure where the light is coupled in-plane [66]. It should be noted that the scope of this thesis did not include the complete optimization of the coupling system. A simplified approach was taken in order to have a functional coupling for testing the photonic crystals. The test was designed for the non-bent position of the flexible device only. A diagram of the waveguide device and light delivery system can be seen in Figure 4.2.
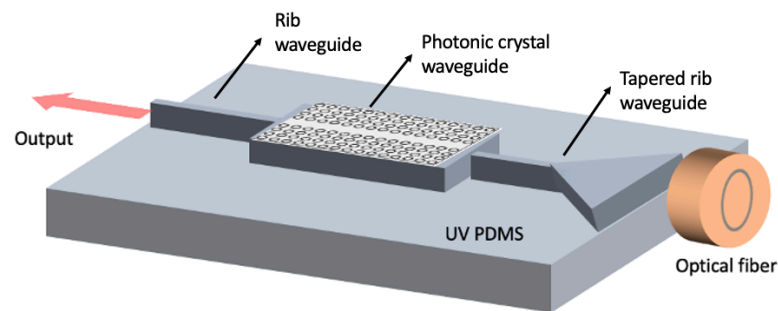
Figure 4.2: Diagram of final waveguide device showing the photonic crystal structure with the tapered rib waveguide at its input. The PDMS cladding is shown. Optical fiber is in-plane to the waveguide for end-fire coupling.

4.2.1. End-fire testing

Many different methods can be used to couple light into a photonic crystal device with optical fibers. Two proposed methods are a Bragg's grating, where light is delivered into the system at an angle, and an end-fire coupler where a tapered waveguide is used to couple light from the same axis as the light propagation direction. [66] End-fire coupling is implemented because it is a simple approach that requires relatively less expertise. The basic working principle of the system is to deliver and collect light from the input and output of the device that is being tested by delivering light with an objective of suitable numerical aperture and magnification [66].

Light path, equipment and alignment of test-setup

Figure 4.3 shows an image of the test set up that was built. Each component that was utilised is labeled. The 1550 nm infrared laser source (Single Mode Fiber Coupled, S1FC1550, Thorlabs) is connected to a collimator via an optical fiber patch cable (P1-1550A- FC, NA =0.13, Thorlabs) to ensure that collimated beams are delivered to the system. The polarization of the optical fiber is controlled with a manual polarizer (3- Paddle Polarization Controllers, FPC561, Thorlabs), to get TM polarization. The light path leads to a 10x (N=0.18, Leitz- Wetzlar) objective that focuses light into the inlet of the sample, which is mounted on a 3D printed sample holder. The mode field diameter, a measure in a single-mode fiber that takes into account the fraction of light that leaks into the cladding, is $10.4 \pm 0.5 \ \mu m$ [65]. This means that the output of the objective has an estimated spot size of $\approx 1.0 \ \mu m$ at the focal point. A 20x objective (NEO SPlan, N =0.4, Olympus) is placed at the output of the waveguide.

In the setup, a total of four cameras are used to align the objectives to the device and measure the output light intensity. A USB microscope is placed perpendicular to the sample holder to obtain a top view of the waveguide and light propagation. An IR-camera is placed in line with the objective to capture the transmitted light. Due to the considerable size of the IR-camera, the light output path, consisting of the objective, lens, and camera, is kept stationary. The initial alignment of the system is done with red light, as the visible detection of the light path greatly facilitates this process. Visible light is delivered using a laser source with a wavelength of 635 nm (Single Mode Fiber Coupled, S1FC635PM, Thorlabs). The output facet of the device is aligned to the objective using the translation stage. Alignment is done visually: a camera is used to capture a live image of the objective, and the distance of the sample holder from the objective is changed until the image is in focus. Since the IR-camera is in line with the objective, a flip mirror is used to change the path of the light, delivering it to the visible light camera. Once the position of the sample is set, the input objective is aligned following the same steps. To deliver light into the device and collect the back reflection with the camera, the laser source is connected to a beam splitter/mirror component where the light is split in the propagation direction into the objective and in the back reflection into the camera. The details of the test setup and equipment can be found in Appendix C.1.
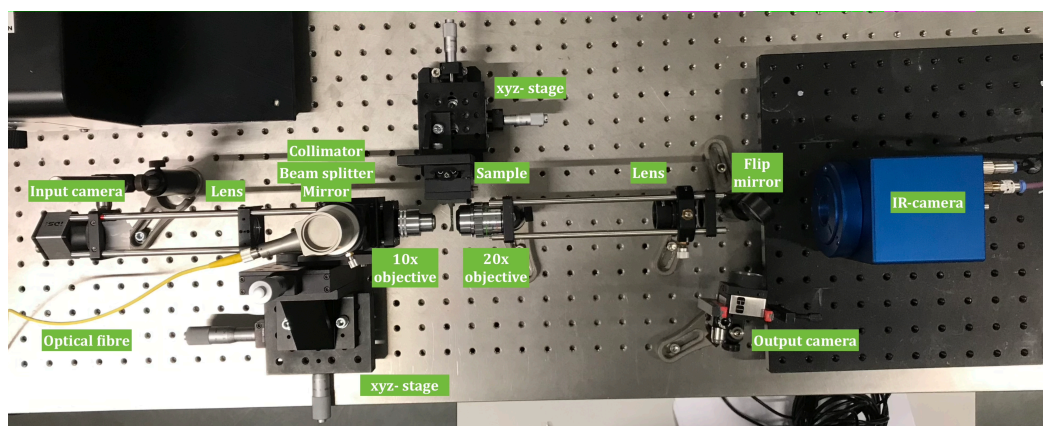

Figure 4.3: The end-fire test set up that was built for this thesis is pictured. Each component is labeled. The light path is from the laser source to the IR-camera.

4.2.2. Light coupling with a tapered rib waveguide

A tapered waveguide structure decreases in width from the inlet, where the fiber is coupled to, towards the input of the photonic crystal(<1 μm). This allows the inlet area to be as wide as desired, making coupling easier. The taper also serves to lower the optical mode of the fiber in increments as light propagates into the smaller mode of the photonic crystal waveguide, increasing transmission efficiency [11]. The coupling waveguide is designed to be complimentary to the fabrication process followed for the photonic crystal structures. The obvious answer for this was found to be utilizing a rib waveguide structure design: the core of the waveguide and the layer to which it is attached are made of UV-PDMS. The structure is printed and PDMS is molded in the fabrication steps previously described in Section 3.1.2 and Section 3.3.3. The visualization of such the tapers attached to the photonic crystal waveguide was given in Figure 4.2.

Design of the tapered waveguide

FEM analysis is used to create a simple and versatile design for tapered waveguides that can be adapted to the needs of the optical testing. The goal is to determine the angle with which the waveguide tapers, to focus the light into the inlet of the photonic crystal waveguide. The design can be adapted to create waveguides with different lengths and inlet widths if the taper angle is kept constant. The same COMSOL study from Section 2.2.1 is applied to this geometry and calculations are done for TM polarization. For the simulations, the inlet width is chosen as 10 μm and kept constant, while the length is varied with a parameter sweep. The output width of the taper is set to be equal to the width of the photonic crystal waveguide input. In the model, the taper couples into a straight rib waveguide of 10 μm length. Figure 4.4 shows the change in propagation of the electromagnetic wave inside the taper waveguide when the taper angle is varied. The coupling and transmission increase with a gradual decrease in width. For the 8.4°taper, Figure 4.4b, the fully formed wave propagation in the rib is evident and the transmission is calculated as 65%. The COMSOL transmission data for the complete taper angle sweep are given in Appendix A.6. The inlet width of the taper for the final device was determined by feedback from the experimental results as 100 μm, which is further explained in Section 4.3.2. This was the final dimensions used to design and fabricate the tapers previously discussed in section 3.1.2.
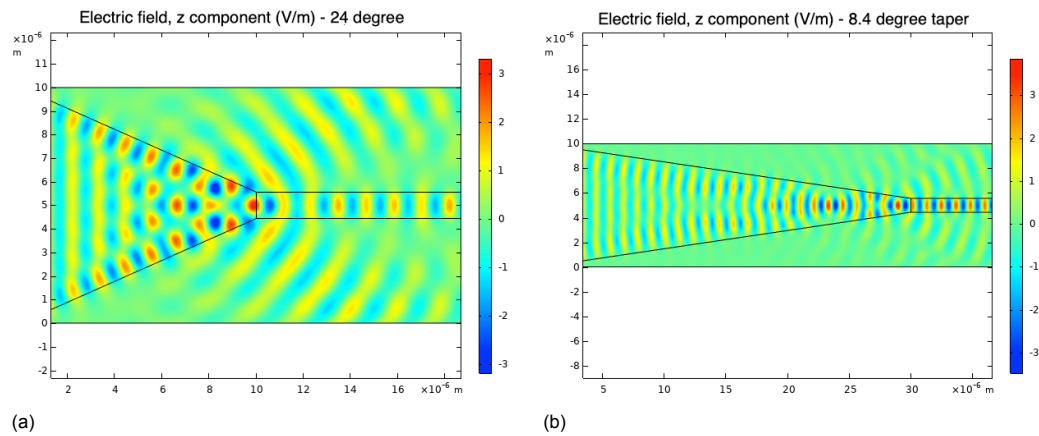
Figure 4.4: COMSOL simulation of the electric field(V/m) component perpendicular to the propagation field is plotted for TM polarized light in a UV-PDMS waveguide with 24°(a) and 8.4°(b) tapers. Inlet and outlet widths are kept constant while the taper length is varied. The taper waveguide is attached to a straight waveguide.

Mode coupling in the rib waveguide and cladding layer

So far, all the considerations of the device have been planar and the direction perpendicular to the plane in which light travels was assumed to be confined by internal reflection. However, the coupling of light into the taper waveguide requires 3D consideration. A rib waveguide relies on internal reflection to confine light in the core or rib region. Typically, a high refractive index material makes up the core, which consists of the "rib" extrusion and the layer beneath it [16]. The core is index confined at its top surface by air. Its bottom surface is confined by a low refractive index material layer. The tapered coupler designed for the test setup is a rib waveguide with a UV-PDMS core and bottom layer.

A COMSOL analysis is performed to model the first mode of the light propagating inside the narrowest section of the rib waveguide. The dimensions of the tapered rib waveguide are determined in part by the dimensions of the photonic crystal, since they are fabricated together. The core height of the rib waveguide is set equal to the height of the pillars. Similarly, the narrow output of the taper is equal to the width of the photonic crystal inlet waveguide. The "Mode Analysis" study is used to search for the effective refractive index in the cross-sectional area of the waveguide. The study is solved searching for an "effective mode index" of 1.39. The electric field in the direction perpendicular to the propagation plane is solved and plotted to obtain the mode shape of the coupling of TM polarized light. The simulation results for a photonic crystal inlet with a lattice constant of 1000 nm are given in Figure 4.5. Figure 4.5a shows a rib waveguide with a bottom layer height of 1 μm without an additional cladding layer. Here it can be seen that most of the light is localized in the bottom layer of the waveguide, which significantly hinders the transmission efficiency. A solution to this is presented by Kee et al. [31], who add an additional layer of lower refractive index PDMS to the bottom of the cladding and show that a small difference in refractive index between the two layers results in light coupling into the rib. The use of PDMS is interesting because it allows the flexibility of the structure to be maintained. This method is adapted to the materials used in this thesis: the rib and its bottom layer is made of UV-PDMS (n= 1.3996 at 1.55 μm) and the cladding is chosen as Sylgard 184 PDMS (n = 1.3804 at 1.55 μm). Figure 4.5b, shows the 1 μm rib layer attached to the PDMS cladding. The image shows that the localization of light towards the rib is improved, but the light still also propagates in the bottom layer, which is expected [13]. This enhancement, and thus the coupling of light into the rib, is very dependent on the height of the UV-PDMS layer: Figure 4.5c shows that when the layer is increased to 8 μm, the light is almost entirely found in the cladding layer, leading to significant coupling losses.

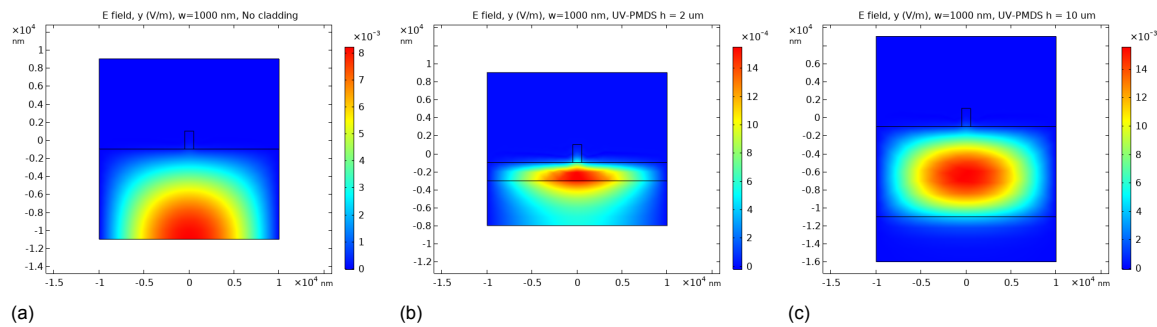(a)   (b)   (c)

Figure 4.5: Simulation results on mode coupling in the cross sectional area of the tapered rib waveguide, solved for the out-of-plane electric field. a) 1 μm UV- PDMS layer with no additional cladding. b) 2 μm UV-PDMS layer with Sylgard PDMS cladding at the bottom. c)10 μm UV-PDMS layer with Sylgard PDMS cladding at the bottom.

The results are also consistent with experimental results that report that TM mode light is inherently lossy within rib waveguides [54]. It is clear that the confinement of light depends crucially on the minimum PDMS layer height that can be achieved in fabrication and should be in the micron range. The mode coupling model has also shown that the modes shift towards the rib region when its width is increased, which is given in Appendix A.7. However this parameter is not changeable due to the set input area of the photonic crystal waveguide. The minimum height of the UV-PDMS cladding is related to fabrication constraints, which are further explained in Section 4.3.1.

4.2.3. Proof of concept using taper waveguides on silicon
The validity, or alignment, of the test setup was confirmed by conducting tests on an established waveguide. The need for a calibration sample arised because of the difficulty of coupling light into the fabricated device due to its small coupling height, ≤ 2 μm, and bottlenecks in the fabrication of the prototype device. Literature ([78]) using photoresist material for the core of the waveguide was taken as a reference for the proof-of-concept design of the tapered waveguide. The sample was printed with 2PP using the 10x objective, which allows large structures to be polymerized. Photoresist IP-Q (Nanoscribe GmbH, n = 1.513) was printed on a silicon (n=3.170) substrate. [1]. The waveguide was designed with an inlet area of 450 μm x 100 μm tapering at an angle of 10°down to an outlet area of 100 μm x 100 μm, which is a scaling up of the model designed in Section 4.2.2. The printed structure is shown in Figure 4.6, along with the views of its inlet and outlet facets.

(a)   (b)   (c)
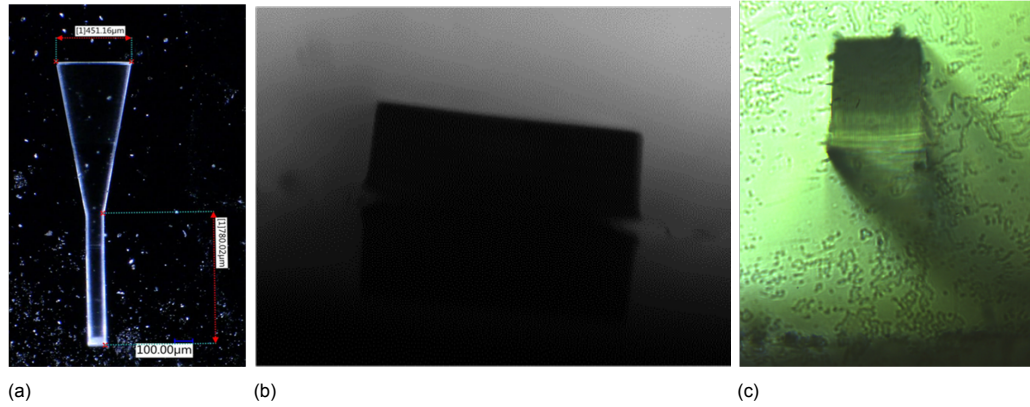
Figure 4.6: Camera images showing the calibration sample, 2PP print of IP-Q on silicon. a) Optical microscope measurements of the taper, the larger width area is the inlet. b) View of the input objective, showing the facet of the taper through which light is coupled. c) View of the output camera, capturing the output facet. Note that the tip of the taper is tilted upwards and detached from the silicon substrate.

The calibration sample was tested with both visible and infrared light following the alignment procedure previously detailed in Section 4.2.1. For both wavelengths, coupling into the waveguide was distinctively observable by looking at the coupled and uncoupled states of light at the output of the waveguide. Uncoupled red light is diffracted across the silicon substrate and the pattern is visible around the taper, seen in Figure 4.7b. When coupled into the taper, the light is clearly confined to the taper area. Light coupled into the waveguide is also visible to the naked eye, shown in Figure 4.7a. Light focused in the waveguide output facet is also pictured for the experiments with infrared light in Figure 4.7c.

(a)   (b)   (c)
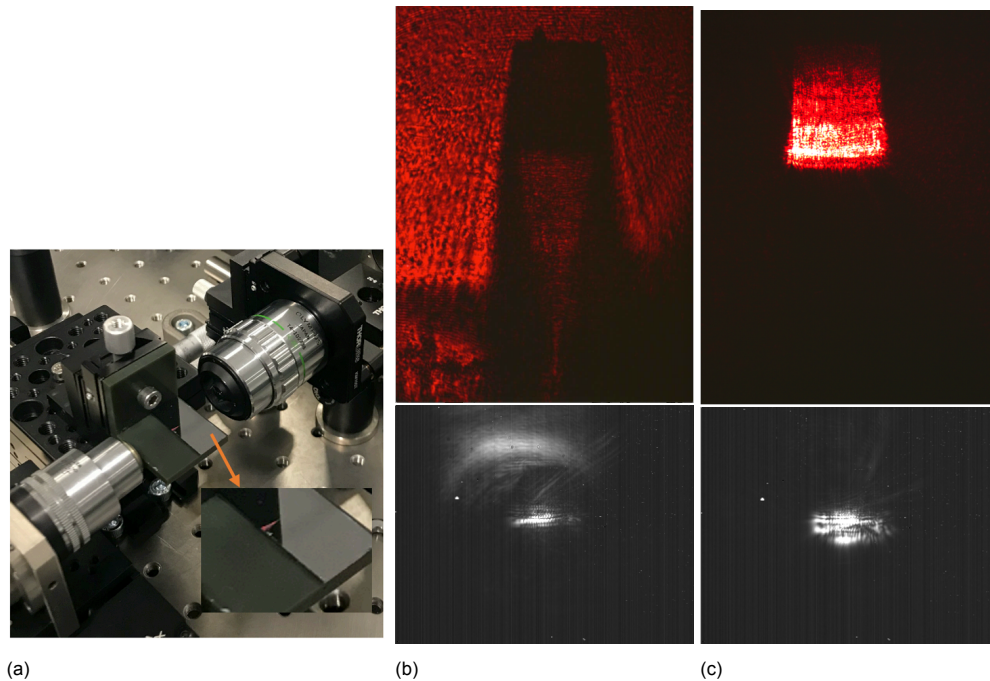
Figure 4.7: Experiments on the test set-up with the calibration taper. a) Image of the test setup during the experiment, inlet shows the red light that is seen coupled into the sample. b) The images of the output facet from the visible and IR- camera showing the uncoupled light exiting the sample. c) The images of the output facet from the visible and IR- camera showing the light coupled into the taper.

4.3. Feedback on the device from the experimental results

The experimental results and observations obtained from the testing phase were used as feedback for the fabrication of the device and the final device design. A sample holder for the PDMS casting was designed as a solution to the fabrication problems that hindered the ability of coupling light into the PDMS facet of the waveguide inlets. The final design for testing was formed with consideration of testing efficiency and the fabrication process.

4.3.1. Design of a sample holder compatible with the test setup

A sample holder was designed to be used during the PDMS molding, to control the dimensions of the of the PDMS slab and to define the PDMS facets that form the interface through which light is coupled into the device. The accessibility with light and the surface quality of the input and output of the fabricated device were the challenges discovered during the experimental phase of the project. It was observed that cutting the PDMS at the edges of the waveguides to make their end facets accessible resulted in cut marks and surface roughness. In addition, light scattering was seen at the inlet during testing, suggesting that the PDMS facet defects result in losses.

The sample holder consists of two components manufactured using a high resolution 3D printer (Micro Plus, Envisiontec GmbH, Germany). The main holder houses the fused silica substrate with the printed 2PP structures. A CAD image can be seen in Figure 4.8a. When the sample is placed inside, a height of 1.5 mm is left at the top and the poured PDMS is leveled to this height, creating a PDMS layer with the same height. The second component of the test setup is designed to address the accessibility and edge quality of the inlet and outlet facets of the waveguide. Two block "holders" are placed on the sample with their edges parallel to the edges of the waveguide. They are used to create a mold for the PDMS slab that ensures that the inlet and outlet facets of the waveguide are in contact with air. The roughness of the PDMS surface is addressed by a silicone wall attached to the side edges of the "block holders", with their smooth side in contact with PDMS. The entire sample holder is shown in Figure 4.8c.

(a)   (b)   (c)
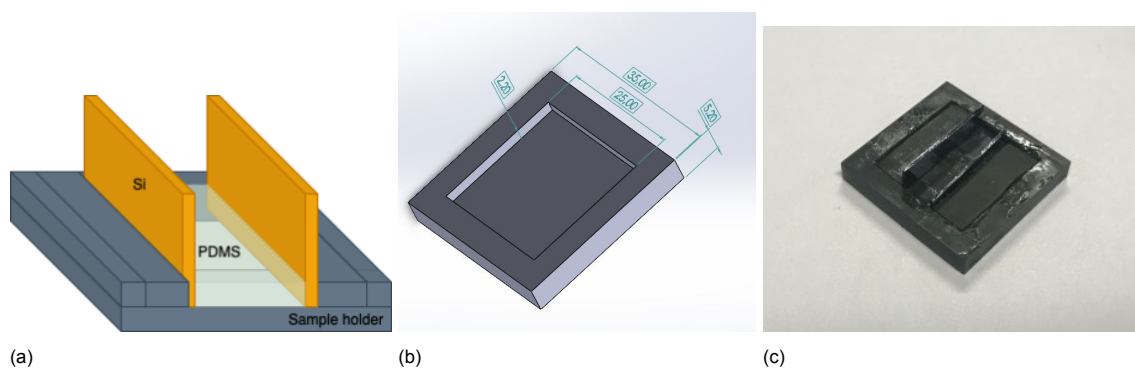
Figure 4.8: a)Illustration of the PDMS sample holder concept. b) CAD design of the sample holder with the dimensions labeled. c) Sample placed inside the sample holder in real life, with the silicon edged holder components placed on top.

4.3.2. Final design of the device

Modelling, fabrication and characterization observations and results led to a final device specifically designed for testing with the built experimental setup. The illustration of the final design and the printed device are shown in Figure 4.9. The main features of the final device design are as follows:

– Multiple waveguide devices are printed on the same chip and the inlet facets are in line.

  Testing multiple waveguides on the same chip is advantageous for several reasons: the 2PP process is sensitive to the state of the laser and environmental conditions, leading to varying results for the prints. Testing waveguides that are printed together leads to experimental results that are comparable. This also eliminates the repetition of the time-consuming procedure that is needed to align a sample in the test setup. With a single chip the objective is focused on the facet

of the device once and then the sample holder only needs to be moved parallel to the facets to move to the next waveguide.

– 3 lengths of photonic crystal waveguides are printed with 3 repetitions of each length.

The test setup measures the intensity of the light at the output of each waveguide. To have a frame of reference for the transmittance of the light, the light intensity is measured for 3 different waveguide lengths (40, 60, and 130 μm). This will allow conclusions to be drawn about the loss of light and the photonic crystal path length. Figure 4.9b shows the 9 waveguides that are printed.

– The photonic crystal waveguide is designed with an s-shaped 45°bent defect.

This creates an offset between the input and output points of the light. The idea is to avoid collecting light that passes straight through. The light must be confined by the photonic crystal waveguide in order to follow a curved path. The S-shaped print was previously shown in Figure 3.2.

– A tapered waveguide is placed at the input of the photonic crystal and a rib waveguide is placed at the exit.

The same coupling waveguide is used for each waveguide to avoid variations in losses due to the coupling. The inlet width is chosen to be 100 μm, as this has been shown to be a dimension that is detectable in the test setup with the calibration sample.

– 2PP blocks are printed at the edges of the inlet and outlet, as air blocks and indicators for the sample holder placement.

The blocks are intended to be used as visual guides to aid in the placement of the silicon edged sample holders onto the printed substrate. Being significantly larger than the waveguide prints, they extend the device edge away from the critical components (waveguides) so that there is an error margin in where the PDMS facet is located. The blocks also function as "air blocks" for PDMS molding, ensuring that the facet of the waveguide is accessible to light by creating an air gap of a few micrometers in the device before the waveguide inlet.
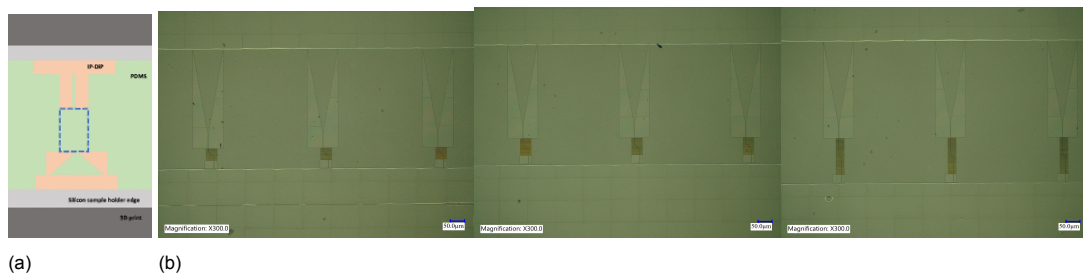

(a)   (b)

Figure 4.9: Visuals of the final design. a) Illustration a single waveguide, showing the pillar region, the coupling blocks, PDMS regions and the air blocks. b) The final device as printed, showing the 9 waveguides and the printed "air" blocks.

4.3.3. Characterization results and limitations

Attempts to couple light into the fabricated photonic crystal device proved challenging and no measurements were able to be made. Limitations in various aspects of the fabrication and light coupling were identified as possible causes and points for further improvement.

Alignment precision was identified as a weakness of the test setup that contributed to the difficulty in experimentation. The functionality of the setup and the taper waveguide coupling system was demonstrated with a proof-of-concept coupler. However, the inlet and outlet area of this calibration sample is x100 times (100 μm vs. 1 μm) the scale of the inlet of the photonic crystal waveguide. This means that the smaller device has less tolerance for misalignment problems such as tilt. Also, the visual feedback from the camera and the light beam is much harder to detect in real life at the submicron scale. The test setup has been proven to be functional, but its alignment accuracy needs to be improved to achieve the precision required for testing the actual photonic crystal waveguide.

The critical limitation in fabrication is the minimum PDMS height that was achieved. Mode analysis showed that the PDMS layer must be in the micrometer range to achieve light coupling in the waveguide, which requires high-precision fabrication. The current PDMS molding method does not allow the height to be controlled at this accuracy. However, the results regarding the possibility of using PDMS with different refractive indices as cladding layers are interesting. The challenge in the design of this waveguide is the inability to use common materials in photonics, such as Si and SiO_2 which have a high refractive index difference and thus better index confinement [16]. However, these materials are not flexible or biocompatible. The use of UV-PDMS and Sylgard 184 PDMS makes it possible to maintain flexibility while ensuring light confinement for both the coupler and the photonic crystal waveguide. It is also promising for the future work on this photonic crystal implant device: It is not applicable to have air as the external environment of the waveguide since the device is to be placed into the brain. Therefore, an additional flexible cladding layer will serve to confine light but can also act as the isolation layer for the implant.

Limitations in the sample holder for PDMS fabrication were also found to be the precision with which the blocks could be placed and leakage into the air gaps between the block and the sample. Attempts were made to prevent leakage into the mold by a variety of methods; double-sided tape to ensure that the blocks are stationary and applying force to the sample holder with magnets and clips to block the air gaps. However, it was found that some degree of leakage was inevitable. The leakage occurs between the PDMS layer and the substrate, leading to defects at the facet where the light is coupled into the device from. Therefore the leakage contributes critically to the loss of transmission efficiency.

5

Conclusion

This thesis was a feasibility study on the use of soft photonic crystal waveguides in a spatio-controlled brain implant for drug delivery. In the bigger picture, the photonic crystal structure is intended to locally activate drug release mechanisms on a flexible implant that will be placed on the surface of the cortex. Critical functionalities and design parameters of the waveguide system were identified to assess feasibility of such an implant. These were biocompatibility, flexibility and transmission efficiency. Design, fabrication and characterization steps were followed to investigate the bandgap behavior and functionality of a 2D photonic crystal waveguide with a flexible matrix, with consideration of its application as a brain implant.

By creating bandgap and transmission analysis models in COMSOL Multiphysics, the photonic crystal waveguide was simulated and designed. The models presented are simulation tools for designing 2D slab photonic crystals with arbitrary bandgap, wavelength, dimension, and materials. The goal of the simulations was to determine the lattice constant, pillar diameter, and material combination that would give the highest transmission efficiency at a wavelength of 1550 nm.

As a result of the dispersion diagram simulations, an unusual design was proposed using metal rings in a flexible matrix as photonic crystals. The structures were shown to be promising as a photonic crystals due to the wide bandgap range they exhibited. Metal thin films showed bandgap behavior similar to bulk metals, creating new opportunities of using thin-film fabrication methods to make the metallo-photonic crystal device. When printed pillars can be coated with a metal ring in a single step, many of the more complicated metal fabrication methods, patterning PDMS, metal plating etc., are eliminated.

Modelling has demonstrated that it is possible to use a 2D photonic crystal in a brain implant that is expected to withstand mechanical bending. One of the important aspects of achieving this is identified as selecting a design with a wide bandgap to compensate for the transmission shifts that occur due to bending. A model for a lattice constant of 800 nm and 560 nm diameter pillars was calculated to have a transmission of 78% in a linear waveguide of 15 unit cells and a wide bandgap between 1400 nm and 1700 nm. The model consists of a flexible photosensitive PDMS (UV-PDMS) matrix with 21 nm gold thin film coated photoresist nanopillars embedded in it. The mechanical bending of the implant in the brain was estimated using a 2D approach to relate this to a strain that deforms the unit cell of the photonic crystal. When this waveguide experiences a nominal bending radius of 2.671 μm, the transmission at the top and bottom surfaces of the implant changes by $\pm$ 3%. The simulated strain is significantly greater than that experienced by the implant due to the curvature of the brain ($\approx$ 15 mm). It can be concluded that the waveguide should maintain high transmission efficiency when placed on the brain.

Experiments with two-photon polymerization (2PP) provided a printing strategy for controlling the pillar diameters: incremental changes in dose can tune the pillar dimensions with high precision without having to change the model itself. This is very valuable for the fabrication of photonic crystals, since pillar diameter to pitch distance (r/a) is a sensitive parameter that strongly influences the performance of the waveguide.

Printing with negative tone resist IP-Dip, a minimum pillar diameter of 0.30 $\pm$0.02 μm was achieved with a lattice constant of 0.5 μm. The measured aspect ratio was 3.9. Uniform and defect-free nanopillar arrays with a size of 30 μm by 120 μm were printable.

Fabrication of the flexible matrix resulted in a protocol for the transfer of submicron pillars into a UV-PDMS slab. The ability to have high refractive index materials embedded inside the matrix without disrupting the flexibility of the device makes this fabrication method is very useful for the design of such a brain implant. UV-PDMS proved to be more favorable for patterning nanostructures compared to Sylgard 184 due to its lower viscosity.

The photonic behavior of the waveguide, both as printed and after PDMS coating, was observed optically. The color of the nanopillar arrays under white light changed with varying periodicity and pillar diameter. This was a visual confirmation of the effect of the design parameters on the photonic bandgap, as well as an efficient detection tool to confirm the pillar sizes and uniformity of all printed samples.

The experimental setup was constructed as an end-fire coupled free-space light path to measure the transmission of visible and infrared light through the photonic crystal waveguide. The functionality of the experimental setup was demonstrated for a calibration sample with an output area of 100 μm by 100 μm. Light was delivered into the input facet and collected out of the output facet of the prototype device in the light propagation plane. Alignment was ensured using cameras.

In the thesis, a fabrication strategy was presented in which the entire waveguide device, the photonic crystal and its coupler, are printed and molded on the same chip. This allowed for efficient and simple fabrication of the device. The use of 2PP for printing resulted in very good alignment for light coupling between the taper and the photonic crystal waveguides. The print of the coupling structure was designed to serve as a mold and the UV-PDMS was patterned in the same fabrication step as the pillars of the photonic crystal. The coupling was designed as a tapered rib waveguide made of PDMS.

3D light confinement in the waveguide design was proposed to be provided by an additional flexible cladding layer by modelling the light mode at the cross section of the rib waveguide. The UV-PDMS rib waveguide (n = 1.3996) was designed to be index confined by adding a lower refractive index PDMS layer (Sylgard, n = 3804) to the bottom of the device. This way, the flexibility of the structure is not compromised and losses in the direction perpendicular to the light propagation plane are mitigated. The simulations showed that the UV-PDMS layer must be fabricated as thin as possible, otherwise much of the light is lost to the cladding layer and light coupling is inefficient.

The conclusions from the experimental phase of light coupling created a feedback loop for the design and fabrication process. The critical fabrication step, expected to be the source of losses in the device, was identified as the PDMS drop casting. The quality of the facets of the waveguide through which light is coupled into the device in the test setup and the thickness of the PDMS layer were two of the bottlenecks encountered. A sample holder with mirrored silicon sidewalls was designed for PDMS molding to fabricate a smoother surface for the waveguide inlet. With this sample holder, a minimum UV-PDMS layer of 1 mm was achieved.

Overall, the findings of this thesis is a promising step towards actualising the drug-delivery brain implant that is functionalized with a photonic crystal waveguide. The recommendations that are proposed to further the research of this device is provided in Chapter 6. This proposed design of a photonic crystal waveguide, and the delivery of light in the implant, is a fraction of the research that needs to be completed before such an implant can be realised as a treatment method of brain disorders.

6

Recommendations

The results of this thesis, both positive and negative, have led to a guide for the next steps in continuing this line of research on the use of photonic crystals as a light delivery system in a brain implant. This section offers the new questions that arise from this work and the recommendations for the direction with which to continue this research.

The metallo-photonic crystal structures exhibited high transmission of 1550 nm light in structures with larger feature sizes than those of dielectric models. It will be interesting to exploit this property to achieve bandgap wavelengths that are difficult to reach with the dielectric models due to fabrication limitations. For a unit cell with a lattice constant of 500 nm, one of the bandgaps of the 2D photonic crystal was shown to be in the visible light region. This can be used to design a waveguide that functions with red light. To do so, modelling calculations need to be repeated with the optical properties adjusted to the appropriate frequency. It is also recommended to investigate surface plasmon effects, where surface waves can localize at the metal/dielectric interface at visible/ IR frequencies and could be valuable to further understand the metal bandgap behavior [42, 33]. Jiang et al. suggest that using the Finite-Difference Time-Domain method (FDTD) to analyze a 2D metallic photonic crystal in 3D leads to a more accurate model to explain the absorption that occurs due to metal dispersion [25]. This approach can be used to obtain a more in-depth analysis of the waveguide designed in this thesis.

An improvement in fabrication will be to measure the gold layer deposited on the pillars and confirm that the sidewalls are indeed uniformly coated. The current sputter coater used for the experiments is efficient but not accurate. The fabrication of the gold layer can be improved, and gold can be replaced with other "good" metals such as silver if the fabrication allows. Since modelling has shown that the ring and bulk metals exhibit similar behavior, the model can be simulated again to design for gold pillars. Gold pillars can be fabricated by electroplating [41], but their transfer into the PDMS matrix needs to be investigated. The validity of the photonic crystal design relies on the assumption that no delamination occurs between the contact surface of PDMS and the nanopillars when the device is mechanically bent. Scanning electron microscopy can be used to image the bent state to confirm that the PDMS remains attached to the pillars.

Diverging from the current design, the implant can be designed as a more complicated geometry, such as a woodpile. Nanoscribe offers a negative PDMS resist (IP-PDMS) that can be used to fabricate 2PP flexible 3D structures. This can eliminate the need for a PDMS matrix and thus a molding step, as well as the problems associated with index confinement, since the structure will confine light in all 3 dimensions.

The coupling of light into the system can be improved. The characterization of the photonic crystal device depends largely on how the light is delivered. The alignment of the test setup can be improved by adding tilt adjusting components that compensate for the minimal misalignment in the light path as it travels through each component. The objectives used in the setup were selected based on their availability and are designed for visible light. The use of lenses specifically designed for IR will minimize the losses and can allows for a smaller spot size.

Although the end-fire coupling system is simplistic and easy to use, another method can be used to eliminate the problems encountered. One possible choice is to use a grating coupler system where the light is delivered into the system vertically [11]. This method can be incorporated into the same printing and PDMS molding steps used to fabricate the current taper coupler. Since light is not delivered from a side facet of the PDMS slab, the need for improvement of the side edges and additional sample holder components can be eliminated. However, the grating coupler requires careful design to achieve high transmission efficiency.

Control of the PDMS slab height can be improved by designing a more accurate sample holder. The use of spin coating to achieve a thin PDMS layer is not recommended as initial experiments during the project showed incompatibility with the flow around the nanopillar arrays of the waveguide. A more inventive solution can be using the aforementioned PDMS resist to to two-photon polymerize the cladding layer with high accuracy.

Full characterization of this flexible photonic crystal waveguide design still remains. The transmission should be measured for a range of wavelengths to obtain a spectrum that confirms where the bandgap occurs. Transmission through the device also needs to be tested in mechanical bending to verify the modeling results and confirm that the designed implant can indeed remain functional and transmit light despite the deformation caused by the movement and curvature of the brain.

A
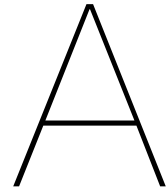
Modelling

A.1. Au thin film refractive index and extinction coefficients

Optical constants of the gold thin film are dependent on the film thickness and frequency. Table A.1 gives the constants that were used in the simulation of the models with the gold.

Table A.1: Refractive index, n, and extinction coefficient, k, for varying gold thin film thickness.

Gold ring thickness	n:	k:
5.7 nm [17]	1.0453	10.840
11.7 nm [17]	0.84991	10.925
21 nm [61]	0.35755	10.669
Bulk [27]	0.52406	10.742

A.2. COMSOL transmission data

The data acquired from the COMSOL transmission simulations are reported for several material combinations in this section. Calculated transmission percentages through the waveguide model at 1550 nm wavelength are listed for a sweep of the lattice constant (labeled a) and radius to lattice constant ratio r/a. These results were used to choose the "key" models, which are detailed in shown Table 2.1.

GaN pillars in UV-PDMS matrix (Model A)

```
% Model:              waveguide-gan.mph
% Version:            COMSOL 5.4.0.388
% Date:               Jul 23 2021, 22:41
% Table:              Table 6 - Global Evaluation 1 (Pout/Pin)
% a (nm)              r/a                      Pout/Pin*100 (1)
500                   0.2                      2.1569386467987946
500                   0.25                     21.307853848456865
500                   0.30000000000000004      33.141063555395384
500                   0.35000000000000003      29.703064712518934
500                   0.4                      0.7820139295152517
600                   0.2                      46.9784190379287E-3
600                   0.25                     1.3614756559235138
600                   0.30000000000000004      2.7368337481407004
600                   0.35000000000000003      30.955069753483297E-3
600                   0.4                      91.90813355846824E-4
```

21 nm Au ring around IP-Dip pillars in UV-PDMS (Model D)

```
% Model:              waveguide-gold.mph
% Version:            COMSOL 5.4.0.388
% Date:               Jul 24 2021, 16:44
% Table:              Table 2 -
% a (nm)              ra                       Pout/Pin*100 (1)
500                   0.2                      62.15456623420781
500                   0.25                     59.30295156424391
500                   0.30000000000000004      62.37401107941044
500                   0.35000000000000003      61.10308619793307
600                   0.2                      50.48880598149018
600                   0.25                     65.09957016946977
600                   0.30000000000000004      64.3886899281784
600                   0.35000000000000003      67.98592045159731
700                   0.2                      41.317798594721324
700                   0.25                     72.6883846151264
700                   0.30000000000000004      74.71741670834693
700                   0.35000000000000003      73.34976596479166
800.0000000000001     0.2                      72.65843156936755
800.0000000000001     0.25                     38.46476196307269
800.0000000000001     0.30000000000000004      76.96903155798528
800.0000000000001     0.35000000000000003      78.46420539460681
900                   0.2                      0.4946005853380987
900                   0.25                     63.75630776138554
900                   0.30000000000000004      76.93958135465286
900                   0.35000000000000003      79.70583319275971
1000                  0.2                      76.33090681846869
1000                  0.25                     70.6216774658272
1000                  0.30000000000000004      0.002622524641464183
1000                  0.35000000000000003      65.84374766439473
1100                  0.2                      67.47979450380524
1100                  0.25                     81.08164079022681
```

1100	0.30000000000000004	77.978798721934
1100	0.35000000000000003	1.0070201839182525E-4
1200	0.2	69.27941802995488
1200	0.25	61.57593088192506
1200	0.30000000000000004	63.58962185207585
1200	0.35000000000000003	78.19698970553269
1300	0.2	65.84054429854024
1300	0.25	68.36233215569722
1300	0.30000000000000004	59.66312523301108
1300	0.35000000000000003	85.94574807220371
1400	0.2	41.034443631701194
1400	0.25	41.76071617829259
1400	0.30000000000000004	63.745964669751935
1400	0.35000000000000003	85.56407737237228

11.7 nm Au ring around IP-Dip pillars in UV-PDMS (Model E)

```
% Model:              waveguide-gold-11.7nm.mph
% Version:            COMSOL 5.4.0.388
% Date:               Jul 25 2021, 00:31
% Table:              Table 8 - Global Evaluation 1 (Pout/Pin*100)
% a (nm)              ra                        Pout/Pin*100 (1)
```

a (nm)	ra	Pout/Pin*100 (1)
500	0.2	44.70718511272956
500	0.25	43.201607133578015
500	0.30000000000000004	39.431623998006295
500	0.35000000000000003	33.01268514796826
600	0.2	20.469690072393785
600	0.25	47.46884983627258
600	0.30000000000000004	46.472981794122475
600	0.35000000000000003	46.05081110255225
700	0.2	19.562931467851868
700	0.25	48.23005418561989
700	0.30000000000000004	58.34564595580852
700	0.35000000000000003	53.36943587877548
800.0000000000001	0.2	57.22181660462364
800.0000000000001	0.25	60.02893079969034
800.0000000000001	0.30000000000000004	50.88532195819548
800.0000000000001	0.35000000000000003	62.462716505005254
900	0.2	33.97522610204796
900	0.25	0.15695488517056033
900	0.30000000000000004	57.681510405213196
900	0.35000000000000003	61.646650597532535
1000	0.2	66.79459545107385
1000	0.25	59.35925343630313
1000	0.30000000000000004	19.722406772947934
1000	0.35000000000000003	32.52469336050896
1100	0.2	50.86001132965091
1100	0.25	70.39711825508682
1100	0.30000000000000004	57.00511128952252
1100	0.35000000000000003	11.430217932139229
1200	0.2	64.67133959777027
1200	0.25	42.72533967253693
1200	0.30000000000000004	72.00594721289264
1200	0.35000000000000003	69.3045060136286
1300	0.2	53.506256171215966
1300	0.25	58.793468800244874
1300	0.30000000000000004	49.82114153959723

```
1300                    0.35000000000000003        76.57773828984047
1400                    0.2                        41.18843279946578
1400                    0.25                       51.33554043769404
1400                    0.30000000000000004        67.84682431891143
```

A.3. Dispersion diagram and transmission spectra of key models

The following graphs give the bandgap and transmission calculations performed on the key models of the project. This data was summarised in Table 2.1.

GaN pillars in UV-PDMS matrix (Model A)

(a)   (b)
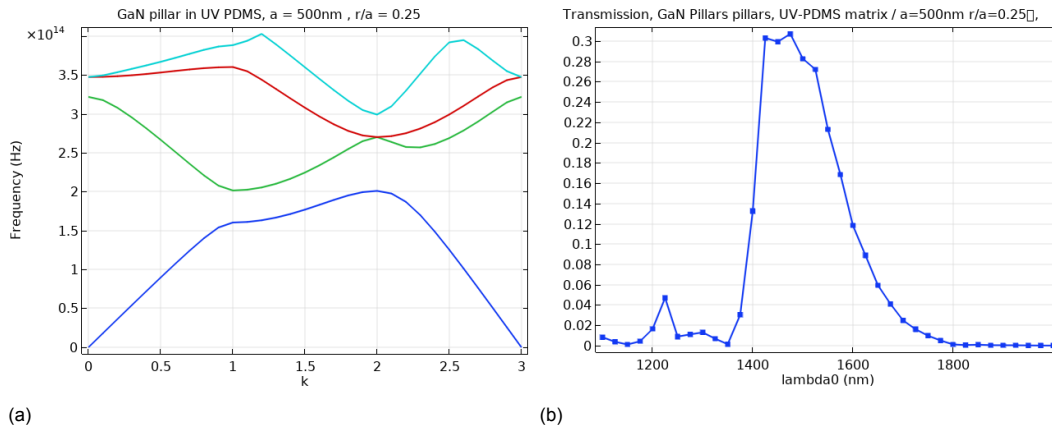
Figure A.1: Bandgap diagram and transmission of model D1, 21nm GaN in UV-PDMS matrix with a=500 nm, r/a=0.25.
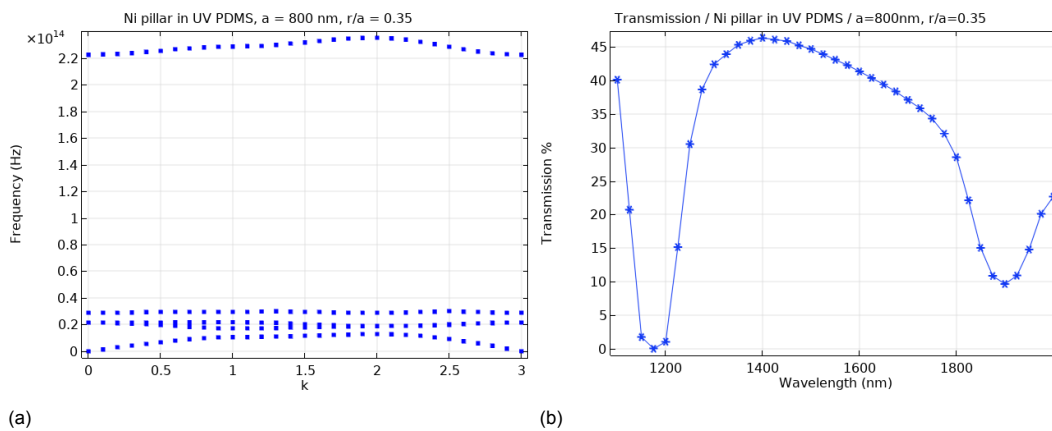
Nickel pillars in UV-PDMS (Model B)

(a)   (b)
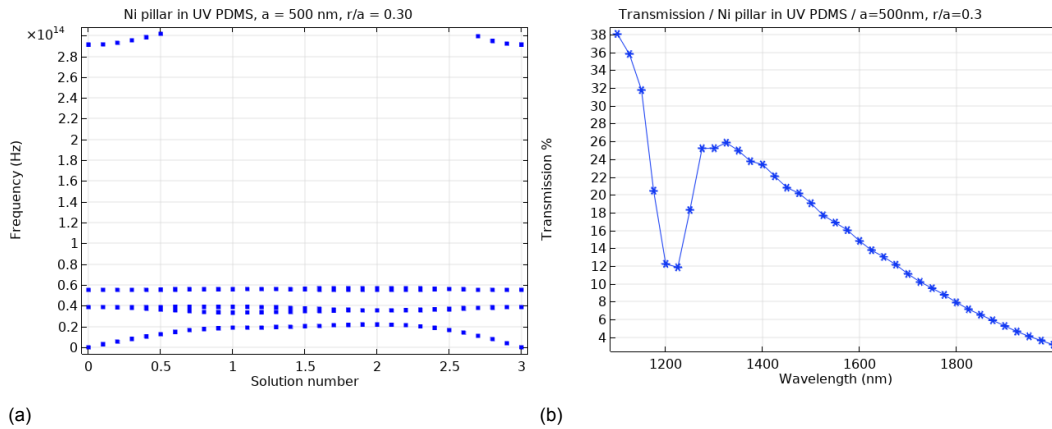
Figure A.2: Bandgap diagram and transmission of model B1, Nickel pillars in UV-PDMS matrix with a = 500 nm, r/a=0.3.

(a)   (b)

Figure A.3: Bandgap diagram and transmission of model B2, Nickel pillars in UV-PDMS matrix with a = 800 nm, r/a=0.35.

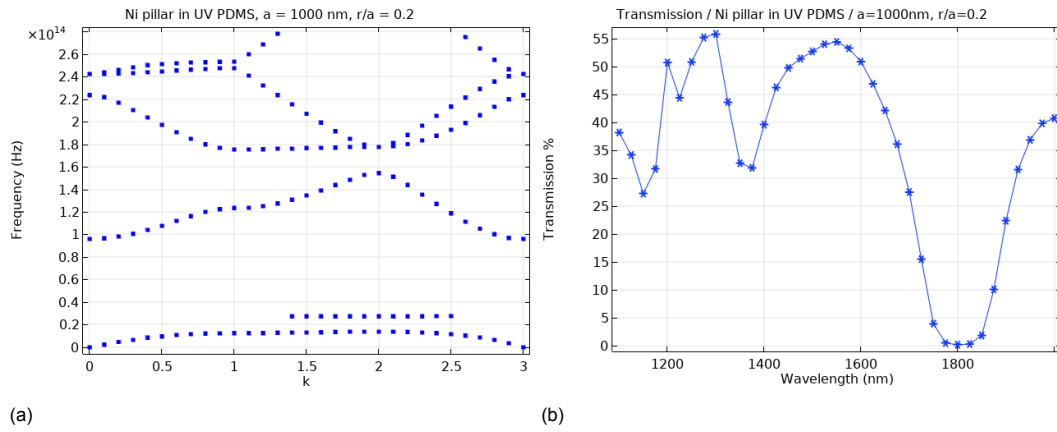(a)   (b)

Figure A.4: Bandgap diagram and transmission of model B3, Nickel pillars in UV-PDMS matrix with a = 1000 nm, r/a=0.2.

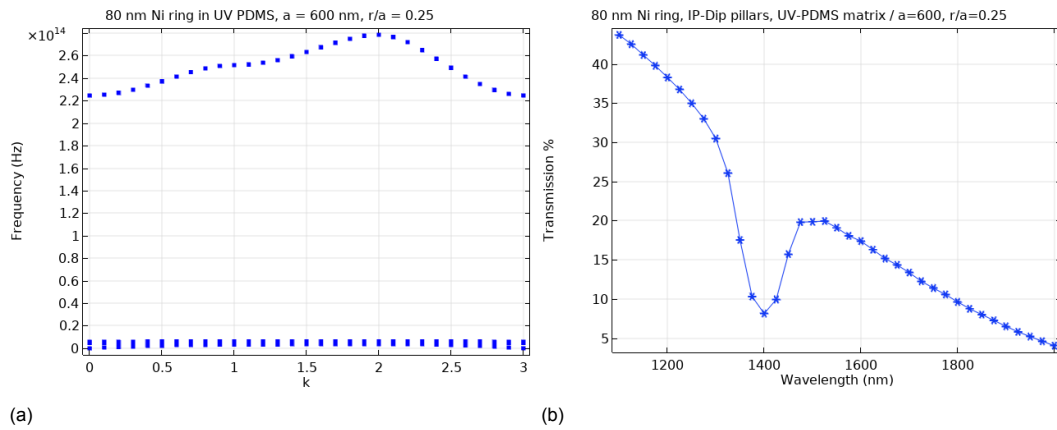## 80 nm Ni ring around IP-Dip pillars in UV-PDMS (Model C)

(a)   (b)

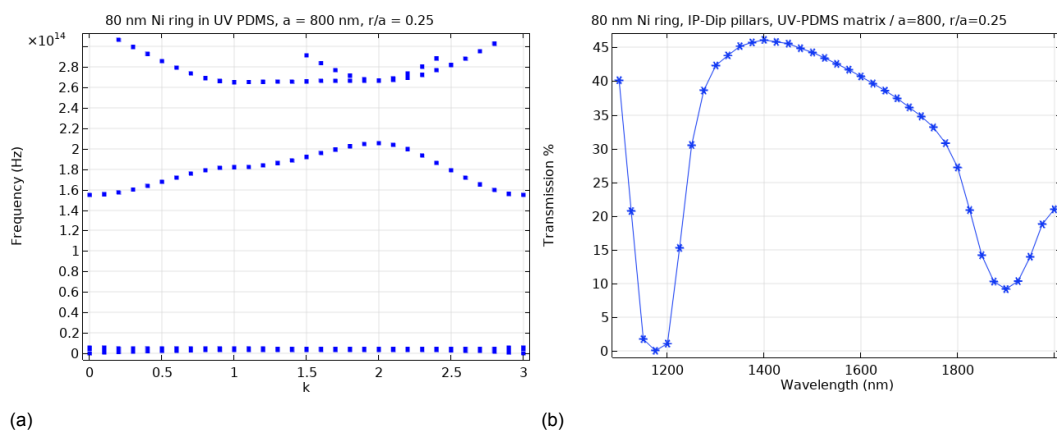Figure A.5: Bandgap diagram and transmission of model C1, IP-Dip pillars with 80 nm Ni Ring in UV-PDMS matrix with a=600 nm, r/a=0.25.

(a)   (b)

Figure A.6: Bandgap diagram and transmission of model C2, IP-Dip pillars with 80 nm Ni Ring in UV-PDMS matrix with a=800 nm, r/a=0.25.
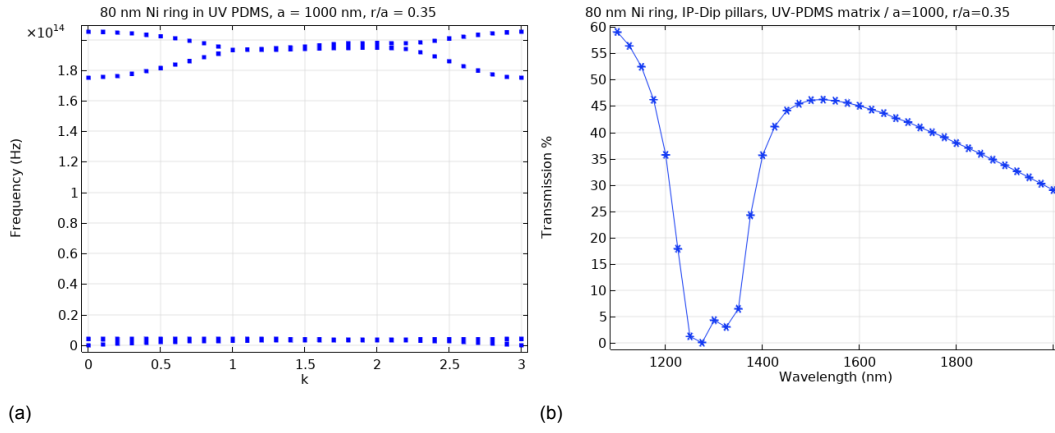
Figure A.7: Bandgap diagram and transmission of model C2, IP-Dip pillars with 80 nm Ni Ring in UV-PDMS matrix with a=1000 nm, r/a=0.35.

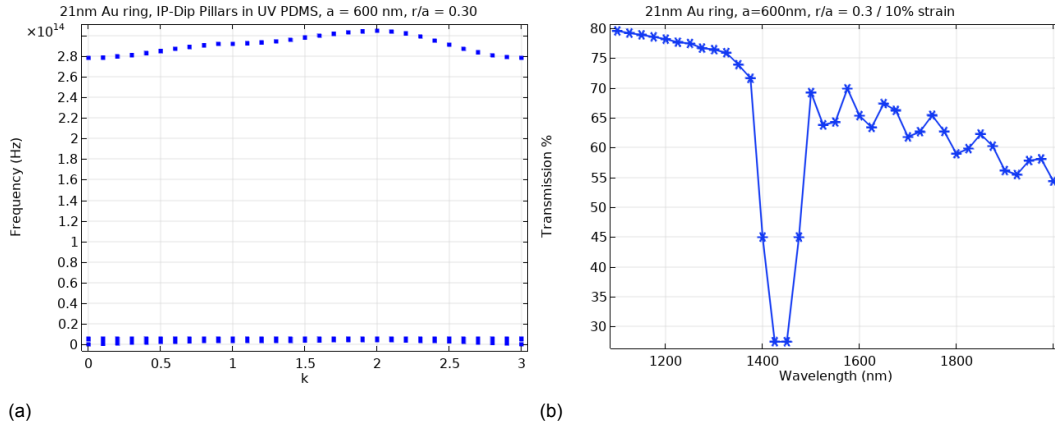## 21 nm Au ring around IP-Dip pillars in UV-PDMS (Model D)

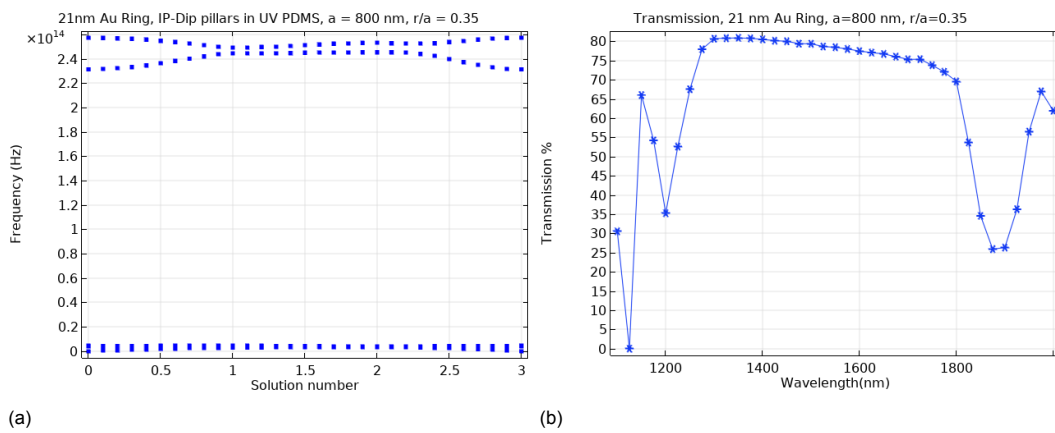Figure A.8: Bandgap diagram and transmission of model D1, 21nm Au ring, 600 nm, r/a = 0.3.

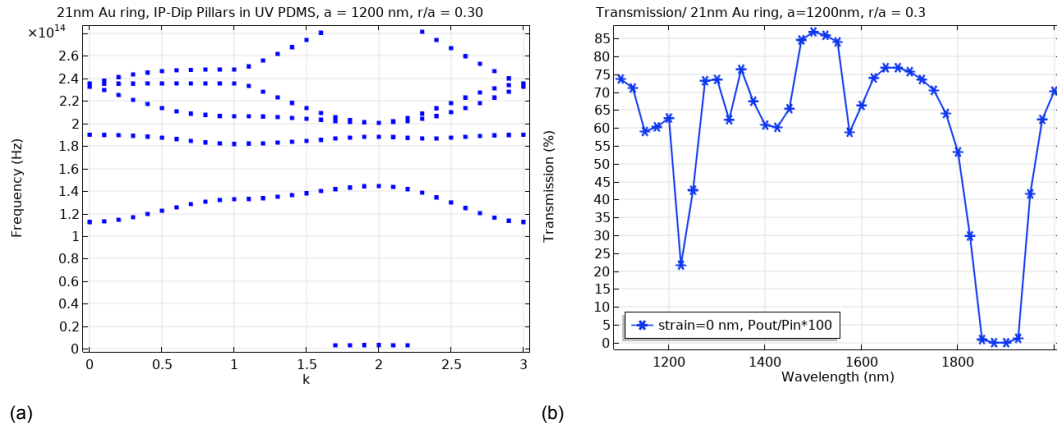Figure A.9: Bandgap diagram and transmission of model D2, 21nm Au ring, 800 nm, r/a = 0.35.

(a)   (b)

Figure A.10: Bandgap diagram and transmission of model D3, 21nm Au ring, 1200 nm, r/a = 0.3.

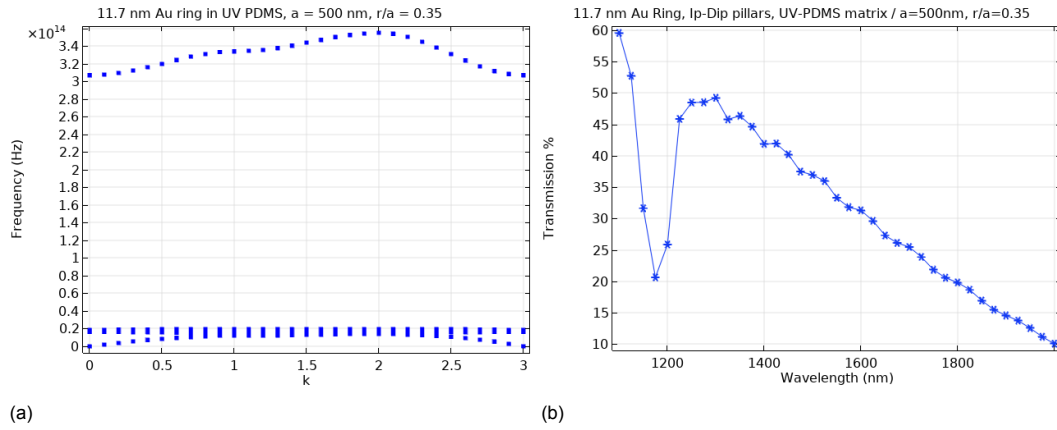## 11.7 nm Au ring around IP-Dip pillars in UV-PDMS (Model E)

(a)   (b)

Figure A.11: Bandgap diagram and transmission of model E1, IP-Dip pillars with 11.7nm Au ring in UV-PDMS, a=500 nm, r/a = 0.35.

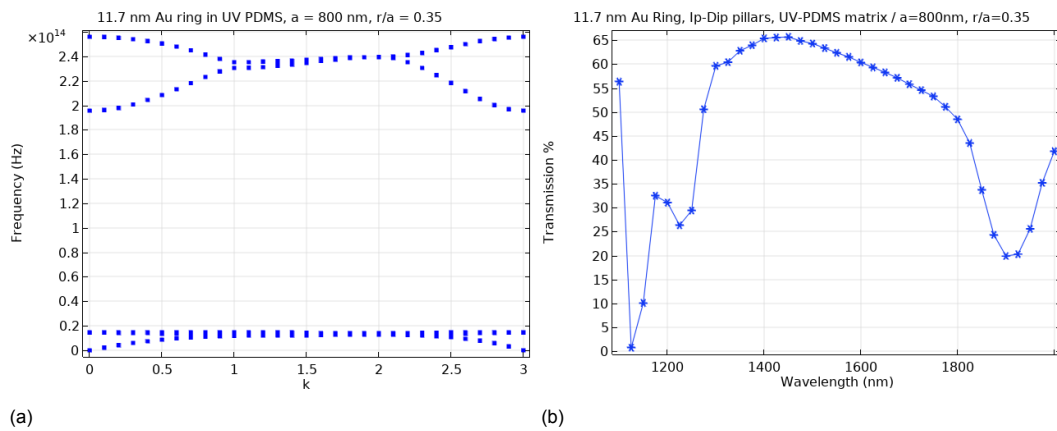(a)   (b)

Figure A.12: Bandgap diagram and transmission of model E2, IP-Dip pillars with 11.7nm Au ring in UV-PDMS, a=800 nm, r/a = 0.35.
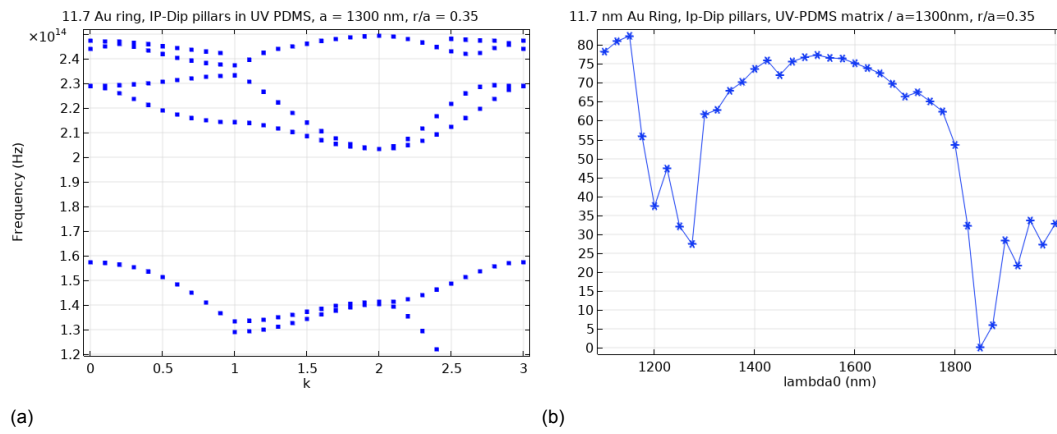
Figure A.13: Bandgap diagram and transmission of model E2, IP-Dip pillars with 11.7nm Au ring in UV-PDMS, a=1300 nm, r/a = 0.35.

A.4. COMSOL transmission calculations for mechanical bending

The COMSOL results that were used to report the effect of strain on the photonic crystal waveguide transmission (Section 2.3.2) are given in this section. The deformation of the unit cell is set as $(a \pm \Delta a)$. $l + 15a$ is the expression used for the length of the waveguide in its deformed state. Δa is calculated by for the strain applied by using the bending radius calculations that were given in Section 2.3.

Key Model D1 – 600 nm, r/a = 0.3, evaluated at 10% strain

```
% Model:              waveguide-20nm-500-03-10%.mph
% Version:            COMSOL 5.4.0.388
% Date:               Aug 31 2021, 11:45
% Table:              Table 9 - Global Evaluation 1 (, Pout/Pin*100, l+15*a, )
% strain (nm)         lambda0 (nm)          Pout/Pin*100 (1)         l+15*a (nm)
60                    1549.9999999999998       8.859768179686938         9900
0                     1549.9999999999998      64.28516370694295          9000
-60                1549.9999999999998      72.3161107553325        8100.000000000001
```

Key Model D1 – 600 nm, r/a = 0.3, evaluated at 20% strain

```
% Model:              waveguide-20nm-500-03-10%.mph
% Version:            COMSOL 5.4.0.388
% Date:               Aug 31 2021, 12:24
% Table:              Table 10 - Global Evaluation 1 (, Pout/Pin*100, l+15*a, )
% strain (nm)         lambda0 (nm)          Pout/Pin*100 (1)         l+15*a (nm)
120                   1549.9999999999998      58.987132448168694        10800
0                     1549.9999999999998      64.28516370694291          9000
-120               1549.9999999999998      73.46952917461081       7200.000000000001
```

Key Model D2 – 800 nm, r/a = 0.35, evaluated at 10% strain

```
% Model:              waveguide-20nm-800-035-10%.mph
% Version:            COMSOL 5.4.0.388
% Date:               Jul 26 2021, 23:28
% Table:              Table 9 - Global Evaluation 1 (, Pout/Pin*100, l+15*a, )
% deltaa (nm)         Pout/Pin*100 (1)          L (nm)
-80                   80.5161910824916          10799.999999999998
0                     78.48557380193593         11999.999999999998
80                    75.41639041955544         13200
```

Key Model D2 – 800 nm, r/a = 0.35, evaluated at 20% strain

```
% Model:              waveguide-20nm-800-035-20%.mph
% Version:            COMSOL 5.4.0.388
% Date:               Jul 26 2021, 23:34
% Table:              Table 9 - Global Evaluation 1 (, Pout/Pin*100, l+15*a, )
% deltaa (nm)         Pout/Pin*100 (1)          L (nm)
-160                  75.86507642194394         9599.999999999998
0                     78.48557380193593         11999.999999999998
160                   22.29231145024592         14400
```

Key Model D3 – 1200 nm, r/a = 0.35, evaluated at 10% strain

```
% Model:              waveguide-20nm-10%-1000-025.mph
% Version:            COMSOL 5.4.0.388
% Date:               Aug 31 2021, 19:46
% Table:              Table 9 - Global Evaluation 1 (, Pout/Pin*100, l+15*a, )
% strain (nm)         lambda0 (nm)          Pout/Pin*100 (1)         l+15*a (nm)
-120               1549.9999999999998      82.82121933921424      16200.000000000002
0                     1549.9999999999998      78.15754933730526         18000
120                   1549.9999999999998      81.11717582558245         19800
```

Key Model D3 – 1200 nm, r/a = 0.35, evaluated at 20% strain
```
% Model:              waveguide-20nm-500-03-10%.mph
% Version:            COMSOL 5.4.0.388
% Date:               Aug 31 2021, 14:24
% Table:              Table 11 - Global Evaluation 1 (, Pout/Pin*100, l+15*a, )
% strain (nm)         lambda0 (nm)          Pout/Pin*100 (1)       l+15*a (nm)
240                   1549.9999999999998    72.45272521841893      21600
0                     1549.9999999999998    84.04616364566884      18000
-240                  1549.9999999999998    80.44942627344939      14400.000000000002
```

Key Model D3 – 1200 nm, r/a = 0.35, evaluated at 20% strain
```
% Model:              waveguide-20nm-500-03-10%.mph
% Version:            COMSOL 5.4.0.388
% Date:               Aug 31 2021, 14:24
% Table:              Table 11 - Global Evaluation 1 (, Pout/Pin*100, l+15*a, )
```

A.5. Transmission graphs for key model D

The following graphs are the transmission spectra calculated for key model D, the 21 nm Au ring model. The design parameters lattice constant (a,ranging 500 nm to 1000 nm) and pillar diameter to lattice constant (r/a, ranging 0.2 to 0.35) are the varied. These graphs are valuable to validate the expected transmission values of the fabricated models because their r/a constants are subject to an error margin.
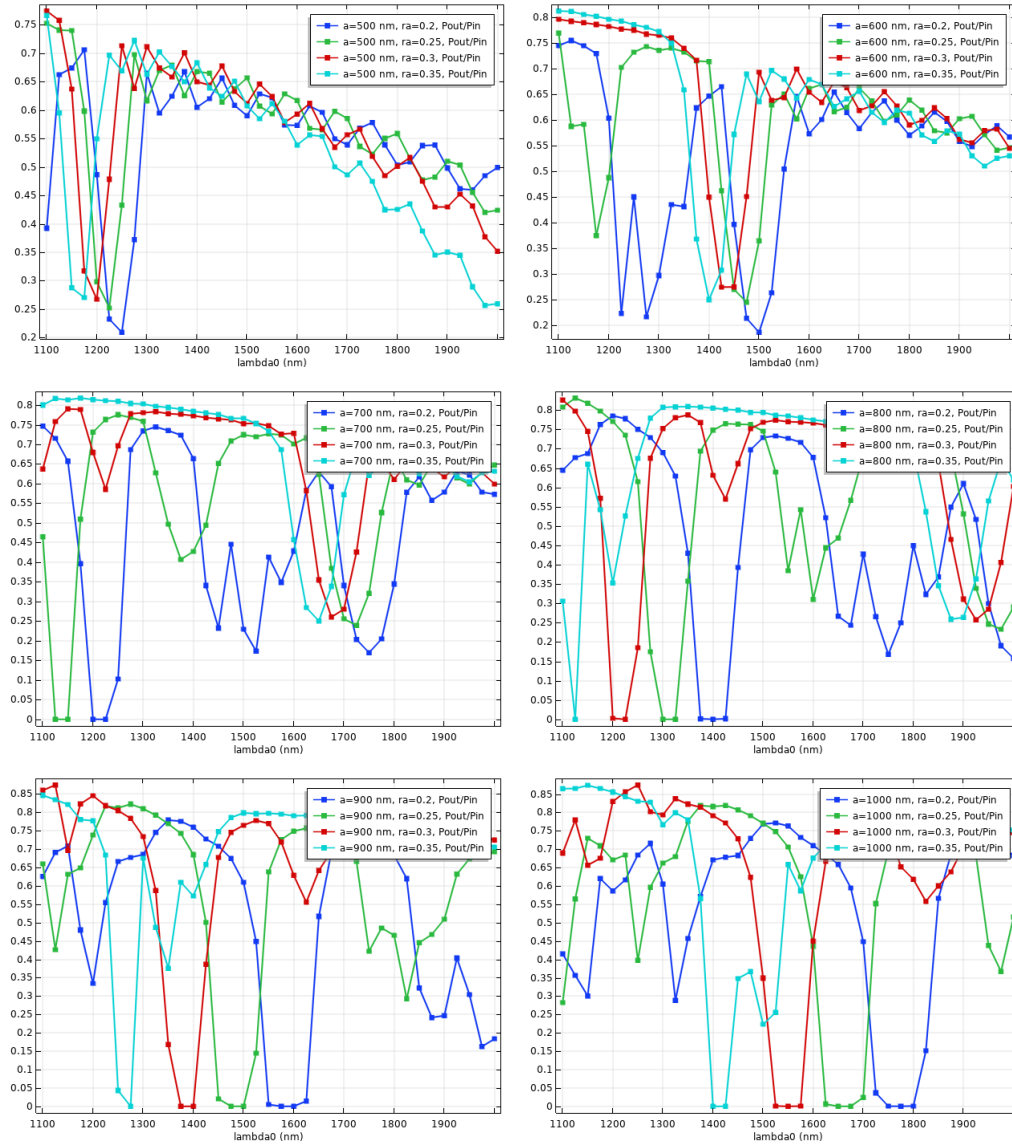

Figure A.14: Transmission spectra plotted for key model **A**. Pillar diameter to lattice constant r/a is varied from 0.2 to 0.35 for lattice constants (a), ranging 500 nm to 1000 nm.

A.6. COMSOL transmission values for the tapered waveguide with varying taper angle

COMSOL transmission calculations on the tapered waveguide (Section 4.2.2) are performed to determine the taper angle at which the optimum light propagation is achieved. To do so the output width (w_a) is kept constant while a parameter sweep is done for the length of the taper (l_taper). The input width is kept constant at 10 μm. The angle is swept from 25°(l_taper = 10 μm) to 2°(l_taper = 150 μm).

```
% Model:              tapered+simulation.mph
% Version:            COMSOL 5.4.0.388
% Date:               Jul 23 2021, 23:29
% Table:              Table 10 - Global Evaluation 1 (, , -Pout/Pin*100)
% l_taper (um)        lambda0 (nm)       w_a (m)           -Pout/Pin*100 (1)
10                  1550                1.12E-6           17.88634791025736
29.999999999999996    1550              1.12E-6            65.28849743235192
49.99999999999999     1550              1.12E-6            68.87081941249502
70                  1550                1.12E-6           73.7806403469555
89.99999999999999     1550              1.12E-6            75.51680009283893
109.99999999999999    1550              1.12E-6            72.5485926597028
130                 1550                1.12E-6           74.3157532931681
150                 1550                1.12E-6           74.58489671573936

% Model:              tapered+simulation.mph
% Version:            COMSOL 5.4.0.388
% Date:               Jul 23 2021, 23:39
% Table:              Table 11 - Global Evaluation 1 (, w_a, -Pout/Pin*100)
% l_taper (um)        lambda0 (nm)       w_a (m)           -Pout/Pin*100 (1)
10                  1550                7.000000000000001E-7   16.39671146486068
29.999999999999996    1550              7.000000000000001E-7   54.63801060924996
49.99999999999999     1550              7.000000000000001E-7   58.2521594743451
70                  1550                7.000000000000001E-7   65.20367966694238
89.99999999999999     1550              7.000000000000001E-7   62.18502642211055
109.99999999999999    1550              7.000000000000001E-7   65.002864464325
130                 1550                7.000000000000001E-7   63.26268387397078
150                 1550                7.000000000000001E-7   65.10883211163258
```

A.7. COMSOL mode simulations for rib waveguide

Light coupling into the rib waveguide is simulated with a mode study in COMSOL. The model of a UV-PDMS rib waveguide with low refractive index PMDS cladding as the bottom layer is used. Figure A.15 shows an example of the effect of the width of the rib on the coupling. The mode for rib widths 1 μm, 3 μm and 5 μm are pictured. It is seen that the wider rib allows more light to be coupled into the waveguide.
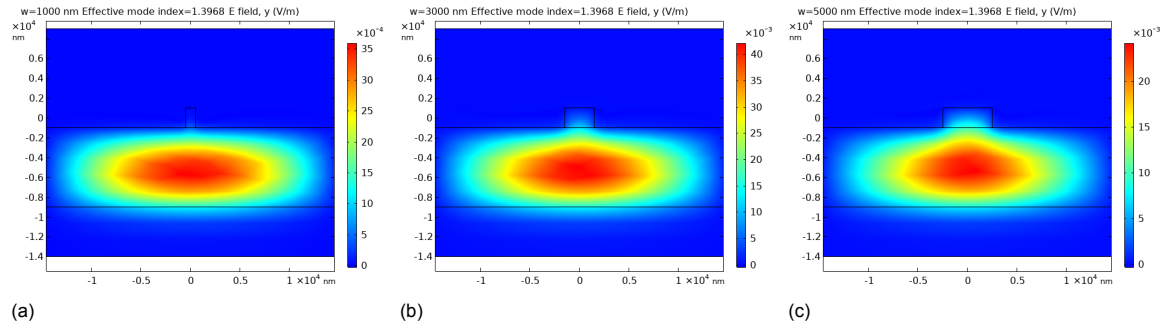

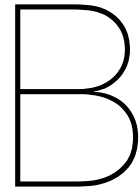(a)   (b)   (c)

Figure A.15: Mode study on the cross section of the rib waveguide showing the effect of the rib width to coupling of light. The UV-PDMS layer is 8 μm and the rib height is kept constant at 2 μm. a) Rib width 1 μm. b) 3 μm. c) 5 μm.

B

Fabrication

B.1. Device fabrication protocol

2D printing:

1. A cleanroom soft cloth is used to clean the fused silica sample first with Acetone, then isopropanol (IPA). The sample is dried using the air blower.

2. The fused silica sample is cleaned in the plasma cleaner for 10 minutes.

3. The sample is then placed in of the slots on the sample holder of the Nanoscribe and it is secured by placing tape on its edges.

4. A droplet of IP-Dip, a negative-tone photo resist formulated by Nanoscribe, is dispensed on the sample.

5. The sample holder is loaded into the Nanoscribe device, and the related .gwl file is printed. The advised printing steps of the Nanoscribe are followed.

6. Once printed the substrate is removed from the sample holder and placed in PGMEA for 40 minutes and then 10 minutes in IPA. It is finally placed in 3M™ Novec™ Engineering Fluid for 30 seconds. In all these steps, the sample should be placed in the fluids vertically. The removal from one fluid to the placement to the next one should be done as quickly as possible to avoid the structures contact with air.

7. Finally, the substrate is placed on cleanroom cloth and dried with an air gun at low pressure. The air gun is held perpendicular and pointing to the middle of the sample.

Gold coating:

1. The fused silica substrate is placed into the sputter deposition chamber by sticking it to a 45°angled SEM sample holder. The sample is rotated after each sputtering cycle, so the position of the edges change. The sputter rate data given for the device used should be utilized to adjust the sputter time according to the desired Au thickness. Plasma current is 20 mA.

Sample holder preparation:

1. The substrate is placed into the main sample holder.

2. The bottom of the silicon edged blocks are covered with double sided tape, and placed on to the substrate. An optical microscope is used for alignment.

3. The silicon edged blocks are secured with clips.

UV-PDMS Preparation:

1. In a UV-light filtered room, a tinted bottle is placed in the scale.

2. The two components of UV-PDMS, the base (A) and the curing agent (B), are dispensed into the tinted bottle with a pipette. Individual pipettes should be used for the solutions.

3. A stirring magnet is placed in the bottle, its cap is placed on the bottle. The bottle is wrapped in aluminum foil and stirred in the magnetic stirrer for 1 hour.

4. The bottle is then placed into the desiccator for 30 minutes. The cap is untightened, just enough to release air, but not taken off before placing it in the desiccator.

5. The UV-PDMS is poured onto the sample holder with the substrate placed into it, then desiccated for a minimum of an hour.

6. After desiccation the sample holder is placed into a UV chamber and cured for 40 minutes.

7. Sample is left in the sample holder for a minimum of 2 hours, then peeled off. A scalpel can be used to cut the uncritical edges of the PDMS to make release easier.

Sylgard PDMS Preparation:

1. The two components of Sylgard PDMS, the base and the curing agent, are combined at a weight ration of 10:1.

2. The mixture is stirred by hand for 5 minutes, or until it is no longer transparent.

3. The mixture is placed into the desiccator for 30 minutes, until no air bubbles are visible.

4. The PDMS mixture is poured onto the sample. If the PDMS is being used for molding, it is placed in the desiccator again for a minimum of 1 hour.

5. The PDMS is cured in the oven for an hour at 40°C.

B.2. Two-photon polymerization - printed pillars

Several nanopillar arrays with varying dimensions were printed over the course of the project. In the images below, SEM measurement are done for prints of 410 nm diameter pillars at 800 nm pitch and 330 nm diameter pillars at 650 nm pitch. The measurements show that varying the laser power by 1% offers good control on the fabricated pillar diameters and thus the r/a ratio that is critical for the bandgap performance of the photonic crystal structures.
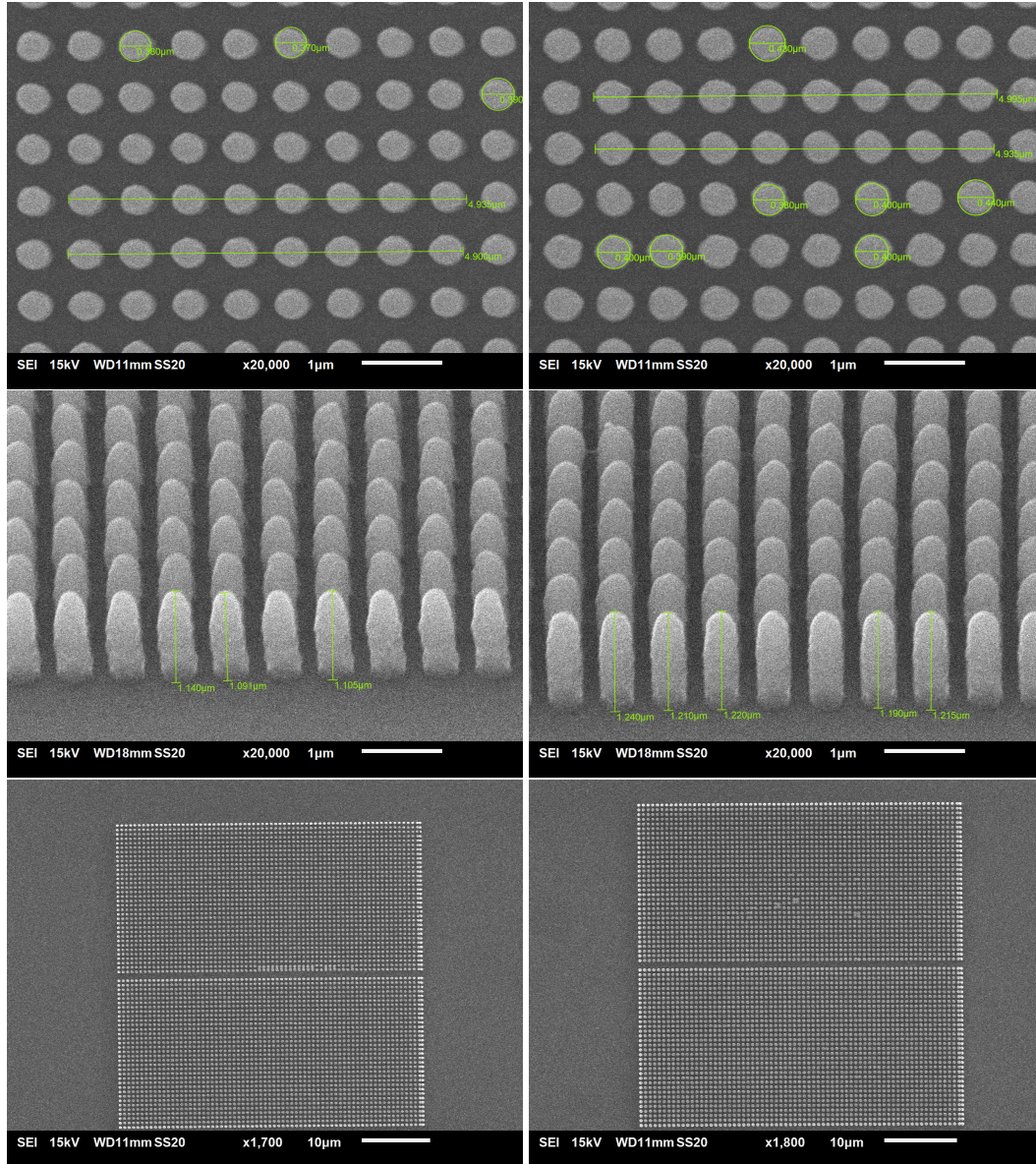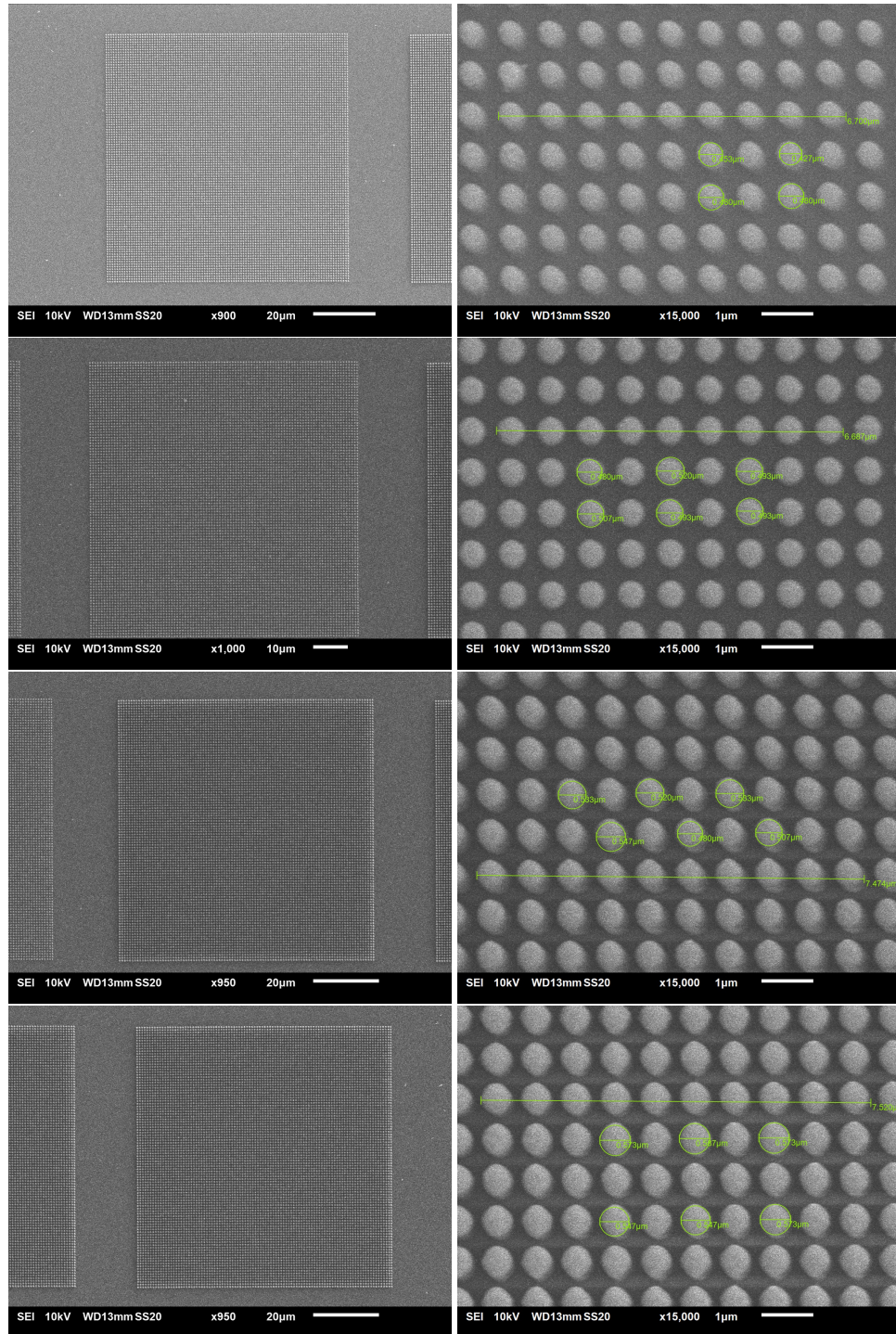

Figure B.2: SEM images showing a nanopillar array of 650 nm pitch, printed with a CAD design of 330 nm diameter pillars with 3.75 aspect ratio. The scanning speed is constant at 1500 μm /sec while the laser power is increased. a) 18% laser power resulting in a pillar diameter of 0.37±0.01 μm. r/a is 0.28. The measured aspect ratio is 3.0. b)19% 0.41±0.02 μm. r/a is 0.32. The measured aspect ratio is 2.96.

Figure B.1: SEM images showing a nanopillar array of 800 nm pitch, printed with a CAD design of 410 nm diameter pillars with 3.75 aspect ratio. The scanning speed is constant at 1500 µm /sec while the laser power is increased. a) 18% laser power resulting in a pillar diameter of 0.46±0.03 µm. r/a is 0.29. b)19% 0.5±0.01 µm. r/a is 0.31. c)20% laser power resulting in 0.52±0.02 diameter. r/a is 0.33. d) 21% laser power resulting in 0.56±0.02 diameter. r/a is 0.35.

B.3. Printing parameters - Dose

Dose testing is a necessity to determine the ideal scan speed and laser power combination for the optimal printing results. Figure B.3 is an example dose test, showing an nanopillar arrays printed with varying dose. The pillar arrays on the left side of the image are not printed, indicating that the dosing was too low to polymerize the photoresist. As the laser power increases towards the right side of the dose test over-polymerization occurs. There exits a diagonal region in the dose test were the pillar arrays exhibit blue color. This is an indication of photonic behavior and thus these are the ideal dose parameters. In the experiments, dosing was seen to be very dependent on the state of the laser which decays over time. It is suggested to first do a larger dose test scanning the laser power and scan speed to determine the parameter range where the printing time is minimized. Counter intuitively, scan speed is not inversely proportional to print time: their relationship is a curve where after a certain threshold, dependent on the print structure, the print time increases with increasing scan speed. After determining this scan speed, fine tuning the pillar size by doing a secondary dose test which scans the laser power in small increment is suggested.
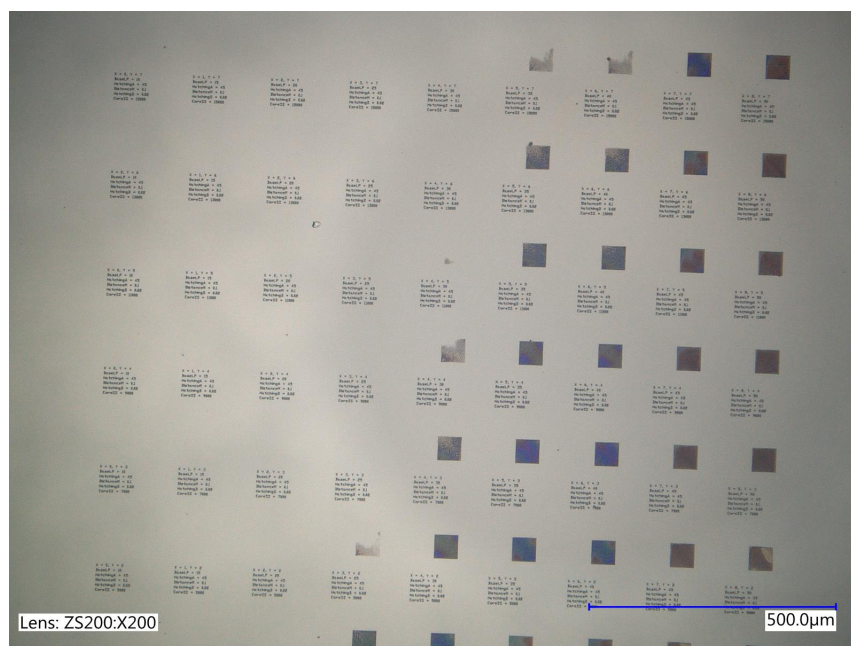

Figure B.3: Example dose testing for nanopillar arrays. x-axis is increasing laser power, y-axis is increasing scan speed.

B.4. Printing parameters - Hatching and Slicing

The dose of the print is dependent on the processing parameters of CAD models. The hatching distance is a parameter for the width of the vertical lines that are used to slice the model. A small hatching distance is expected to increase the resolution with which the print can be done. Figure B.6 shows a dose test with hatching distance and laser power. It can be seen that the dose with which the arrays are polymerized increases as the hatching distance is decreased, even though the laser power and scan speed are kept constant. It can be theorised that the smaller hatch distance means that the structures are sliced into more lines for the laser to sweep and this leads to more exposure. The effect of slicing (the horizontal print lines) follows the same principles and is detailed in Figure B.5
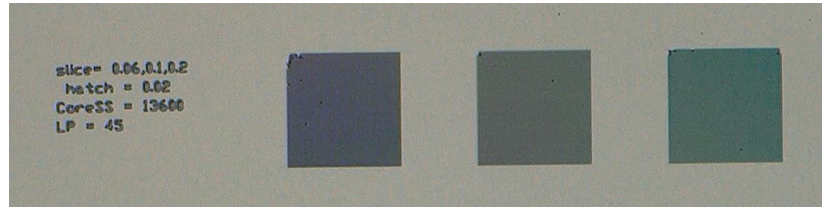

Figure B.4: Optical microscope images showing the effect of increasing slicing (0.06 μm, 0.1 μm and 0.2 μm). The pillar arrays are 420 nm diameter with a 1400 nm pitch. The laser power and scan speed are kept constant for as 45% and 13600 μm/s, respectively.
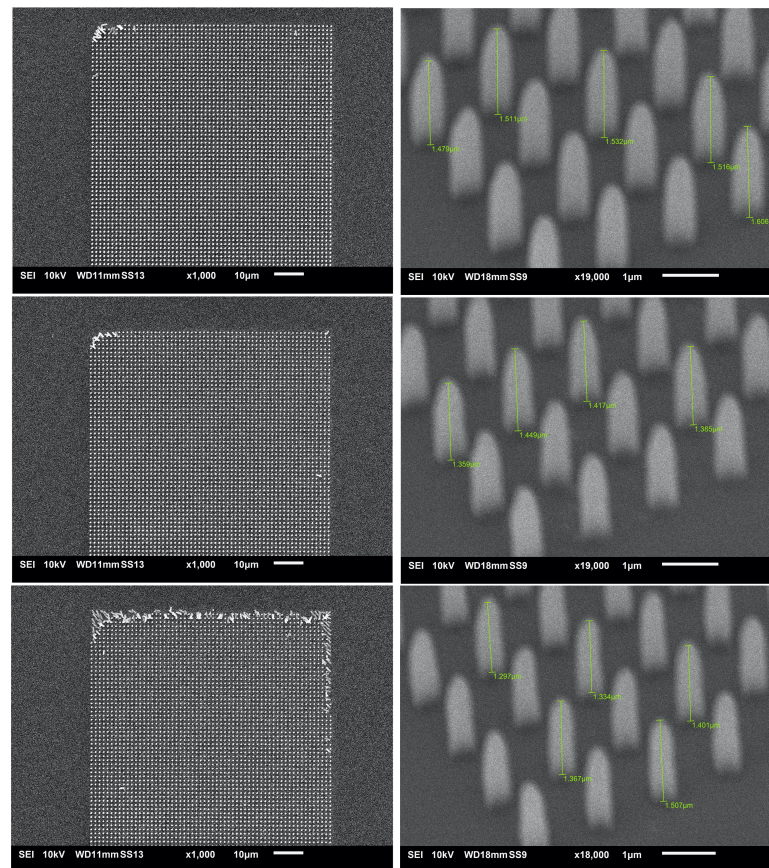

Figure B.5: SEM images showing the effect of increasing slicing (0.06 μm, 0.1 μm and 0.2 μm). The pillar arrays are 420 nm diameter with a 1400 nm pitch. The laser power and scan speed are kept constant for as 45% and 13600 μm/s, respectively.

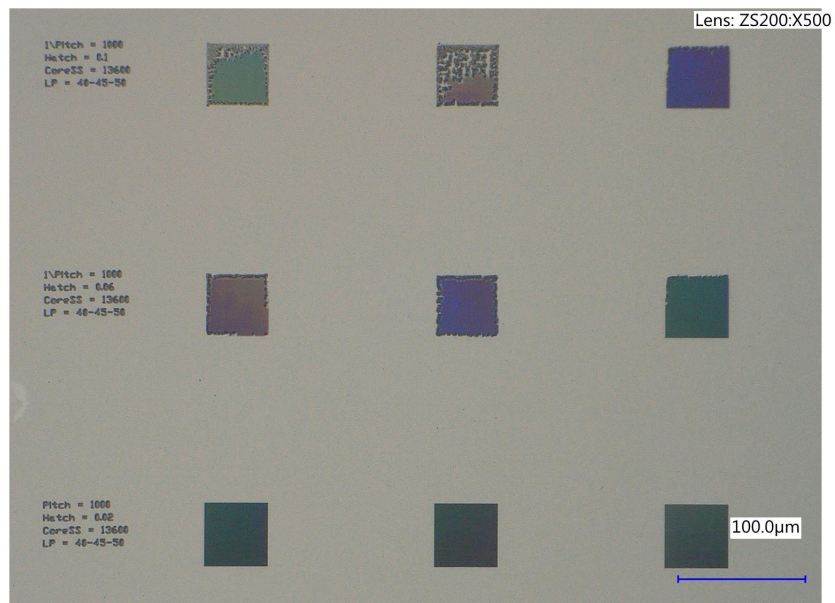Figure B.6: Optical microscope image of dose test scanning +5% laser power increments in the x-axis and +0.04 μm increments in the hatching distance. The scan speed is kept constant at 13600 μm/s. The printed nanopillar models have a lattice constant of 1000 nm and the diameters are 360 nm. The aspect ratio is 3.75.

B.5. Comparison of pillar development methods

Several development procedures were experimented with in order to reach the final development process (section 3.1.1) for the 2PP nanopillars.The advised IP-Dip development method after two-photon polymerization is to immerse the printed substrate in PGMEA for 20 minutes, followed by 5 minutes in IPA [1]. This development method resulted in significantly collapsed pillar arrays. Solutions to the pillar collapse problem were proposed as diluting PGMEA incrementally with IPA and exposing the structures to additional UV treatment while they were immersed in the development liquid [59]. Collapse of the pillars was reduced by using these methods, however the printed arrays were not defect free and collapses occurred at the edges of the prints. Finally, using the solution Novec 7100 Engineered Fluid as the final step added to the conventional development procedure was successful. Figure B.8 is a comparison of printed arrays developed with these methods. Figure B.7 shows the reproducibility of the defectless nanopillar arrays using the chosen development method.
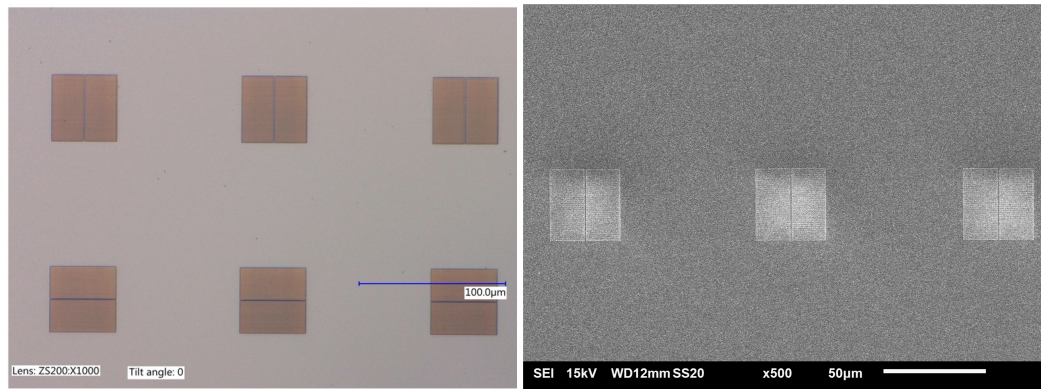

Figure B.7: Optical microscope and SEM images of the nanopillar waveguides developed using Novec 7100. The printed arrays show the same quality and no defects.
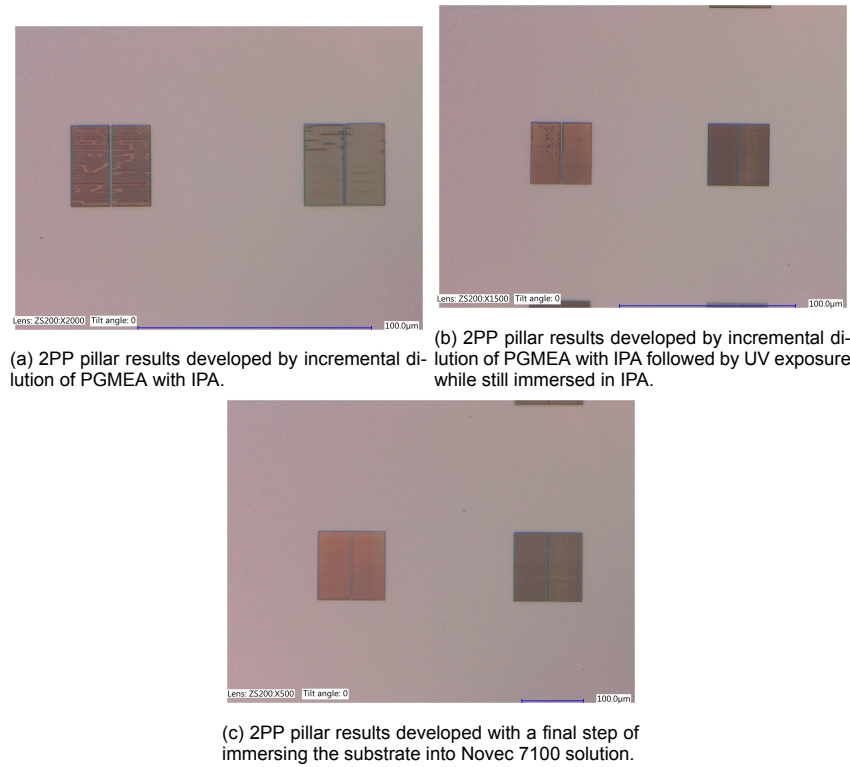

(a) 2PP pillar results developed by incremental dilution of PGMEA with IPA.

(b) 2PP pillar results developed by incremental dilution of PGMEA with IPA followed by UV exposure while still immersed in IPA.

(c) 2PP pillar results developed with a final step of immersing the substrate into Novec 7100 solution.

Figure B.8: 2PP nanopillar arrays developed with different processes.

B.6. Pillar array defects

The printing quality achieved in the Nanoscribe is greatly dependent on the tool condition. During the course of the project, a tilt issue of the tool led to increasingly defective nanopillar arrays to be printed. Figure B.9 shows an example of nanopillars printed 2 months apart, with the condition of the tool declining. Figure B.10 shows the non-uniformity of the prints: it is visible that the tilt issue resulted in the top right corner of the print to be exposed with less dose than that of the bottom of the print. It was observed that the nanopillars, which have a very small feature size, are extremely sensitive to such alignment and dosing issues of the tool. Larger print areas were more effected by the tilt issue. This problem was fixed by maintenance of the tool by the company.
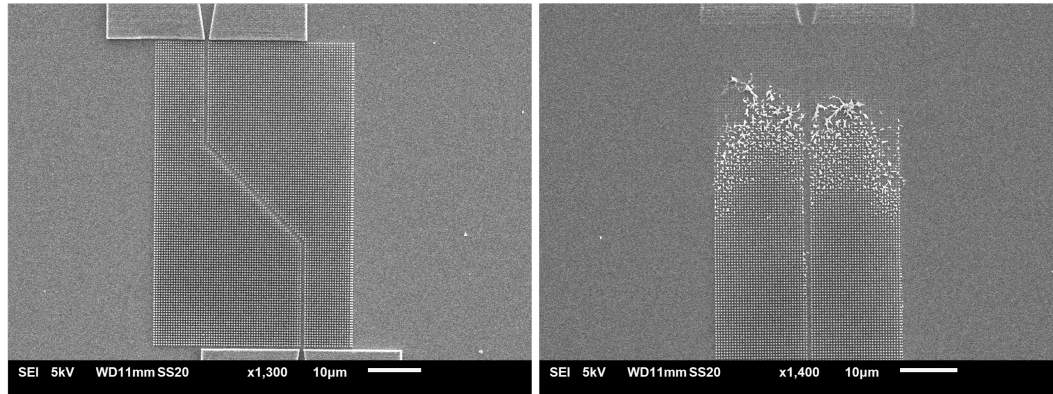

Figure B.9: 40 μm x 60 μm array of 250 nm diameter pillars at 500 nm pitch. The SEM images show prints of the same model as the tilt issue in the printer declined over 2 months. The printing printing parameters were kept unchanged.
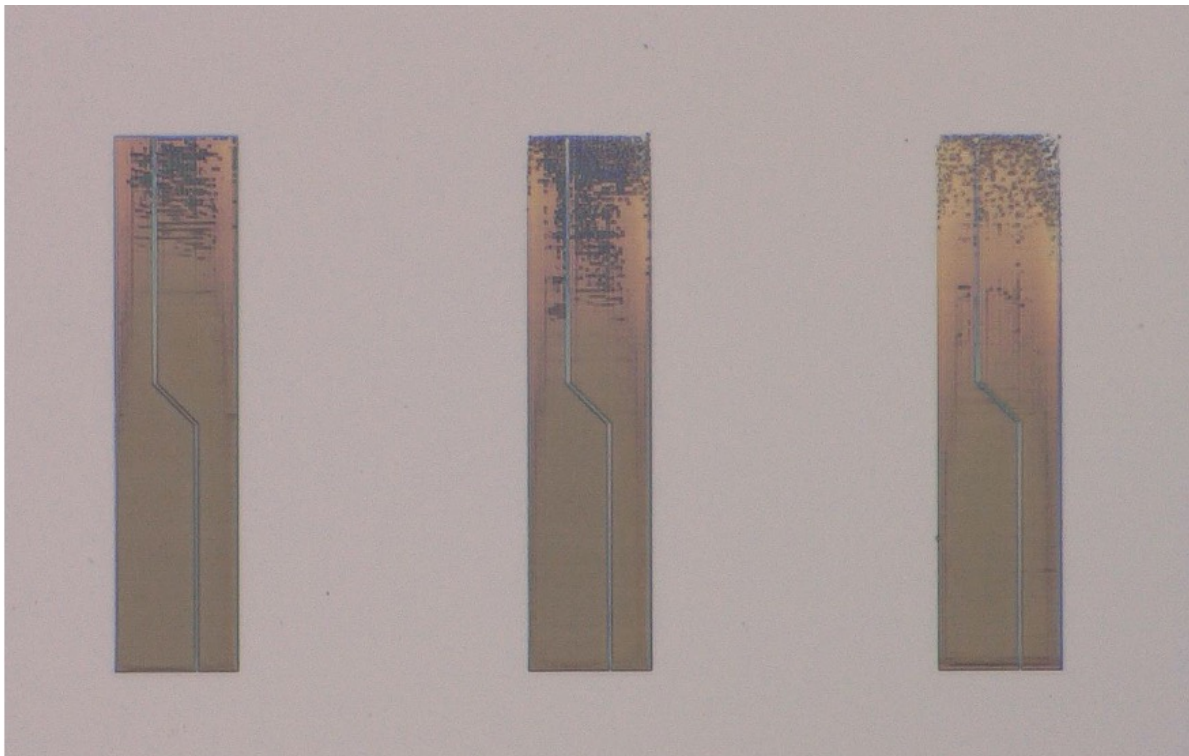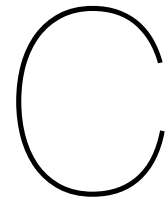

Figure B.10: Optical microscope images of 30 μm x 120 μm nanopillar arrays. The tilt issue is apparent from the change in color of the array from the bottom to the top, indicating nonuniform dosing across the print.

C

Characterization

C.1. Test setup equipment

Previously, the top view of the end-fire test setup was shown in Figure 4.3 and the working principles were explained. The details of the test setup are pictured in the following figures.
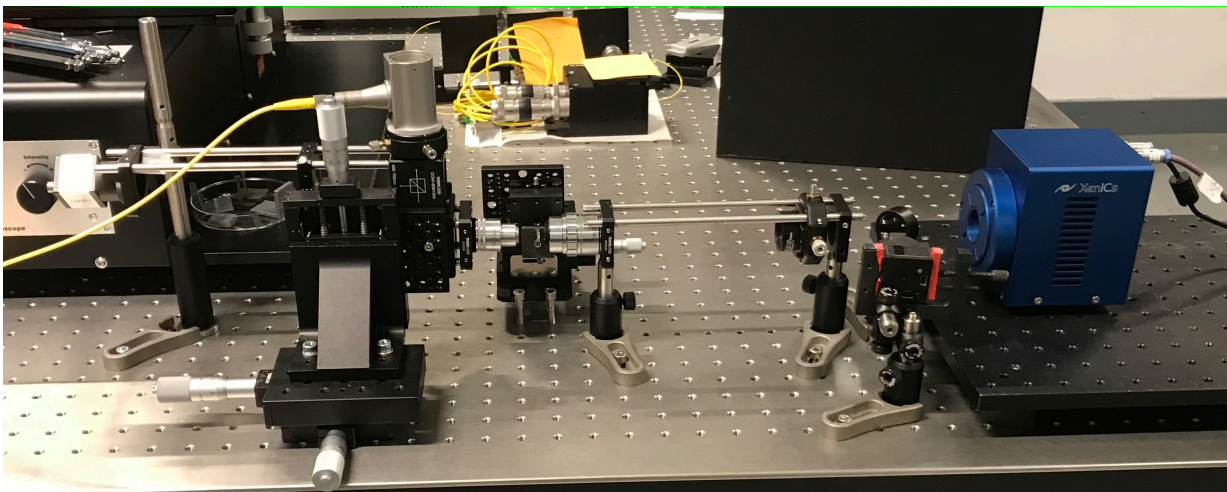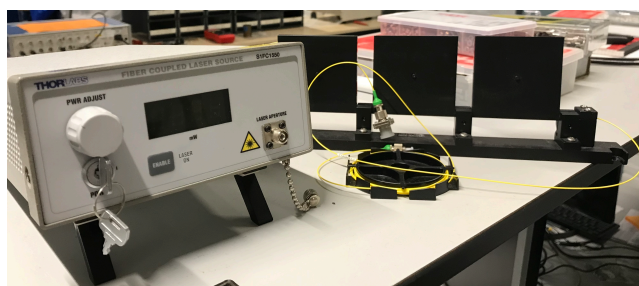

Figure C.1: Side view of the test setup.

Figure C.2: Picture showing the laser source, polarizer and optical fibres that provide light into the set-up.
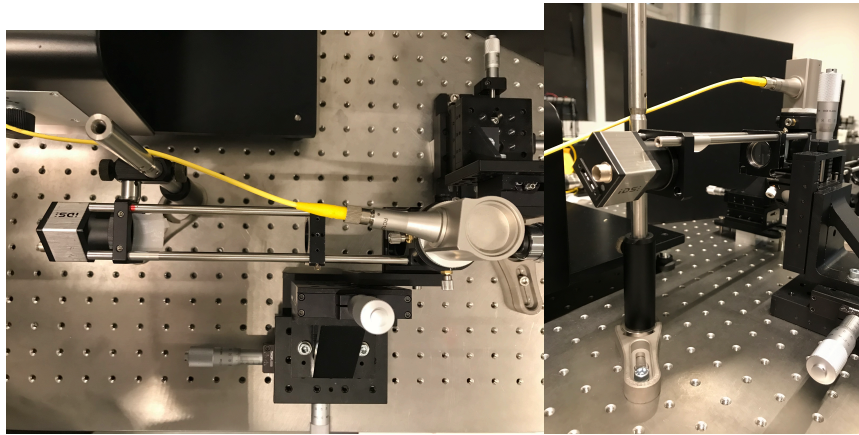
Figure C.3: Details of the light path into the input objective. The camera for visualizing the inlet facet and 150 mm lens focusing light into it is visible. The collimator/beam splitter/mirror system attached to the objective is shown.

Figure C.4: Close up of the sample that is in place in the setup is shown. The objectives are focused on the input and output facets of the sample.

Figure C.5: The path of the light that exits the sample is pictured; showing the focused objective, lens and camera system. The light path is altered using a flip mirror to use the output visible light camera and the infrared camera.

Bibliography

[1] *3D Microfabrication Solution Set Large Features (3D LF)*. URL: `https://support.nanoscribe.com/hc/en-gb/articles/360017312153-3D-Microfabrication-Solution-Set-Large-Features-3D-LF-`.
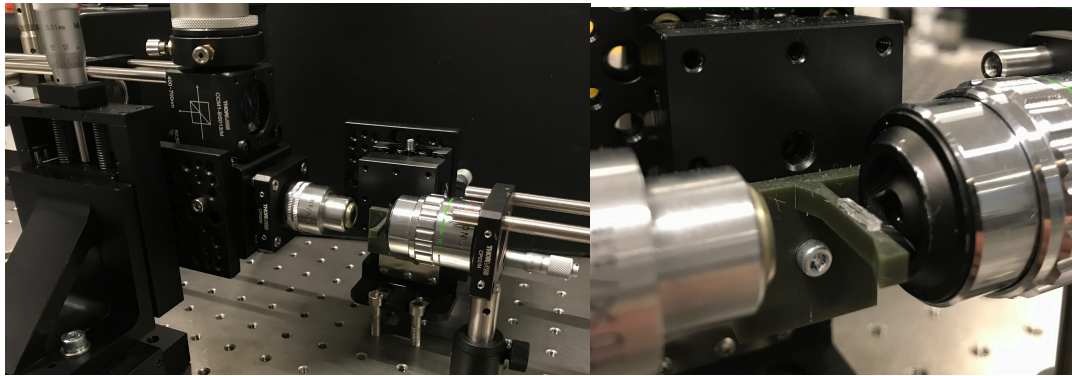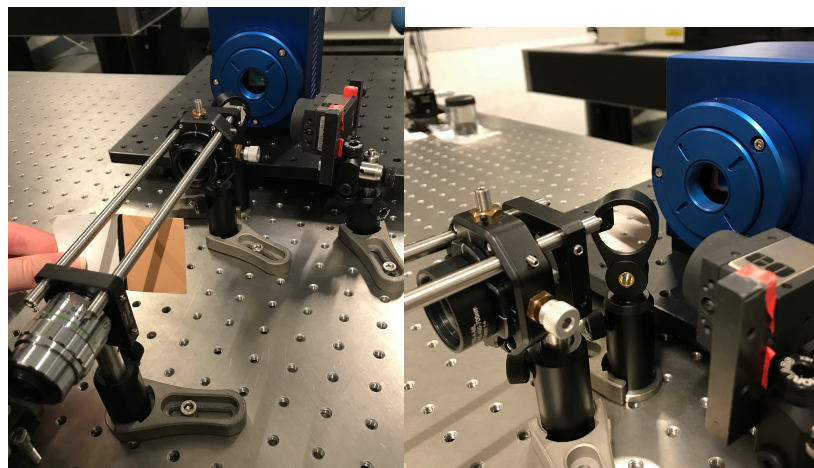
[2] Sadao 1950- Adachi. *Optical constants of crystalline and amorphous semiconductors : numerical data and graphical information LK - https://tudelft.on.worldcat.org/oclc/905482178*. English. Boston ; SE - XX, 714 p. : ill. ; 25 cm: Kluwer Academic Publishers, 1999. ISBN: 0792385675 9780792385677. URL: `http://catdir.loc.gov/catdir/enhancements/fy0821/99023736-d.html%20http://catdir.loc.gov/catdir/enhancements/fy0821/99023736-t.html`.

[3] Ady Arie, Nili Habshoosh, and Alon Bahabad. "Quasi Phase Matching in Two-Dimensional Quadratic Nonlinear Photonic Crystals". In: vol. 39. Jan. 2008, pp. 45–60. DOI: `10.1007/978-88-470-0844-1_4`.

[4] M Assad et al. "Comparative in vitro biocompatibility of nickel-titanium, pure nickel, pure titanium, and stainless steel: genotoxicity and atomic absorption evaluation." In: *Bio-medical materials and engineering* 9 1 (1999), pp. 1–12.

[5] Gabriele Bonaventura et al. "Biocompatibility between Silicon or Silicon Carbide surface and Neural Stem Cells". In: *Scientific Reports* 9.1 (2019), p. 11540. ISSN: 2045-2322. DOI: `10.1038/s41598-019-48041-3`. URL: `https://doi.org/10.1038/s41598-019-48041-3`.

[6] Youngnam Cho and Albena Ivanisevic. "In vitro assessment of the biocompatibility of chemically modified GaAs surfaces". In: *NanoBiotechnology* 2.1 (2006), pp. 51–59. ISSN: 1551-1294. DOI: `10.1007/s12030-006-0007-6`. URL: `https://doi.org/10.1007/s12030-006-0007-6`.

[7] Jeffrey B Chou et al. "Enabling Ideal Selective Solar Absorption with 2D Metallic Dielectric Photonic Crystals". In: *Advanced Materials* 26.47 (2014), pp. 8041–8045. DOI: `https://doi.org/10.1002/adma.201403302`. URL: `https://onlinelibrary.wiley.com/doi/abs/10.1002/adma.201403302`.

[8] Edmond K C Chow et al. "Demonstration of high waveguide bending efficiency (>90%) in a photonic-crystal slab at 1.5-um wavelengths". In: *Physics and Simulation of Optoelectronic Devices IX*. Ed. by Yasuhiko Arakawa, Peter Blood, and Marek Osinski. Vol. 4283. International Society for Optics and Photonics. SPIE, 2001, pp. 453–461. DOI: `10.1117/12.432595`. URL: `https://doi.org/10.1117/12.432595`.

[9] Alison Cowley and Brian Woodward. "A Healthy Future: Platinum in Medical Applications". In: *Platinum Metals Review* 55 (2011), pp. 98–107. DOI: `10.1595/147106711X566816`.

[10] Scott Dhuey et al. "Three-dimensional woodpile photonic crystals for visible light applications". In: *Journal of Physics Communications* 1.1 (Aug. 2017), p. 15004. DOI: `10.1088/2399-6528/aa7ef9`. URL: `https://doi.org/10.1088/2399-6528/aa7ef9`.

[11] Hemant Sankar Dutta et al. "Coupling light in photonic crystal waveguides: A review". In: *Photonics and Nanostructures - Fundamentals and Applications* 20 (2016), pp. 41–58. ISSN: 1569-4410. DOI: `https://doi.org/10.1016/j.photonics.2016.04.001`. URL: `https://www.sciencedirect.com/science/article/pii/S1569441016300116`.

[12] Nagi Elabbasi. *Modeling Phononic Band Gap Materials and Structures*. URL: `https://www.comsol.com/blogs/modeling-phononic-band-gap-materials-and-structures/`.

[13] Neslihan Eti and Hamza Kurt. "Model Analysis of Ridge and Rib Types of Silicon Waveguides With Void Compositions". In: *IEEE Journal of Quantum Electronics* 52.10 (2016), pp. 1–7. DOI: `10.1109/JQE.2016.2598082`.

[14] Joachim Fischer and Martin Wegener. "Three-dimensional optical laser lithography beyond the diffraction limit". In: *Laser & Photonics Reviews* 7.1 (2013), pp. 22–44. DOI: `https://doi.org/10.1002/lpor.201100046`. URL: `https://onlinelibrary.wiley.com/doi/abs/10.1002/lpor.201100046`.

[15] Luís M Fortes, M Clara Gonçalves, and Rui M Almeida. "Flexible photonic crystals for strain sensing". In: *Optical Materials* 33.3 (2011), pp. 408–412. ISSN: 0925-3467. DOI: `https://doi.org/10.1016/j.optmat.2010.09.024`. URL: `http://www.sciencedirect.com/science/article/pii/S0925346710004106`.

[16] Lin Gan and Zhiyuan Li. "Designs and experiments on infrared two-dimensional silicon photonic crystal slab devices". In: *Frontiers of Optoelectronics* 5.1 (2012), pp. 21–40. ISSN: 1674-4594. DOI: `10.1007/s12200-012-0192-y`. URL: `https://doi.org/10.1007/s12200-012-0192-y`.

[17] Lihong Gao, Fabien Lemarchand, and Michel Lequime. "Comparison of different dispersion models for single layer optical thin film index determination". In: *Thin Solid Films* 520.1 (2011), pp. 501–509. ISSN: 0040-6090. DOI: `https://doi.org/10.1016/j.tsf.2011.07.028`. URL: `https://www.sciencedirect.com/science/article/pii/S0040609011014155`.

[18] Vaibhav Gupta et al. "Mechanotunable Surface Lattice Resonances in the Visible Optical Range by Soft Lithography Templates and Directed Self-Assembly". In: *ACS Applied Materials & Interfaces* 11.31 (Aug. 2019), pp. 28189–28196. ISSN: 1944-8244. DOI: `10.1021/acsami.9b08871`. URL: `https://doi.org/10.1021/acsami.9b08871`.

[19] Liam Hanlon et al. "Diamond nanopillar arrays for quantum microscopy of neuronal signals". In: *Neurophotonics* 7.3 (2020), pp. 1–12. DOI: `10.1117/1.NPh.7.3.035002`. URL: `https://doi.org/10.1117/1.NPh.7.3.035002`.

[20] Martin Hetzl et al. "GaN nanowires on diamond". In: *Materials Science in Semiconductor Processing* 48 (2016), pp. 65–78. ISSN: 1369-8001. DOI: `https://doi.org/10.1016/j.mssp.2016.03.013`. URL: `https://www.sciencedirect.com/science/article/pii/S1369800116300580`.

[21] K. Hsu et al. "Wavelength Tuning by Bending a Flexible Photonic Crystal Laser". In: *Journal of Lightwave Technology* 31.12 (June 2013), pp. 1960–1964. ISSN: 1558-2213. DOI: `10.1109/JLT.2013.2262922`.

[22] Maesoon Im et al. "Neural probes integrated with optical mixer/splitter waveguides and multiple stimulation sites". In: *2011 IEEE 24th International Conference on Micro Electro Mechanical Systems*. 2011, pp. 1051–1054. DOI: `10.1109/MEMSYS.2011.5734609`.

[23] Ui-Jin Jeong et al. "A minimally invasive flexible electrode array for simultaneous recording of ECoG signals from multiple brain regions". In: *Lab Chip* 21.12 (2021), pp. 2383–2397. DOI: `10.1039/D1LC00117E`. URL: `http://dx.doi.org/10.1039/D1LC00117E`.

[24] Scott A Jewett et al. "Gallium nitride is biocompatible and non-toxic before and after functionalization with peptides". In: *Acta Biomaterialia* 8.2 (2012), pp. 728–733. ISSN: 1742-7061. DOI: `https://doi.org/10.1016/j.actbio.2011.09.038`. URL: `http://www.sciencedirect.com/science/article/pii/S1742706111004314`.

[25] Hao Jiang et al. "3-D FDTD Analysis of Gold-Nanoparticle-Based Photonic Crystal on Slab Waveguide". In: *Journal of Lightwave Technology* 27.13 (2009), pp. 2264–2270. DOI: `10.1109/JLT.2008.2006577`.

[26] John D. Joannopoulos et al. *Photonic Crystals: Molding the Flow of Light*. 2nd ed. Princeton University Press, 2008. ISBN: 0691124566.

[27] P B Johnson and R W Christy. "Optical Constants of the Noble Metals". In: 6.12 (), pp. 4370–4379. DOI: `10.1103/PhysRevB.6.4370`. URL: `https://link.aps.org/doi/10.1103/PhysRevB.6.4370`.

[28] P. B. Johnson and R. W. Christy. "Optical constants of transition metals: Ti, V, Cr, Mn, Fe, Co, Ni, and Pd". In: *Phys. Rev. B* 9 (12 June 1974), pp. 5056–5070. DOI: `10.1103/PhysRevB.9.5056`. URL: `https://link.aps.org/doi/10.1103/PhysRevB.9.5056`.

[29] Steven Johnson et al. "Linear waveguides in photonic-crystal slabs". In: *Phys. Rev. B* 62 (Sept. 2000). DOI: `10.1103/PhysRevB.62.8212`.

[30] Ihab El-Kady et al. "Metallic photonic crystals at optical wavelength". In: *Phys. Rev. B* 62 (2000). DOI: `10.1103/PhysRevB.62.15299`.

[31] Jack Kee et al. "Design and fabrication of Poly(dimethylsiloxane) single-mode rib waveguide". In: *Optics express* 17 (2009), pp. 11739–11746. DOI: `10.1364/OE.17.011739`.

[32] Sidney F A Kettle and Lars J Norrby. "The Brillouin zone—An interface between spectroscopy and crystallography". In: *Journal of Chemical Education* 67.12 (Dec. 1990), p. 1022. ISSN: 0021-9584. DOI: `10.1021/ed067p1022`. URL: `https://doi.org/10.1021/ed067p1022`.

[33] Low Khee Lam et al. "SURFACE PLASMON EFFECTS AND RESONANCE STATE ON SQUARE LATTICE OF METALLIC PHOTONIC CRYSTALS AND DEFECT MODE IN H POLARIZATION". In: *Progress In Electromagnetics Research C* 83 (2018), pp. 45–56. DOI: `10.2528/PIERC18011601`.

[34] Namil Koo et al. "Improved mold fabrication for the definition of high quality nanopatterns by Soft UV-Nanoimprint lithography using diluted PDMS material". In: *Microelectronic Engineering* 84.5 (2007), pp. 904–908. ISSN: 0167-9317. DOI: `https://doi.org/10.1016/j.mee.2007.01.017`. URL: `http://www.sciencedirect.com/science/article/pii/S0167931707000597`.

[35] A Kromka et al. "9 - Diamond nucleation and seeding techniques for tissue regeneration". In: *Diamond-Based Materials for Biomedical Applications*. Ed. by R Narayan. Woodhead Publishing Series in Biomaterials. Woodhead Publishing, 2013, pp. 206–255. ISBN: 978-0-85709-340-0. DOI: `https://doi.org/10.1533/9780857093516.2.206`. URL: `https://www.sciencedirect.com/science/article/pii/B9780857093400500096`.

[36] Chiung-Wen Kuo et al. "Nanofluidic system for the studies of single DNA molecules". In: *Electrophoresis* 29 (2008), pp. 2931–2938. DOI: `10.1002/elps.200700943`.

[37] Ki yong Kwon and Wen Li. "Integrated multi-LED array with three-dimensional polymer waveguide for optogenetics". In: *Proceedings of the IEEE International Conference on Micro Electro Mechanical Systems (MEMS)* (2013). DOI: `10.1109/MEMSYS.2013.6474421`.

[38] Y Li et al. "UV to NIR optical properties of IP-Dip, IP-L, and IP-S after two-photon polymerization determined by spectroscopic ellipsometry". In: *Opt. Mater. Express* 9.11 (Nov. 2019), pp. 4318–4328. DOI: `10.1364/OME.9.004318`. URL: `http://www.osapublishing.org/ome/abstract.cfm?URI=ome-9-11-4318`.

[39] Caizhi Liao, Alain Wuethrich, and Matt Trau. "A material odyssey for 3D nano/microstructures: two photon polymerization based nanolithography in bioapplications". In: *Applied Materials Today* 19 (2020), p. 100635. ISSN: 2352-9407. DOI: `https://doi.org/10.1016/j.apmt.2020.100635`. URL: `https://www.sciencedirect.com/science/article/pii/S2352940720300834`.

[40] COMSOL Applications Library. *Band-Gap Analysis of a Photonic Crystal*. URL: `https://www.comsol.nl/model/band-gap-analysis-of-a-photonic-crystal-798`.

[41] Jianpeng Liu et al. "Gold nanopillar arrays as biosensors fabricated by electron beam lithography combined with electroplating". In: *Appl. Opt.* 54.9 (Mar. 2015), pp. 2537–2542. DOI: `10.1364/AO.54.002537`. URL: `http://ao.osa.org/abstract.cfm?URI=ao-54-9-2537`.

[42] J.-M. (Jean-Michel) Lourtioz and Dominique. T A - T T - Pagnoux. *Photonic crystals : towards nanoscale photonic devices*. English. Berlin, 2008. DOI: `10.1007/978-3-540-78347-3LK-https://tudelft.on.worldcat.org/oclc/261324944`.

[43] Jie Lu et al. "Light-activated nanoimpeller-controlled drug release in cancer cells". eng. In: *Small (Weinheim an der Bergstrasse, Germany)* 4.4 (Apr. 2008), pp. 421–426. ISSN: 1613-6829. DOI: `10.1002/smll.200700903`. URL: `https://pubmed.ncbi.nlm.nih.gov/18383576%20https://www.ncbi.nlm.nih.gov/pmc/articles/PMC2712492/`.

[44] Lina Maigyte and Kestutis Staliunas. "Spatial filtering with Photonic Crystals". In: *Applied Physics Reviews* 2 (Feb. 2015), p. 011102. DOI: `10.1063/1.4907345`.

[45] Gina Mayonado et al. "Investigation Of The Bragg-Snell Law In Photonic Crystals". In: July 2015. DOI: `10.1119/bfy.2015.pr.015`.

[46] Attila Mekis et al. "High Transmission through Sharp Bends in Photonic Crystal Waveguides". In: *Phys. Rev. Lett.* 77 (18 Oct. 1996), pp. 3787–3790. DOI: `10.1103/PhysRevLett.77.3787`. URL: `https://link.aps.org/doi/10.1103/PhysRevLett.77.3787`.

[47] Nanoscribe Support. *Adjusting the Dose*. URL: `https://support.nanoscribe.com/hc/en-gb/articles/360001159713`.

[48] Nanoscribe Support. *Cad Model Creation*. URL: `https://support.nanoscribe.com/hc/en-gb/articles/360000810253` (visited on).

[49] D Nedeljkovic et al. "Waveguiding at 1550 nm using photonic crystal structures in silicon on insulator wafers". In: *OFC 2001. Optical Fiber Communication Conference and Exhibit. Technical Digest Postconference Edition (IEEE Cat. 01CH37171)*. Vol. 2. 2001, TuC6–TuC6. DOI: `10.1109/OFC.2001.927304`.

[50] A Neumann et al. "Comparative investigation of the biocompatibility of various silicon nitride ceramic qualities in vitro". In: *Journal of Materials Science: Materials in Medicine* 15.10 (2004), pp. 1135–1140. ISSN: 1573-4838. DOI: `10.1023/B:JMSM.0000046396.14073.92`. URL: `https://doi.org/10.1023/B:JMSM.0000046396.14073.92`.

[51] M Nouri-Goushki et al. "3D Printing of Large Areas of Highly Ordered Submicron Patterns for Modulating Cell Behavior". In: *ACS Applied Materials & Interfaces* 12.1 (Jan. 2020), pp. 200–208. ISSN: 1944-8244. DOI: `10.1021/acsami.9b17425`. URL: `https://doi.org/10.1021/acsami.9b17425`.

[52] C K Park et al. "Formation of silicon nitride nanopillars in dual-frequency capacitively coupled plasma and their application to Si nanopillar etching". In: *Journal of Vacuum Science & Technology A* 25.4 (2007), pp. 1073–1077. DOI: `10.1116/1.2713116`. URL: `https://doi.org/10.1116/1.2713116`.

[53] Sang-il Park et al. "Theoretical and Experimental Studies of Bending of Inorganic Electronic Materials on Plastic Substrates". In: *Advanced Functional Materials* 18 (Sept. 2008), pp. 2673–2684. DOI: `10.1002/adfm.200800306`.

[54] Shibnath Pathak. "Chapter 7 - Photonics Integrated Circuits". In: *Nanoelectronics*. Ed. by Brajesh Kumar Kaushik. Advanced Nanomaterials. Elsevier, 2019, pp. 219–270. ISBN: 978-0-12-813353-8. DOI: `https://doi.org/10.1016/B978-0-12-813353-8.00008-7`. URL: `https://www.sciencedirect.com/science/article/pii/B9780128133538000087`.

[55] P Hunter Peckham and D Michael Ackermann. "Chapter 21 - Implantable Neural Stimulators". In: *Neuromodulation (Second Edition)*. Ed. by Elliot S Krames, P Hunter Peckham, and Ali R Rezai. Second Edition. Academic Press, 2018, pp. 275–287. ISBN: 978-0-12-805353-9. DOI: `https://doi.org/10.1016/B978-0-12-805353-9.00021-8`. URL: `https://www.sciencedirect.com/science/article/pii/B9780128053539000218`.

[56] A. K. Piotrowska et al. "Strain-sensitive photonic crystals for sensing applications in structural health monitoring". In: *2015 IEEE Workshop on Environmental, Energy, and Structural Monitoring Systems (EESMS) Proceedings*. July 2015, pp. 102–106. DOI: `10.1109/EESMS.2015.7175860`.

[57] Richard Pleeging. "Polymer nano manufacturing of a biomimicking surface used for kidney stone crystallization studies". PhD thesis. Delft University of Technology, 2019. URL: `https://repository.tudelft.nl/islandora/object/uuid:92ce1f5d-b8cb-4c44-9f63-b59a5f13057e?collection=education`.

[58] Christopher M Proctor et al. "An Electrocorticography Device with an Integrated Microfluidic Ion Pump for Simultaneous Neural Recording and Electrophoretic Drug Delivery In Vivo". In: *Advanced Biosystems* 3.2 (2019), p. 1800270. DOI: `https://doi.org/10.1002/adbi.201800270`. URL: `https://onlinelibrary.wiley.com/doi/abs/10.1002/adbi.201800270`.

[59] Julia Purtov et al. "Improved development procedure to enhance the stability of microstructures created by two-photon polymerization". In: *Microelectronic Engineering* 194 (2018), pp. 45–50. ISSN: 0167-9317. DOI: `https://doi.org/10.1016/j.mee.2018.03.009`. URL: `http://www.sciencedirect.com/science/article/pii/S0167931718301205`.

[60] Lorenzo Rigutti. "Semiconductor Nanowires". In: 2014, pp. 1–33. DOI: `10.1002/047134608X.W8215`.

[61] Gilad Rosenblatt et al. "Nonmodal Plasmonics: Controlling the Forced Optical Response of Nanostructures". In: *Physical Review X* 10 (Mar. 2020). DOI: `10.1103/PhysRevX.10.011071`.

[62] J H Sanders. "Medical instruments identification via a luminescent micro-particle coating as an alternative for existing identification methods". PhD thesis. {TU} Delft.

[63] John P Seymour et al. "State-of-the-art MEMS and microsystem tools for brain research". In: *Microsystems & Nanoengineering* 3.1 (2017), p. 16066. ISSN: 2055-7434. DOI: `10.1038/micronano.2016.66`. URL: `https://doi.org/10.1038/micronano.2016.66`.

[64] Ravi Shukla et al. "Biocompatibility of Gold Nanoparticles and Their Endocytotic Fate Inside the Cellular Compartment: A Microscopic Overview". In: *Langmuir* 21.23 (Nov. 2005), pp. 10644–10654. ISSN: 0743-7463. DOI: `10.1021/la0513712`. URL: `https://doi.org/10.1021/la0513712`.

[65] *Single Mode {FC}/{PC} Fiber Optic Patch Cables*. URL: `https://www.thorlabs.com/newgrouppage9.cfm?objectgroup%7B%5C_%7Did=1362`.

[66] Gyeongho Son et al. "High-efficiency broadband light coupling between optical fibers and photonic integrated circuits". In: *Nanophotonics* 7 (2018). DOI: `10.1515/nanoph-2018-0075`.

[67] Changhoon Sung et al. "Multimaterial and Multifunctional Neural Interfaces: From Surface-type and Implantable Electrodes to Fiber-based Devices". In: *Journal of Materials Chemistry B* 8 (2020). DOI: `10.1039/D0TB00872A`.

[68] *SYLGARDTM 184 Silicone Elastomer Technical Data*. URL: `https://www.dow.com/content/dam/dcc/documents/en-us/productdatasheet/11/11-31/11-3184-sylgard-184-elastomer.pdf?iframe=true`.

[69] Osamu Takayama and Michael Cada. "Two-dimensional metallo-dielectric photonic crystals embedded in anodic porous alumina for optical wavelengths". In: *Applied Physics Letters* 85.8 (2004), pp. 1311–1313. DOI: `10.1063/1.1784047`. URL: `https://doi.org/10.1063/1.1784047`.

[70] Kimberly Tio. "Wettability-controlled permeability of porous PDMS membranes for drug delivery in the brain". PhD thesis. Delft University of Technology, 2018. URL: `http://resolver.tudelft.nl/uuid:d660729a-65d2-471c-ae81-81860acbb11c`.

[71] Roberto Toro et al. "Brain Size and Folding of the Human Cerebral Cortex". In: *Cerebral Cortex* 18.10 (Oct. 2008), pp. 2352–2357. ISSN: 1047-3211. DOI: `10.1093/cercor/bhm261`. URL: `https://doi.org/10.1093/cercor/bhm261`.

[72] *UV-curable liquid silicon rubber / UV-PDMS Data Sheet*. URL: `www.microresist.com`.

[73] P. Viktorovitch. "Physics of Slow Bloch Modes and Their Applications". In: Jan. 2008, pp. 27–42. DOI: `10.1007/978-88-470-0844-1_3`.

[74] Peter Vukusic. "Manipulating the Flow of Light with Photonic Crystals". In: *Physics Today - PHYS TODAY* 59 (Oct. 2006). DOI: `10.1063/1.2387101`.

[75] Zhenlin Wang et al. "Three-dimensional self-assembly of metal nanoparticles: Possible photonic crystal with a complete gap below the plasma frequency". In: *Physical Review B* 64 (2001), p. 113108. DOI: `10.1103/PhysRevB.64.113108`.

[76] Wolfgang S M Werner, Kathrin Glantschnig, and Claudia Ambrosch-Draxl. "Optical Constants and Inelastic Electron-Scattering Data for 17 Elemental Metals". In: *Journal of Physical and Chemical Reference Data* 38.4 (2009), pp. 1013–1092. DOI: `10.1063/1.3243762`. URL: `https://doi.org/10.1063/1.3243762`.

[77] Kejun Xie et al. "Portable wireless electrocorticography system with a flexible microelectrodes array for epilepsy treatment". In: *Scientific Reports* 7.1 (2017), p. 7808. ISSN: 2045-2322. DOI: 10.1038/s41598-017-07823-3. URL: https://doi.org/10.1038/s41598-017-07823-3.

[78] Yu Xin et al. "Single-Mode Tapered Vertical SU-8 Waveguide Fabricated by E-Beam Lithography for Analyte Sensing". In: *Sensors* 19.15 (2019). ISSN: 1424-8220. DOI: 10.3390/s19153383. URL: https://www.mdpi.com/1424-8220/19/15/3383.

[79] Xiaochuan Xu et al. "Flexible Single-Crystal Silicon Nanomembrane Photonic Crystal Cavity". In: *ACS Nano* 8.12 (Dec. 2014), pp. 12265–12271. ISSN: 1936-0851. DOI: 10.1021/nn504393j. URL: https://doi.org/10.1021/nn504393j.

[80] Eli Yablonovitch. "Photonic Crystals: Semiconductors of Light". In: *Scientific American* 285 (Jan. 2002), pp. 47–51, 54. DOI: 10.1038/scientificamerican1201-46.

[81] Dongpeng Yang, Siyun Ye, and Jianping Ge. "From Metastable Colloidal Crystalline Arrays to Fast Responsive Mechanochromic Photonic Gels: An Organic Gel for Deformation-Based Display Panels". In: *Advanced Functional Materials* 24.21 (2014), pp. 3197–3205. DOI: 10.1002/adfm.201303555. URL: https://onlinelibrary.wiley.com/doi/abs/10.1002/adfm.201303555.

[82] Ali K Yetisen et al. "Holographic Sensors: Three-Dimensional Analyte-Sensitive Nanostructures and Their Applications". In: *Chemical Reviews* 114.20 (Oct. 2014), pp. 10654–10696. ISSN: 0009-2665. DOI: 10.1021/cr500116a. URL: https://doi.org/10.1021/cr500116a.

[83] Ping Zhang et al. "A Novel Sandwich Structure For the Flexible Photonic Device to Meet the Biosensing Requirements". In: *Journal of Micromechanics and Microengineering* 28 (May 2018). DOI: 10.1088/1361-6439/aac449.

[84] Xiaoning Zhang et al. "Complex refractive indices measurements of polymers in visible and near-infrared bands". In: *Appl. Opt.* 59.8 (Mar. 2020), pp. 2337–2344. DOI: 10.1364/AO.383831. URL: http://ao.osa.org/abstract.cfm?URI=ao-59-8-2337.

[85] Pengfei Zhao et al. "Stretchable photonic crystals with periodic cylinder shaped air holes for improving mechanochromic performance". In: *Smart Materials and Structures* 28 (2019). DOI: 10.1088/1361-665X/ab1fb8.